THE UNIVERSITY OF CHICAGO

AMYLOID-BETA AGGREGATION INTERMEDIATES

A DISSERTATION SUBMITTED TO
THE FACULTY OF THE DIVISION OF THE BIOLOGICAL SCIENCES
AND THE PRITZKER SCHOOL OF MEDICINE
IN CANDIDACY FOR THE DEGREE OF
DOCTOR OF PHILOSOPHY

GRADUATE PROGRAM IN BIOCHEMISTRY AND MOLECULAR BIOPHYSICS

BY
JAY MAXSON PITTMAN

CHICAGO, ILLINOIS
JUNE 2020

TABLE OF CONTENTS

LIST OF FIGURES

LIST OF TABLES

ACKNOWLEDGMENTS

I am humbly grateful for the help and support that I have received over the years from coworkers, friends, and family. I came to the University of Chicago with a desire to do science and the Meredith Lab provided the ideal environment for me to grow and learn. The University of Chicago BMB program has provided me a warm environment to find the research that engages me and to take part in extensive training alongside wonderful colleagues. I am grateful to the NIH for the support through the Molecular and Cellular Biology Training Grant (T32 GM007183).

The University of Chicago core facilities and collaborators have been crucial in helping me drive my research forward. I would like to thank Yimei Chen for help with electron microscopy and Dr. Elena Solomaha for training me at the BioPhysics core facility. I extend my thanks to Dr. Justin Jureller for training me in Atomic Force Microscopy at MRSEC. A special thanks to Drew Griffin and Tim Walsh for allowing me to do analysis on the VRS-AFM at Asylum Research. I would also like to thank Dr.Joseph Sachleben for the bountiful advice for everything there is to know about NMR and jazz. Thanks to Chris Boughter for showing me how Atomic Force Microscopy can push the boundaries of my analysis.

I would like to thank the members of my committee, Prof. Tobin Sosnick, Prof. Erin Adams, Prof. Gopal Thinakaran, and Dr. Joseph Sachleben, who gave me invaluable advice over the years to help my science reach its potential. Special thanks to my advisor, Dr. Steve Meredith, for constantly being available to teach me and entertain my ideas. I would like to also thank all the members of the Meredith lab who have taught and helped me over the years. Thank you Dr. Atul Srivastava for the myriad of science and life advice.

I am thankful for Andrea for encouraging and supporting me in this journey and more. Lastly, I would like to thank my family. They have done everything they can to support me in my journey and have shown me that I can always count on them.

ABSTRACT

Alzheimer's Disease (AD) is a devastating neurological disorder that impacts millions of people around the world. There is strong evidence that the class of peptides, Amyloid-β, is causative in the neurodegeneration that takes place during AD. Amyloid-β peptides share a common trait, which is the ability to aggregate (or self-associate) to form higher-ordered structures. Of these structures, the mature fibrils act as a final product of this aggregation and are part of the neuritic plaques formed in advanced AD. Much is known about the mature fibrils in terms of their toxicity and molecular structure; however, in the past several decades it has been revealed that aggregate intermediates, such as small oligomers, are just as cytotoxic, if not more, compared to the mature fibril. However, there is very little know about the mechanism of aggregation and structure of these intermediates. In this thesis, I explore the critical role that amphilicity and heterogenous nucleation play in the production and stability of the aggregation intermediates. In **Chapter 2**, we tested the hypothesis that Aβ21-30 is a putative core domain that takes on structure to promote aggregation. However, we found that Aβ21-30 does not have any structure or aggregate. Therefore, we tested a new hypothesis that aggregation is driven by hydrophobic interactions. We appended hydrophobic residues to Aβ21-30 to make Aβ16-34 and found that it forms fibrils through the hydrophobic effect. We then added a cysteine to Aβ16-34 to replicate heterogeneous nucleation and found that the added "focal point" resulted in faster aggregation. In **Chapter 4**, we explored the aggregation of full-length Aβ40 and the role of amphilicity in the formation of oligomers. We found that Aβ40 forms small, stable oligomers via hydrophobic residues in the C-terminal domain. These NanoDroplet Oligomers (NanDOs) are a flickering species that can associate with Zinc ions through the N-terminal domain to produce flocs.

THE LIST OF PUBLICATIONS BASED ON WORK PRESENTED IN THIS THESIS

1. Srivastava AK, **Pittman JM**, Zerweck J, Venkata Somireddy B, Moore PC, Sachleben JR, and Meredith SC. β-amyloid aggregation and heterogeneous nuclation. *Protein Science*, **2019**, *28*, 1567-1581.[Review]

2. Hawk LML*, **Pittman JM***, Moore PC, Srivastava AK, Zerweck J, Williams JTB, Hawk AJ, Sachleben JR, and Meredith SC. β-amyloid model core peptides: Effects of hydrophobes and disulfies. *Protein Science*, **2019**, *29*, 527-541.

3. Zerweck J, Venkata BS, **Pittman JM**, Srivastava AK, Moore PC, Sachleben JR, Thinakaran G and Meredith SC. A versatile method for producing labeled or unlabeled Aβ55,Aβ40, and other β-amyloid family peptides. *Protein Expression and Purification*, **2019**, *162*, 72-82.

4. **Pittman JM***, Srivastava AK*, Boughter CT, Zerweck J, Venkata BS, Moore PC, Smok I, Tonelli M, Sachleben JR, and Meredith SC. The NanoDroplet Oligomers of Aβ40. *In Preparation*.

*. Denotes equal contribution

CHAPTER 1

INTRODUCTION

Alzheimer's Disease (AD) is a neurodegenerative disorder that impacts millions of people around the world. With no known cure for AD, the number of people in America with AD is projected to double in the next 20 years and result in trillions of dollars of care costs. As a result, there is an intense focus on understanding the pathology of AD and developing a compatible therapeutic treatment. However, the complexity of AD remains a challenge to the medical and research community. The disease can take hold up to 10-15 years before the display of any symptoms, such as motor function and memory loss, behavioral changes and insomnia. By the time the symptoms are identified in the patient, much neuronal damage has occurred in parts of the brain, such as the cerebral cortex and hippocampus.[1,2]

In the early 1900s, Alois Alzheimer performed an autopsy on a patient he had been attending for the previous five years, and found that her brain contained what he termed amyloid plaques and neurofibrillary tangles. Since their identification by Alois Alzheimer in the early 1900s, these amyloid plaque deposits are clues that have launched a slew of investigations into the potential mechanism of AD pathogenesis.[3] In 1984, Glenner and Wong chemically dissected the amyloid plaques and determined that they are comprised partly of a protein with "twisted β-pleated sheets" called amyloid-β, a set of short peptides ranging from approximately 38-43 amino acids in length.[4,5]. Over the past century, it has been found that amyloid-beta (Aβ) is a crucial component of neurotoxicity in AD, with its accumulation and lack of clearance being linked to synaptic dysfunction and neuronal death. As a result, a significant goal has been to develop treatments to decrease the production or removal of Aβ from the brain.

1.1 Amyloid-beta and the Pathology of Alzheimer's Disease

The exploration of the role of Aβ in Alzheimer's disease has resulted in the development of the amyloid hypothesis, which describes the relationship among Aβ overproduction, aggregation and neuronal damage.[6] Aβ is produced by the proteolytic processing of amyloid precursor protein (APP), a type I single-pass transmembrane protein that is thought to be critical for intercellular communication, cellular differentiation, adhesion and other factors influencing neuronal growth and function.[7] The differential splicing of the APP gene results in a number of major isoforms, including APP695, APP751 andAPP770. First, β-secretase binds to the extracellular portion of APP and cleaves at position +1 prior to the first N-terminus amino acid of the Aβ sequence. Then, γ-secretase binds to the transmembrane portion of the protein and cleaves again to release Aβ into the luminal (extracellular) space and C-terminal APP Intracellular Domain (AICD) (Figure 1.1).[8] Given the variations in the cleavage of APP by γ-secretase, the two major Aβ alloforms produced by APP processing are Aβ40 and Aβ42, with Aβ40 being more abundant than Aβ42, with a ratio of 9:1[9]. Aβ is cleared in the brain by degradation in neurons, microglia and astrocytes. There is also efflux of Aβ into the blood and other tissues, with clearance being driven by monocytes, lipoproteins, and the liver. The Amyloid Cascade Hypothesis hold that buildup of Aβ into nano- to micro - molar quantities, from either overproduction or lack of clearance, induces sporadic or familial AD. In addition, it is widely believed that Aβ42 is more neurotoxic than Aβ40. Furthermore, the correlation between Aβ concentration and disease progression is complex. For example, Aβ peptide concentration actually falls in the later stages of the disease.[1,10–12]

The connection between Aβ deposition and AD progression has led to exploring multiple mechanisms of Aβ neurotoxicity. In vitro, Aβ was shown to be acutely toxic to neuron cultures, killing the neuronal cells within 24 hours.[13] This toxicity stems from Aβ interacting with cells in a multitude of ways. For example, Aβ oligomers have a surfactant like effect on lipid membranes and Aβ generates reactive oxidative species that lead to cellular ap-

optosis[14–16]. These neurotoxic effects of Aβ lead to a cascade of symptoms including but not limited to neuronal damage, tau aggregation, inflammation and swelling[17–19]. Behind Aβ's toxicity lies a common and critical trait, which is Aβ's ability to aggregate.

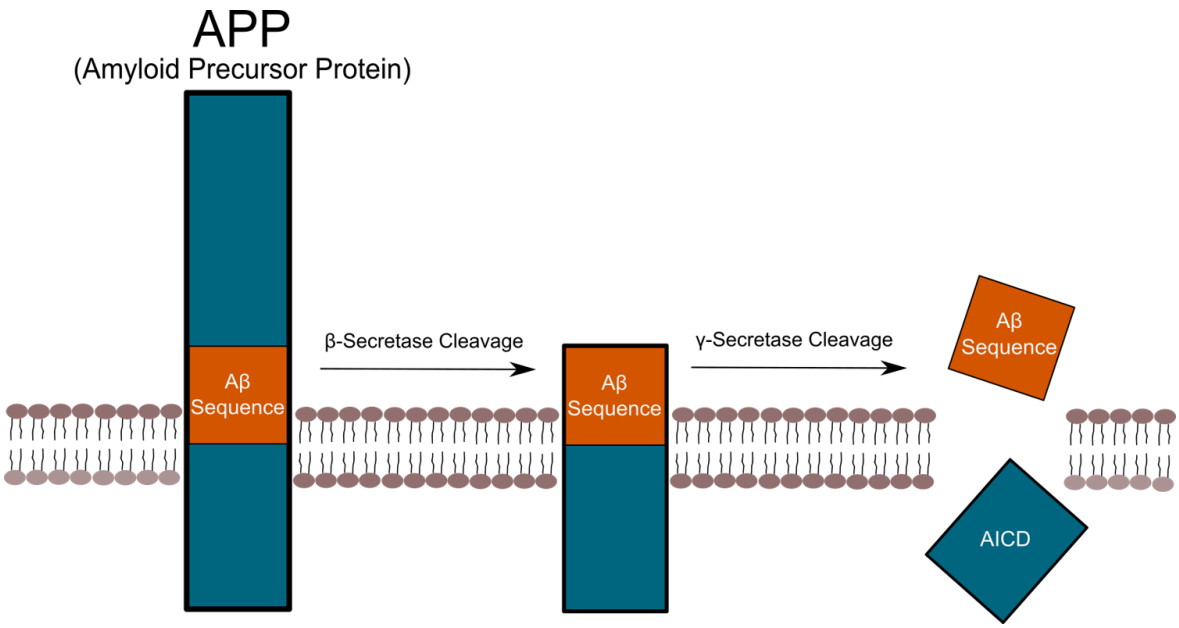

Figure 1.1 The proteolytic processing of APP depicted by initial cleavage by β-secretase and secondary cleavage by γ-secretase. After this, Aβ is release into the extracellular compartment.

1.2 Amyloid-beta Aggregation and Heterogenous Nucleation

Aβ peptides self-associates or aggregates to form a variety of higher-order species, including soluble oligomers and insoluble fibrils. Due to its implications in AD, much has been done to understand the aggregation pathway of Aβ and the morphology of these aggregates (Figure 1.2).

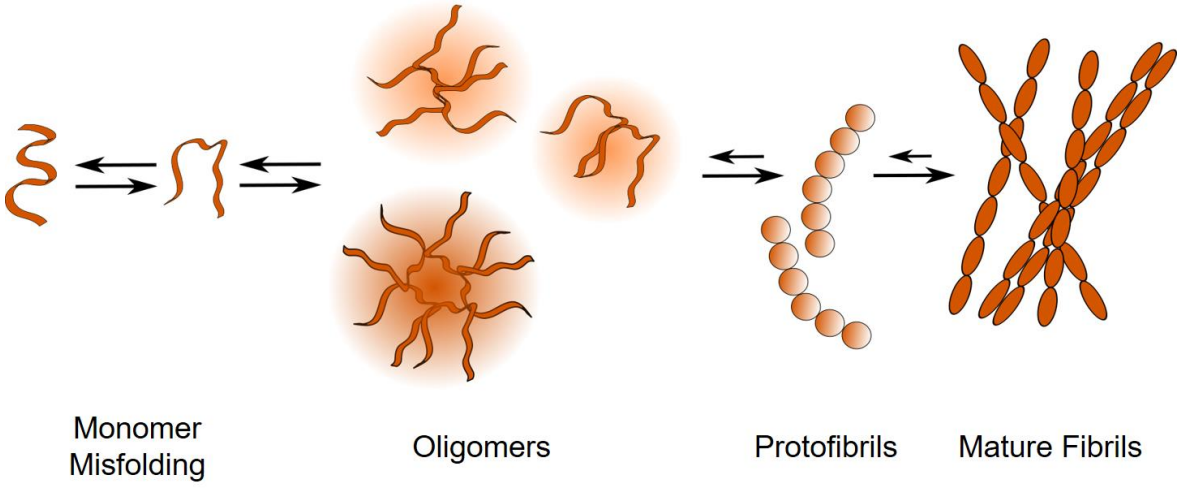

Figure 1.2 A schematic of the aggregation pathway of Aβ.

Most treatments of Aβ aggregation focus on homogeneous nucleation, the mechanism of which has been termed “Nucleation-Polymerization”, i.e. self-association of Aβ monomers to form soluble oligomers. By the reversible addition of single molecules, a series oligomers form until a “critical nucleus” forms, after which the oligomer grows rapidly and falls out as an insoluble fibril.mA critical nucleus can be defined as the smallest aggregate for which it is energetically more favorable to add than to subtract one monomer. Practically, however, the term “oligomer” encompasses a broad class of pre-fibrillar intermediates that range in size and morphology depending on conditions, such as buffer composition, temperature and concentration. Small oligomers ranging from 6 to 40 kDa are secreted and can be identified in cultured cell lines. In addition, some larger oligomers, such as Aβ-derived diffusible ligands (ADDLs) and Aβ*56, have been detected in cell and tissue cultures using immunoblotting. When injected into mice, these induce memory loss in mice[20–24], though these results also have been difficult to reproduce. In any case, soluble oligomers can continue to grow to form soluble “protofibrils” – an inexact term – that resemble “beads on a string”, measuring 5-8nm in width and 150nm in length.[20,25,26] Protofibrils have some β-sheet structure with intraresidue contacts between Glu-22 and

Ile-31 that allow protofibriullar outgrowth, but eventually give way to the formation of the mature, insoluble Aβ fibrils that are richer in β sheet content via the rearrangements in residues 23-26 and Gly33 (Figure 1.3).[27,28]

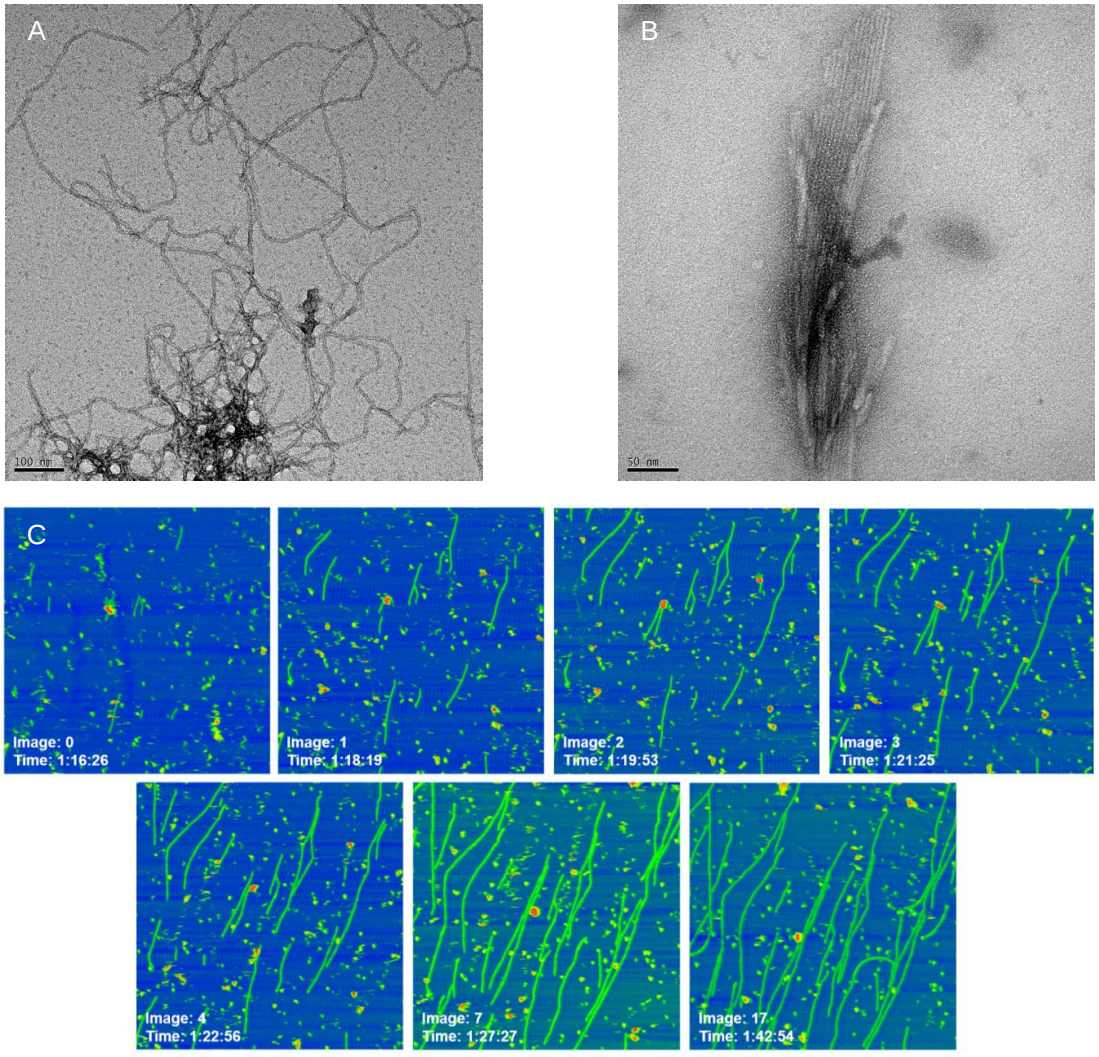

Figure 1.3 (A) TEM of human sequence Aβ fibrils at 49000x and (B) 98000x. Produced in constantly perturbed conditions, the fibrils have a distinct striated appearance. TEM acquired with FEI Tecnai F30 300kv FEG at the UChicago Advanced Electron Microscopy. Facility. (C) AFM of Aβ fibril formation over time. AFM acquired with Cypher Asylum at the UChicago Materials Research and Engineering Center.

The fibrils represent an end-state of Aβ aggregation and are typically found in the core of amyloid plaques formed in AD. Because of their prominence in these plaques, fibril were viewed for a long time as the primary neurotoxic aggregate of Aβ.[23,29] Dendrites that are in proximity to or interacting with Aβ fibril deposits are subject to atrophy, which leads to the breaking of neurites and the disruption of neuronal connections.[30] Different familial mutations in Aβ, such as the ΔE22 Aβ1-39 Japanese mutant and the Iowa mutant, that favor fibril formation are linked with more aggressive forms of AD.[31,32] Thioflavin (ThT) is a dye commonly used to measure the formation of Aβ fibrils by binding along the surface side-chain groves of the β-sheets and shifting from 385 nm to 450 nm in excitation and 445 nm to 482 nm in emission.[33] As examined by ThT fluorescence, the kinetics of Aβ aggregation consist of three phases: lag, growth and plateau. Nucleation is believed to occur during the lag phase. This lag phase can be by-passed by seeding with amyloid-beta fibril fragments or the addition of heterogeneous nucleators, i.e. lipid surfaces and metal-ions (Figure 1.4).

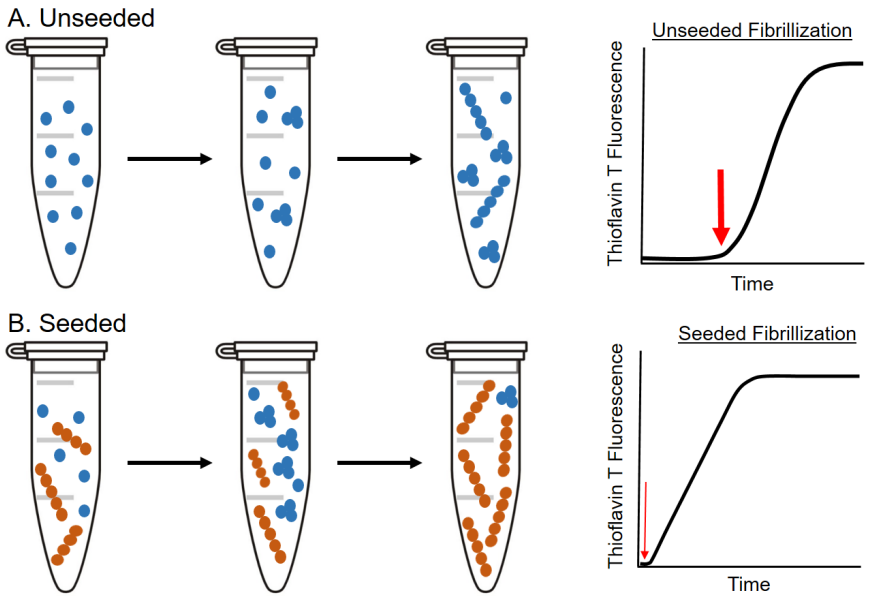

Figure 1.4 Representation of the ThT measurement of unseeded (A) vs seeded (B) Aβ. ”Blue” dots represent non-seed Aβ and the ”orange” fibrils represented added Aβ fibril fragments to initiate catalysis. The addition of these Aβ fibril fragments result in the reduction or elimination the lag phase and transition into the growth phase.

Since the concentration of Aβ in the cerebrospinal fluid is very low, measured at 10ng/mL in some cases (much lower than concentrations typically used for *in-vitro* self-association experiments), heterogeneous nucleation may be the more significant pathway for Aβ aggregation. The Aβ sequence can be divided into two regions: an N-terminal domain consisting mainly of charged residues from amino-acids 1-16 and a C-terminal domain containing two discrete stretches of hydrophobic residues from amino acids 17-21 and 30-40/42 that are typically found to form β sheets in fibril structures (Figure 1.5).[34–36] Reflective of their amphiphilicity, i.e. a molecule that has both hydrophobic and hydrophilic properties, Aβ peptides are capable of forming monolayers[37] in air-water interfaces and micelle-like oligomers.[38,39] This amphiphilic nature of Aβ plays a critical role in this heterogeneous nucleation and production of the amyloid aggregates.

Figure 1.5 Amino acid sequence of Aβ color-coded in respect to different properties. Hydrophobic residues are represented by yellow, while polar residues are red, blue and green. Image from Srivastava et al [34].

In respect to aggregation via the N-terminal domain of Aβ, an important heterogeneous nucleator in AD are metal ions. Neuritic plaques produced in AD were shown to contain mM quantities of metal ions, including Zn^{2+}, Fe^{3+} and Cu^{2+}, and these may be important mediators of heterogeneous nucleation in vivo[40]. The amino acid sequence of amyloid-beta (Figure 1.4) contains three histidine residues (at positions 6, 13 and 14) that are able to bind with divalent and trivalent metals, which are in rapid equilibrium with the metal ions in solution. The addition of metals to Aβ preparations results in increased aggregation, notably fibrillization and precipitation into “amorphous aggregates” through flocculation.[34,41] Addition of Zinc to both Aβ40 and Aβ42 produce “off-pathway” oligomers 12-14nm in size that contain β-sheet structure and are more neurotoxic compared to ADDLs in cell viability and cytotoxicity assays. Here, “off-pathway” oligomer refers to the oligomer

conformationally “trapped” by the metal that is not able to directly elongate into mature fibrils without distinct conformational changes to form a protofibril or a release into monomers that can aggregate (i.e. the addition of EDTA to strip the “off-pathway” oligomers of Zinc or other metals)[42]. The definition of “off-pathway” for amyloids extend to oligomers that have significantly longer half-lives in their transition to the formation of fibrils compared to “on-pathway” oligomers that can incorporate into the fibril structure without dissociation into the monomer form.[43,44]

Lipid surfaces also act as heterogeneous nucleators to catalyze the aggregation of Aβ. Aβ42 forms ion channels, ranging from 1.7 - 2.4nm in diameter, in the lipid membranes of HEK293 immortalized cell lines as measured using patch clamp voltage recording[45]. In other studies, Aβ42 forms pores in DPC micelles and takes on a β-barrel structure detected by CD and NMR.[46] Aβ42 aggregation rate can be significantly enhanced when exposed to lipid vesicle membranes. However, the enchancement is dependent on the characterization of the lipid, where the net negatively charged DOPS lipid vesical membranes shorten the half-time of aggregation by a factor of 4 compared to the zwitterionic DOPC, which only shortens the half-time by 2. Here, fibrils are capable of forming over the surface of the lipid membranes based on the FRET energy transfer from fibril-specific dyes and the probe attached to the lipid head.[47] For Aβ40, the peptide follows a different path, slowing its aggregation when in contact with liposomes made of neutral phophatidycholine and then partially penetrating the membrane[48]. Aβ’s ability to interact with lipid membranes may be the underlying mechanism of toxicity when APP is cleaved and the peptide is released in proximity to the neuronal membrane.[34,49]

1.3 Amyloid-beta and Polymorphism

Polymorphism is a feature present in many amyloidogenic proteins and peptides that has an impact in the interprotein interactions, toxicity and cross-seeding in various neurodegenerative disorders. In Transmissible spongiform encephalopathies (TSEs), the struc-

tural polymorphism of the propagating Prp and the prions fibrils produced may be the underlying explanation of the species barrier for prion transmission.[50,51] For example, Mice that express the Prp found in hamsters are much more susceptible to an injection of hamster PrPsc compared to the wild type mice.[52] α-synuclean, a hallmark amyloid in Parkinson's Disease and dementia that aggregates into Lewy body and Lewy neurites, can form two distinct fibril polymorphs, with the fibril polymorph being more significantly toxic compared to ribbons.[53,54] In yeast, Sup35 is a termination translation protein that aggregates via an NM domain and can produce several amyloid strains with distinct structures. The more structurally rigid the Sup35 amyloid, the less it is able to bind to the Heat Shock Protein (HSP)[55].

Aβ, like other amyloidogenic proteins or peptides mentioned above, can achieve structural polymorphism in fibrils depending on growth conditions[56,57]. Petkova et al. demonstrated that Aβ could achieve structural polymorphism using synthetic Aβ to produce fibrils. To do this, synthetic Aβ40 monomers were placed in two different in-vitro conditions, agitated and quiescent (calm) conditions. Analyzed by TEM and SSNMR, the agitated conditions resulted in the growth of twisted fibrils while the quiescent conditions produced bundled, striated fibrils, with the quiescent fibrils being significantly more toxic to primary embryotic rat hippocampal neurons than the agitated fibrils. Petkova et al. then took the two different fibrils and used them to produce quiescent and agitated "parent" fibril seeds. By seeding Aβ monomers with these fragmented Aβ40 fibril seeds, replicate "daughter" fibrils were generated that have the same molecular structure and morphology as the "parents."[58] Paravastu et al. utilized this seeding method to propagate fibrils in quiescent fibrils and find that the fibrils have a threefold structure, differing from the two fold structure of the agitated fibrils.[59] This work helped to establish a basis for probing the types of Aβ fibrils present in the brains of patients with AD. In work done by Lu et al., Aβ was harvested from the brains of two patients with AD, with Patient 1 having mild cortical atrophy compared to Patient II. The brain-derived Aβ fibrils from each patient were then used to seed synthetic Aβ monomers for replicate fibril growth. This resulted in the

growth of two significantly different fibril structures from Patient I (two fold symmetry) and Patient II (three fold symmetry). There being a predominant type of fibril structure for each patient regardless of the brain region strongly hints that there is a primary nucleation site in the brain that is responsible for the production of single fibril structure.[60] (Figure 1.5) Subsequently, Qiang et al. extracted Aβ from 37 cortical samples of 18 patients with AD. Using brain-seeding methods, patients with rapidly progressive form AD (r-AD) had multiple Aβ40 fibrils with different structures compared to patients with prolonged-duration form AD (t-AD) and posterior cortical atrophy variant AD (PCA-AD).[61]

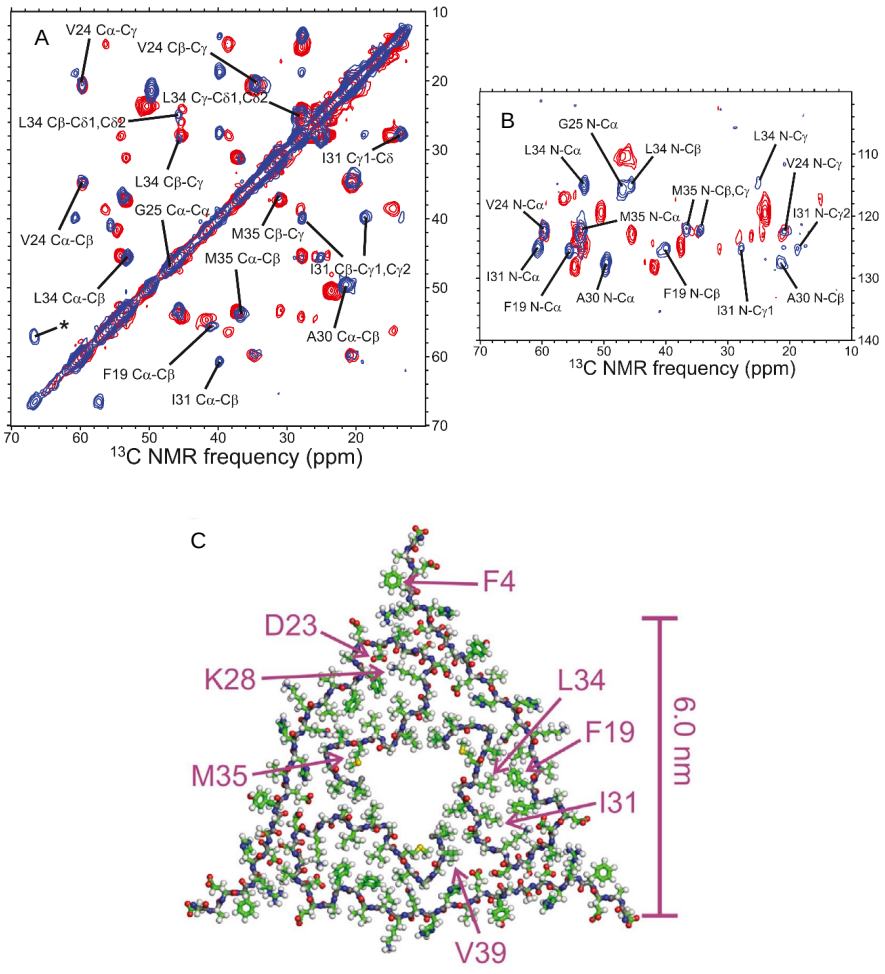

Figure 1.6 (A) Comparison of ssNMR ^{13}C-^{13}C (A) and ^{15}N-^{13}C (B) spectra of Patient I (Red) and Patient II (Blue) brain-seeded Aβ fibrils.(C)3-fold structure of Aβ brain-seeded fibril from Patient I based on Xplor-NIH calculations. Images from Lu et al [60].

1.4 The NMR of Amyloid-beta Intermediates

Research in the past several decades has suggested strongly that soluble oligomers are more neurotoxic than fibrils.[62] In patients, the mass of plaques as measured at autopsy correlates poorly with cognitive dysfunction during life, although both of these are difficult to quantify. In addition, on a “per mass basis” fibrils are less, soluble oligomeric Aβ is more neurotoxic and leads to more neuronal dysfunction and death in vitro during the progression of animal models of AD. For example, soluble Aβ oligomers in humans and mouse models lead to decreased synaptic plasticity and long-term potentiation in neuronal cell cultures.[20,63–66]

In contrast to our growing understanding of fibril structure, however, very little is known about the molecular structure of small Aβ oligomers . The structural analysis of Aβ oligomers is fraught with challenges. Under most conditions in vitro, the Aβ oligomers typically are heterogeneous in size and temporally unstable i.e. they go on to form protofibrils and fibrils. Therefore, there has been a focus on the development of conditions that can favor the stabilization and capture of oligomer species for study. Chimon et al. developed a method to isolate early-state amyloid-beta aggregates under low-salt and low temperature conditions and harvest them using filtration and flash freezing. In this method, Transmission Electron Microscopy (TEM), Atomic Force Microscopy (AFM) and ThT have provided opportunities to track the growth, sizes and morphology of Aβ oligomers. They turned to Solid-state Nuclear Magnetic Resonance Spectroscopy (ssNMRS) to analyze these oligomers. ssNMRS does not have a molecular size limit and can be used to probe the structure of non-crystalline samples; however, it requires isotopic-labeling (usually, ^{1}H, ^{15}N, and/or ^{13}C) in order to make structural determinations. Chimon et al. employed fpRFDR to find that their filtered and trapped Aβ40 oligomers have extensive β-sheet character and therefore, may represent a key kinetic intermediate leading to the formation of protofibrils and fibrils.[67] Following this, low abundance intermediates (7% of the total mass) were produced without purification and freezing and analyzed using ssNMR

1H – 1H dipolar couplings as a spectral filter. These Aβ40 5-15 nm sized oligomers are stable, disordered and have in parallel β-sheet fibrils.[68]

Despite its limitations, which include an upper limit in molecular weight and the need for high peptide concentration, solution NMR remains a powerful tool to understand peptide intra - and intermolecular interactions for proteins. Paramagnetic Relaxation Enhancement (PRE) is a sensitive technique that can be detected up to 34 angstrom (depending on the paramagnetic compound) and can reveal the dynamics of low-population states. Paramagnetic tags have been utilized in determining protein-protein association sites in Calmodulin N- and C-lobes and the sparsely populated interaction states of EDTA-Mn^{2+}tagged HPr and mixed with ^{15}N-labeled EIN.[69–71] Diffusion NMR presents another opportunity to analyze protein oligomerization by utilizing pulse gradients to acquire measurements and calculate diffusion coefficients using the Stejskal-Tanner equation.[72,73] Relaxation (T_1 and T_2) can be measured in samples to shine light on the structural dynamics of proteins and peptides. For example, Fawzi et al. measured R_2 relaxation on Aβ samples in respect to changes in concentration and saw that measured differences in R_2 were due to lifetime broadening effect induced by the incorporation of Aβ monomers into NMR invisible oligomers.[70] These tools are also applicable to the study of, NMR visible oligomers, in addition to the more standard methods of NMR.

1.5 Thesis Topics

In this thesis, we explore the formation of amyloid-beta aggregation intermediates and the manipulation of conditions necessary to control this aggregation. To do this, a variety of techniques were utilized to study the aggregation of Aβ and the Aβ models, including Atomic Force Microscopy and Solution NMR.

In **Chapter 2**, we investigate the aggregation of the congener Aβ peptides to get at the underlying mechanism by which peptides form amyloid fibril. Aβ21-30 has been proposed

to act as a central domain that guides the formation of structure during fibrillization. However, we found that Aβ21-30, cyclo-Aβ21-30 and cys-Aβ21-30 did not aggregate nor have any structure. The key to the formation of fibrils was the addition of hydrophobic residues appended to both the N- and C-terminus of Aβ21-30 (to produce Aβ16-34) in order to favor association via the hydrophobic effect. We then added an N-terminal cysteine residue to Aβ16-34. The addition of cysteine in Cys-Aβ16-34 drastically increased the rate of fibrillization compared to Aβ16-34, suggesting that a heterogeneous nucleator, i.e. metal-ion, could perform a similar role to cysteine by catalyzing and guiding aggregation that results in polymorphic structures found in various subtypes of AD.

In **Chapter 3**, we address the challenges of producing Aβ peptides both Aβ40 and the transmembrane-derived peptide from APP in bacterial systems (Aβ55). Peptide synthesis is by-far the most economical way of obtaining large quantities of unlabeled peptides for studies. However, this method becomes very costly for isotopically labeled peptides in NMR studies. Therefore, bacterial expression systems offer a cheaper way of producing uniformly labeled ^{13}C, ^{15}N or ^{13}C^{15}N peptides. However, Aβ production can be difficult and yields low due to the aggregating nature and limited solubility of the peptides. Here, we present a method of expressing and purifying Aβ using Factor Xa and BNPS-Skatole.

In **Chapter 4**, we stabilize the formation of small oligomers of Aβ40, termed Nanodroplet Oligomers, that have the ability to form instantly and at low Aβ40 concentration. Video-rate Scanning Atomic Force Microscopy (VRS-AFM) show oligomers that are bigger/equal 4nm diameter, a size larger than expected for monomers (1nm), capable of rapidly and spontaneously coalescing and dividing. We use a variety of NMR techniques to explore the formation of the NanDO at the molecular level. ^{13}C-HSQC and HNcoCACB spectra of Aβ40 at a variety of concentrations show chemical shift perturbations (CSPs) in the Cα and Cβ atoms. NMR diffusion studies show a slightly higher diffusion coefficient in lower concentrations than the higher concentration. A MTSL nitroxide labeled was attached to the N-terminal region via Aβ40 Y10C and the C-terminal region via Aβ40

L34C. By measuring peak volumes in ^{15}N-HSQCs, we found that there was a correlation between signal intensity decrease in L34C-MTSL-Aβ40 and amino acid hydrophobicity. This correlation was not seen for Y10C-MTSL-Aβ40. Finally, we explored the role of a heterogeneous nucleator, Zn^{+2}, in the aggregation of the NanDO. Adding Zn^{+2} to the Aβ40 caused the production of larger oligomers via flocculation. HNCO measurements show significant changes in signal in the N-terminal region with the addition of metals. With this, we develop a model showing that NanDOs are in solution and formed through the contacts of hydrophobic residues. When a heterogenous nucleator is added, the N-terminal regions are brought together to form the floc.

CHAPTER 2

BETA-AMYLOID MODEL CORE PEPTIDES: EFFECTS OF HYDROPHOBES AND DISULFIDES

2.1 Introduction

Formation of amyloid fibrils generally includes nucleation, with a transition from largely unstructured monomers to aggregates rich in β-sheets, usually parallel and in-register. In addition, peptides such as Aβ adopt multiple distinct forms or polymorphs, distinguishable by electron microscopy, solid-state NMR, and other techniques.[58,59,74–80] In this article, we compare two hypotheses about how fibrillizing peptides, such as the Aβ peptides, acquire whatever limited structure they possess. According to a first hypothesis, fibrillization begins with a structured core domain that initiates and guides the limited folding. A second hypothesis is that there are few if any specific interactions; rather, Aβ could first become partially aligned through interactions of only modest specificity, for example, by binding a metal ion, or through interactions between hydrophobic side chains in a micelle-like aggregate. According to this second hypothesis, there would be no structured core domain. We compare these hypotheses in the studies reported, below. We report on several model peptides, which are internal fragments of Aβ peptides or variants thereof. Peptides studied include Aβ21–30, Aβ16–34, without or with an N-terminal Cys extension, and a cyclic version of Aβ21–30. Although these internal fragments are not physiological, they allow us to address questions that we would not be able to address with full-length Aβ peptides: in initial studies of Aβ1–40 with a Cys residue appended to the N-terminus, we observed that this peptide formed disulfide bonds very rapidly and was then insoluble even at low peptide concentrations and in fairly harsh solvents(e.g., dimethyl sulfoxide (DMSO)/water/trifluoroacetic acid[TFA] mixtures). This preluded NMR studies. Other investigators had studied Cys-containing Aβ peptides, but these studies also did not include NMR. For example, scanning Cysteine mutagenesis was used to probe solvent accessibility within fibrils[81,82]

and other Cys-containing mutant forms of Aβ[83,84] were developed to examine cytotoxicity or small oligomers. The advantage of using the shorter peptides is that they allowed us to ask three questions: (a) Are short internal fragments, such as Aβ21–30, structured, has been proposed?[85–93] (b) Does the addition of Cys, or cyclization, enhance weak interactions between side chains elsewhere in the peptide, and thereby foster aggregation—that is, by an entropic effect? (c) Does addition of flanking hydrophobic residues convert the internal section of Aβ into an aggregating (fibrillizing) peptide? We will show, below, that Aβ21–30 does not form fibrils, but rather, remain monomeric at all concentrations tested. Attempts to stabilize transient structures through addition of an N-terminal Cys residue (Cys-Aβ21–30) or cyclization (cyclo-Aβ21–30) also led to peptides that always remained unstructured (CD and NMR)and monomeric, and did not form fibrils. On the other hand, extending this domain at both ends to include stretches of hydrophobic amino acids leads to a peptide that aggregates into fibrils. Furthermore, we will also show that addition of the N-terminal Cys to Aβ16–34 enhances the rate of this fibril formation.

2.2 Results

2.2.1 Rationale for the use of model Aβ peptides

We hypothesized that there is no core domain that organizes the limited folding of Aβ into β-sheet-rich amyloid fibrils. To test this hypothesis, we synthesized model peptides to make the following comparisons: 1. We examined peptides from the central region of Aβ peptides, residues 21–30, which has been proposed as an autonomously folding domain.[85–93] In order to stabilize any weak interactions that might exist in this region, we also synthesized a series of peptide variants of Aβ21–30, including Cys-containing and a cyclic peptide, cyclo-Aβ21–30. Cys-Aβ21–30 was monomeric and dimeric only (size exclusion chromatography [SEC], Figure SI 2.8A), soluble, and unstructured by CD spectroscopy and was not further studied. 2. We compared the hydrophilic Aβ21–30 peptide to longer peptides containing this domain, but extending it at each end by adding several

hydrophobic residues, that is, Aβ16–34. We hypothesized that aggregation depends on the presence of multiple weak interactions through the hydrophobic effect; thus, Aβ16–34 would form fibrils while Aβ21–30 would not. 3. We also compared Aβ16–34 with Cys-Aβ16–34, that is, the same peptide as in (2), but containing an additional N-terminal Cys residue. We hypothesized that this Cys residue would act as a "focal point" for interactions between Aβ molecules and would thereby accelerate aggregation by allowing for dimerization, and bypassing a rate-limiting step in aggregation. For (3), we initially synthesized variants of Aβ1–40 and Aβ13–38 containing a single Cys residue appended to the N-terminus. These peptides, however, in contrast to either unmodified Aβ1–40 or Aβ13–38, rapidly formed disulfide bonds and became insoluble in aqueous buffer near neutral pH and even at pH 3 or 10. They were insoluble, furthermore, even in the presence with of organic solvents (e.g., DMSO), denaturants (e.g., urea), or detergents. For this reason, we turned to shorter congeners of Aβ1–40 that maintained the basic domain structure of the full molecule. Aβ16–34 retains the amino acids in the two β-sheets of most Aβ fibrils, and the intervening bend region. Initial experiments (discussed below) showed that this peptide also formed fibrils that exhibit thioflavin T (ThT) fluorescence, and had a fibrillar appearance in transmission electron microscopy (TEM) similar to fibrils formed by Aβ1–40. We also found that appending an N-terminal Cys to Aβ16–34 resulted in a manageable peptide that could be purified, and remained sufficiently soluble in neutral buffers for study by NMR. Figure 2.1 and Table SI 2.1 show the peptides used in these studies.

Figure 2.1 Sequences of Aβ1–40 and internal fragments of Aβ used in these studies. Aβ21–30 and Aβ16–34 were used to make variants with either an N-terminal Cys residue, or cyclized variants.

2.2.2 *Aβ21–30 and variants*

Hypothetically, residues 21–30 of Aβ might form an autonomously folding domain that could guide the acquisition of structure, albeit limited, that accompanies aggregation into fibrils in full-length Aβ peptides, and possibly in the shorter peptides discussed below, such as Aβ16–34. To investigate this possibility, we synthesized Aβ21–30, Cys-Aβ21–30, and cyclo-Aβ21–30. All of these peptides were highly soluble (up to 50 mM), and required no disaggregation procedures, for example, initial dissolution in DMSO, hexafluoroispropanol (HFIP), or 1 mM NaOH. Despite the lack of a disaggregation procedure, Aβ21–30 was monomeric by SEC (Figure SI 2.8a) and sedimentation equilibrium analytical ultracentrifugation (MW = 963, calculated molecular weight = 947.0 g mol^{-1}, Figure SI 2.8b); SEC of Cys-Aβ21–30 showed monomer and dimer only. CD spectroscopy of this peptide up to 500 μM indicated no structure (Figure 2.2a), and the mean residue ellipticity did not change at the concentrations tested, which also indicates the absence of aggregation. CD spectra of cyclo-Aβ21–30 up to 500 μM were essentially identical and indicated no structure(Figure 2.2b). Aβ21–30, Cys-Aβ21–30, and cyclo-Aβ21–30 did not form fibrils. Analysis of $^{1}H,^{1}H$-total correlational spectroscopy (TOCSY), -rotating-frame overhauser effect spectroscopy (ROESY), and-nuclear overhauser effect spectroscopy (NOESY) (Figure 2.2c,d) $^{1}H,^{15}N$ heteronuclear single quantum coherence spectroscopy (HSQC) and $^{1}H,^{13}C$-HSQC for Aβ21–30 (Figure SI 2.9, Table SI 2.6,2.7), Cys-Aβ21–30 (not shown), and cyclo-Aβ21–30 (Figure SI 2.10, Table SI 2.8,2.9) indicated no long range connectivities (for some small peptides and other molecules, NOESY signal can approach zero or become negative. Thus, it was possible that this peptide would have little or no NOESY signal, but this clearly is not the case). The chemical shifts obtained from these spectra were analyzed by TALOS+ as described in Section 2.4.11. In all cases, no secondary (or higher order) structure was detected; rather, all peptides were predicted to be coils, by both sequence and NMR chemical shift data. These experiments did not include a disaggregation procedure; hence, while trace amounts of organic solvent (DMSO or HFIP) might, in theory, abrogate or eliminate weak structures under other circumstances, this clearly

was not the case under our conditions. The NMR finding around which the proposal of a folded structure for this region rested was a connectivity in the 1H,1H-ROESY spectrum of Glu22 Hα to Ala30 HN.[85] A subsequent paper by the same group assigned the peak to two overlapping peaks, Glu22 Hα to Ala30 HN and Lys28 Hα to Ala30 HN.[86] Using a higher field instrument (900 rather than 500 MHz), however, another group showed that there were no long range rotating frame overhauser effect (ROEs), and only weak medium range ROEs; furthermore, the peak in question was an i,I + 2 contact between Lys28 HR and Ala30 HN. Like the latter group, we also observed no long range ROEs or NOEs, albeit under somewhat different solvent conditions. Nevertheless, under our solvent conditions, we conclude that these peptides are monomeric and unstructured.

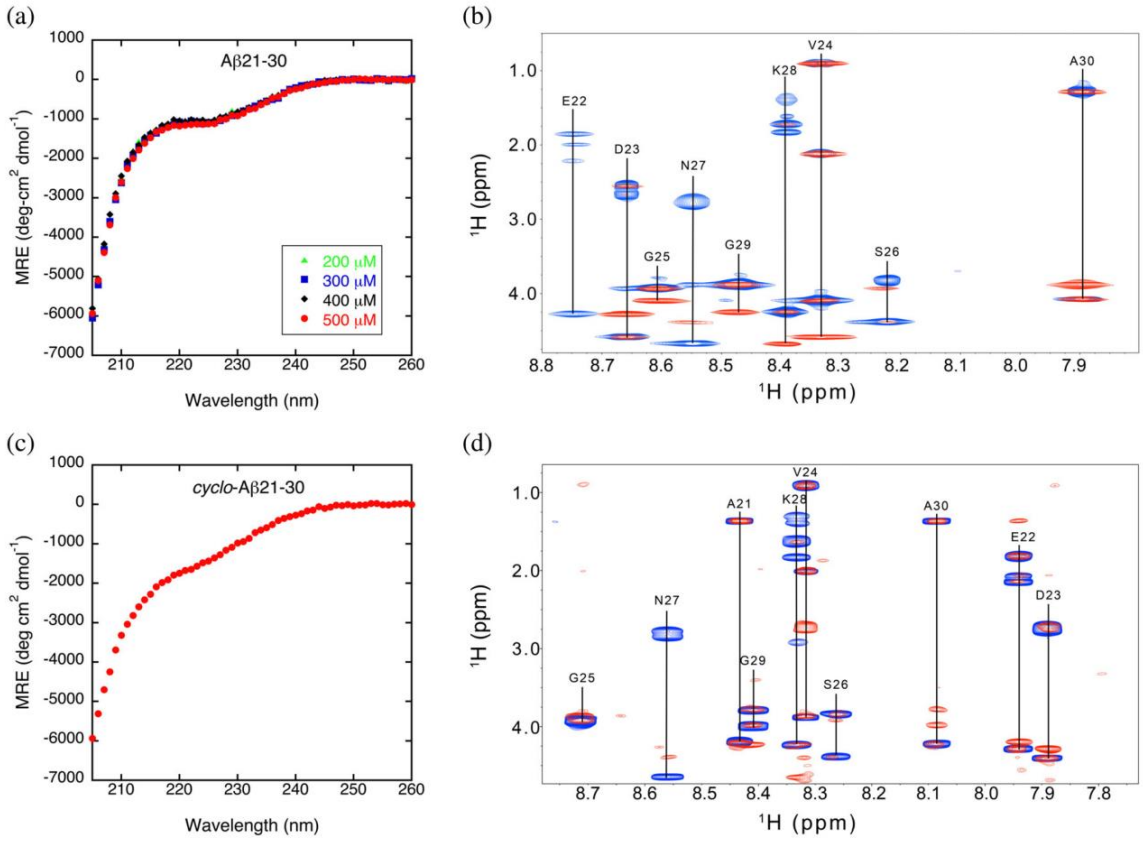

Figure 2.2 Circular dichroic and NMR spectroscopy of Aβ21–30 and cyclo-Aβ21–30. (a) Circular dichroic spectra of Aβ21–30 at concentrations of 200–500 μM, as indicated in the legend. (b) Circular dichroic spectrum of cyclo-Aβ21–30 at 500 μM. In (a) and (b), the spectra are plotted as Mean Residue Ellipticities, which do not vary with peptide concentration, consistent with monomeric status.(c) Superimposed 1H,1H-TOCSY (blue) and ^{1}H,^{1}H-ROESY (red) spectra of Aβ21–30. We also acquired ^{1}H,^{1}H-NOESY spectra (not shown), which were essentially the same as the ^{1}H,^{1}H-ROESY spectra. (d) Superimposed ^{1}H,^{1}H-TOCSY (blue) and ^{1}H,^{1}H-NOESY (red) spectra of cyclo-Aβ21–30. NOESY, nuclear overhauser effect spectroscopy; ROESY, rotating-frame overhauser effect spectroscopy; TOCSY, total correlational spectroscopy

2.2.3 Initial characterization of Aβ16–34 and Cys-Aβ16–34

Initial characterization of these peptides included ThT fluorescence as a marker of fibril formation, electron microscopy of fibrils, SEC, and sedimentation equilibrium analytical ultracentrifugation. As expected for fibril-forming peptides, both Aβ16–34 and Cys-Aβ16–34 displayed typical ThT fluorescence after 1–3 days (Figure 2.3a). Fluorescence was greater for Cys-Aβ16–34 than for Aβ16–34 under the same fibrillization conditions. Adding 0.1 % (vol:vol) β-mercaptoethanol (β-ME) at the start of the fibrillization reaction greatly diminished ThT fluorescence of Cys-Aβ16–34. Transmission electron microscopy of both peptides indicated the presence of typical amyloid fibrils (Figure 2.3b,c). Both peptides were mainly or entirely monomeric when first dissolved. This was shown by SEC (Figure 2.3d,e) and analytical ultracentrifugation (sedimentation equilibrium, Figure 2.3f,g). In the case of Aβ16–34, the size of the monomer peak gradually diminished over 3 days. No oligomer peak was observed in SEC. Analytical sedimentation equilibrium ultracentrifugation confirmed the predominance of monomers: MW = 2,584, calculated molecular weight = 1,978.3 g mol^{-1}. In SEC of Cys-Aβ16–34, there was a more rapid decline in the monomer peak than for Aβ16–34. In addition, peaks with elution positions of dimers and oligomers were observed.

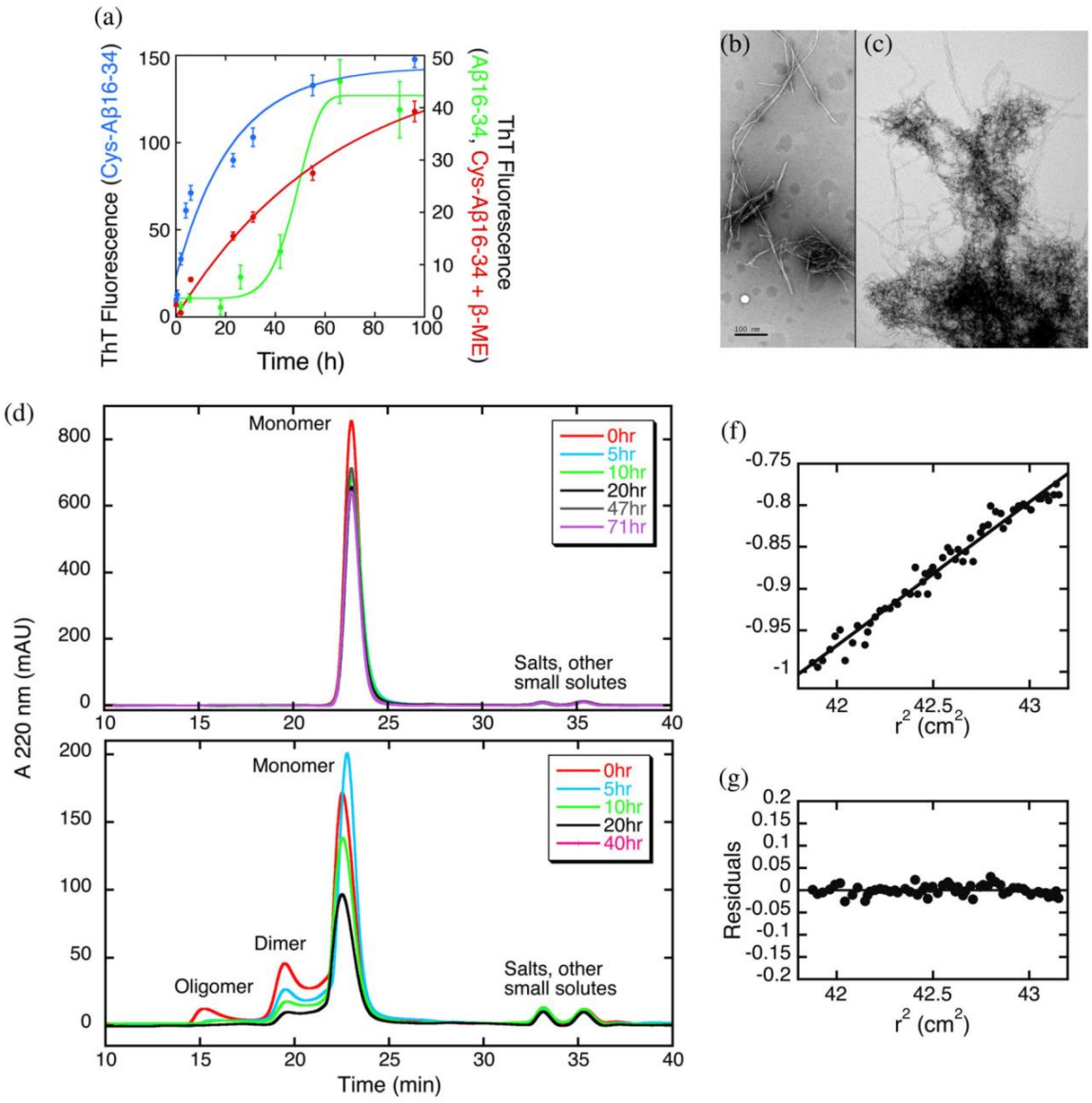

Figure 2.3 Initial characterization of Aβ16–34 and Cys-Aβ16–34. (a) Thioflavin T fluorescence of Aβ16–34 (green), Cys-Aβ16–34 (blue), Cys-Aβ16–34 in the presence of β-ME (red). Points represent mean ± SE for three replicate samples. Note that the two y-axes have different scales. (b, c) Transmission electron micrographs of fibrils of (b) Aβ16–34 and (c) Cys-Aβ16–34. Peptides were disaggregated as described in Methods and allowed to fibrillize at 37C under quiescent conditions. Magnification is ×15,000. (d, e) Size exclusion chromatography of Aβ16–34 and Cys-Aβ16–34, respectively, at various times, as indicated in figure. (f) Analytical ultracentrifugation (sedimentation equilibrium) of Aβ16–34. (g) Residuals for the fit of data shown in panel (f). β-ME, β-mercaptoethanol

2.2.4 Formation of disulfide bonds by Cys-Aβ16–34

Initial observations from SEC and ThT fluorescence indicated that Cys-Aβ16–34 formed fibrils more rapidly than Aβ16–34. Furthermore, these experiments also indicated that the final solubility of Aβ16–34 was greater than that of Cys-Aβ16–34. As a preliminary to NMR experiments discussed below, we measured the rate of disulfide bond formation as a function of temperature. The rate of disulfide bond formation (measured using the Ellman reagent) increased with temperature (Figure 2.4), as expected. Kinetics were analyzed as a second-order reaction, that is,

$$A = \frac{(A_0 - A_{eq})}{(1 + kA_0 t)} + A_{eq} \quad (1)$$

A = absorbance at 412 nm (from Ellman reagent), $A_0 = A_{412nm}$ at t = 0, $V_{eq} = A_{412nm}$ extrapolated to infinite time, t = time, and k = rate constant. The rate constants fit the Arrhenius equation (Figure 2.4, inset). As discussed below, the second-order rate equation is an approximation, albeit a fairly accurate one, for the kinetics scheme used below in our analysis of NMR data.

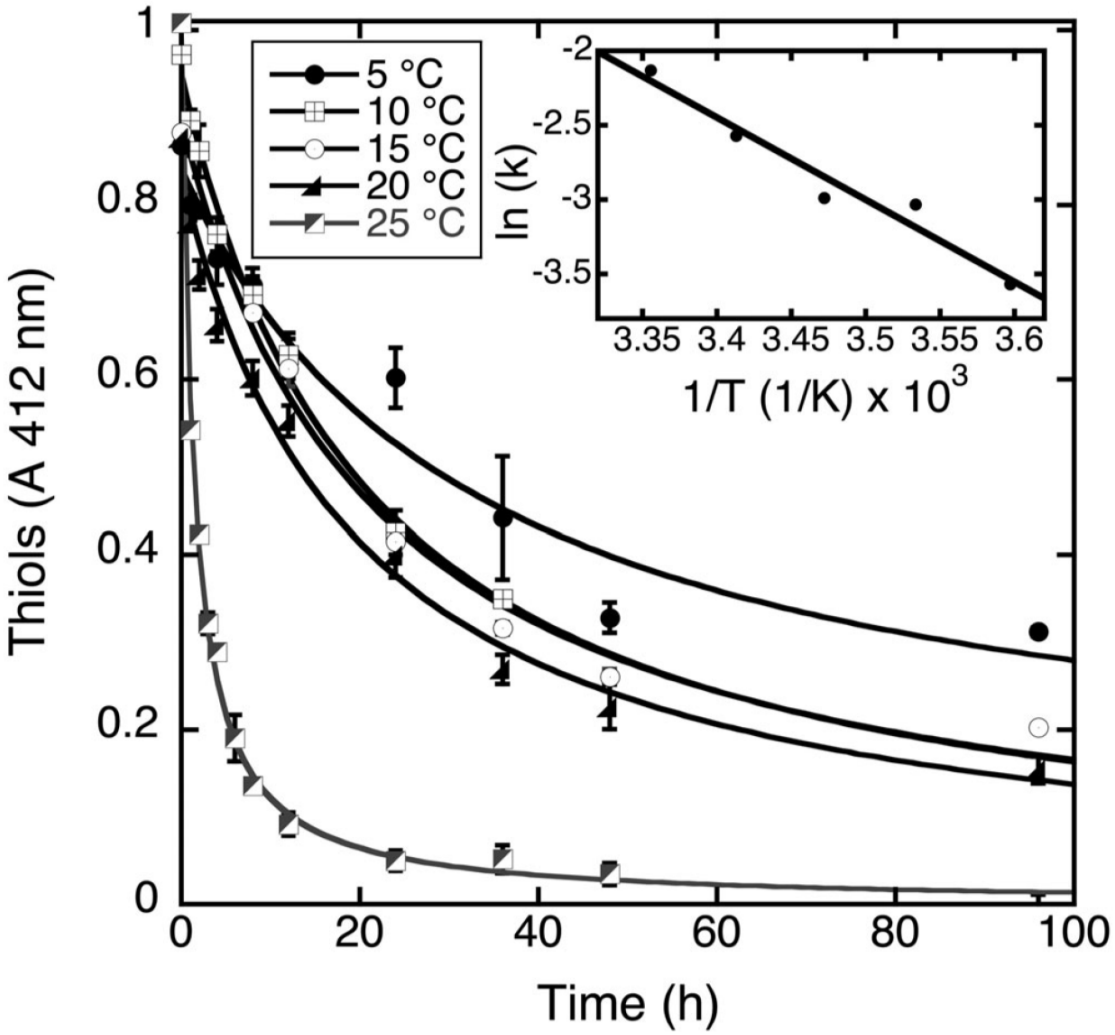

Figure 2.4 Concentration of thiols, assayed using the Ellman reagent, of Cys-Aβ16–34, treated as in serial TOCSY experiments, at various temperatures (from 5°C to 25°C). Initial values are normalized to unity. Lines are nonlinear least squares fit to second-order reaction equation.Inset shows an Arrhenius plot of the second-order rate constants; least square fit yielded $ln(k) = ln(A) - \frac{E_a}{R}(\frac{1}{T}) = 16.33 - 5.5E03(\frac{1}{T})$ where k = rate constant, A = pre-exponential factor, E_a=activation energy, T = absolute temperature, and R = 8.314X10^{-3}kJ mol^{-1} K^{-1}; fit of straight line, r =0.98. TOCSY, total correlation spectroscopy

2.2.5 NMR spectroscopy of Aβ16–34 and Cys-Aβ16–34

Assignments of peaks were made by standard methods; peak heights and volumes were measured using NMRView software. In addition to $^{1}H,^{1}H$-TOCSY and -NOESY spectra, spectra acquired included ^{13}C- and ^{15}N-HSQC of Aβ16–34 and Cys-Aβ16–34 (Figures SI 2.11-2.14). Chemical shifts are listed in Tables SI 2.2,2.3 and 2.4,2.5 for Aβ16–34 and Cys-Aβ16–34, respectively. No long-range nOes were observed for Aβ16–34 and Cys-Aβ16–34, consistent with CD spectra showing no stable secondary structure (not shown). No peak broadening accompanied loss of peak volume and height in any of the time courses, that is, the volume/height ratio showed no change over time. Although soluble oligomeric intermediates are observed for most or all fibril-forming peptides, and indeed were observed by other methods in the case of Cys-Aβ16–34 (Figure 2.3e; see also Figure SI 2.17, discussed below), no new NMR peaks were observed over the course of these experiments. The lack of such peaks could be due to low concentrations of oligomeric species, and/or peak broadening for larger oligomers, and/or similarity in chemical shifts between monomers and dimers or oligomers. In order to compare the fibrillization of Aβ16–34 and Cys-Aβ16–34 at a site-specific as well as a global level, we acquired serial $^{1}H,^{1}H$-TOCSY spectra, and in some cases, 1H-NOESY spectra for these peptides. As indicated above (SEC, ThT fluorescence kinetics), Cys-Aβ16–34 appeared to form fibrils more rapidly than Aβ16–34. This was confirmed in the experiments to be described below. We determined conditions that would allow a direct comparison of Aβ16–34 and Cys-Aβ16–34. Initial experiments showed that at appropriate peptide concentrations for observing both fibrillization and NMR spectra (≥100 μM), the optimal temperature for following serial (time-dependent) TOCSY spectra was 15°C. The read-out of serial TOCSY experiments was decay of peak intensities (volumes and heights) as the fibrillization reaction proceeded. These initial experiments showed that at 5°C CysAβ16–34 precipitated within 3 days, but the spectra of Aβ16–34 barely changed at all even over longer time periods, indicating that fibril formation either did not occur or was extremely slow. On the other end of the spectrum, at temperatures ≥20°C, both peptides fibrillized, but many of

the peaks could no longer be observed. An additional experimental limitation at 25°C was that Cys-Aβ16–34 precipitated within 12 hr, limiting the number of time points and thus the accuracy of the kinetics parameters that could be obtained (TOCSY experiments took 45–90 min, depending on conditions). Therefore, we settled on 15°C as a temperature at which both peptides could be compared. Time courses were obtained for three separate samples of each peptide. Because Cys-Aβ16–34 forms disulfide bonds while Aβ16–34 cannot, different schemes were used to analyze the kinetics of peak decay for these two peptides, as discussed in the next sections.

2.2.6 Kinetics of peak decay for Aβ16–34

For Aβ16–34, ^{1}H,^{1}H-TOCSY peak volumes (and heights) decayed over the course of 2–3 days, and this decay was analyzed as a pseudo-first-order approach to equilibrium, that is

$$V = (V_0 - V_{eq})e^{-kt} + V_{eq} \quad (2)$$

where V = peak volume, V_0 = peak volume at t = 0, V_{eq} = peak volume extrapolated to infinite time, t = time, and k = rate constant. That Aβ peptide fibrillization approached an equilibrium was in agreement with many previous studies, especially by those of Wetzel and associates.[94,95] The average rate for sites within Aβ16–34 (Figures 2.5 and Figure SI 2.15) was 0.016 ± 0.004 hr^{-1} (mean ± SD). 1H spectra also were acquired after each of the serial TOCSY experiments, and the peaks in the amide region (7.0–9.0 ppm) were integrated to obtain area under the peaks. These values similarly decayed over the time course of the experiment (Figure SI 2.16). Analyzed using the same equation, the pseudo-first-order rate constant was 0.026 ± 0.0006 hr−1 (mean ± SD), in reasonable agreement with the mean of rate constants obtained from the serial TOCSY spectra. The mean value for Veq (Equation 2) was 0.810 ± 0.0510. For all peaks volumes, Veq was higher for Aβ16–34 than for Cys-Aβ16–34 (kinetics analyzed below).

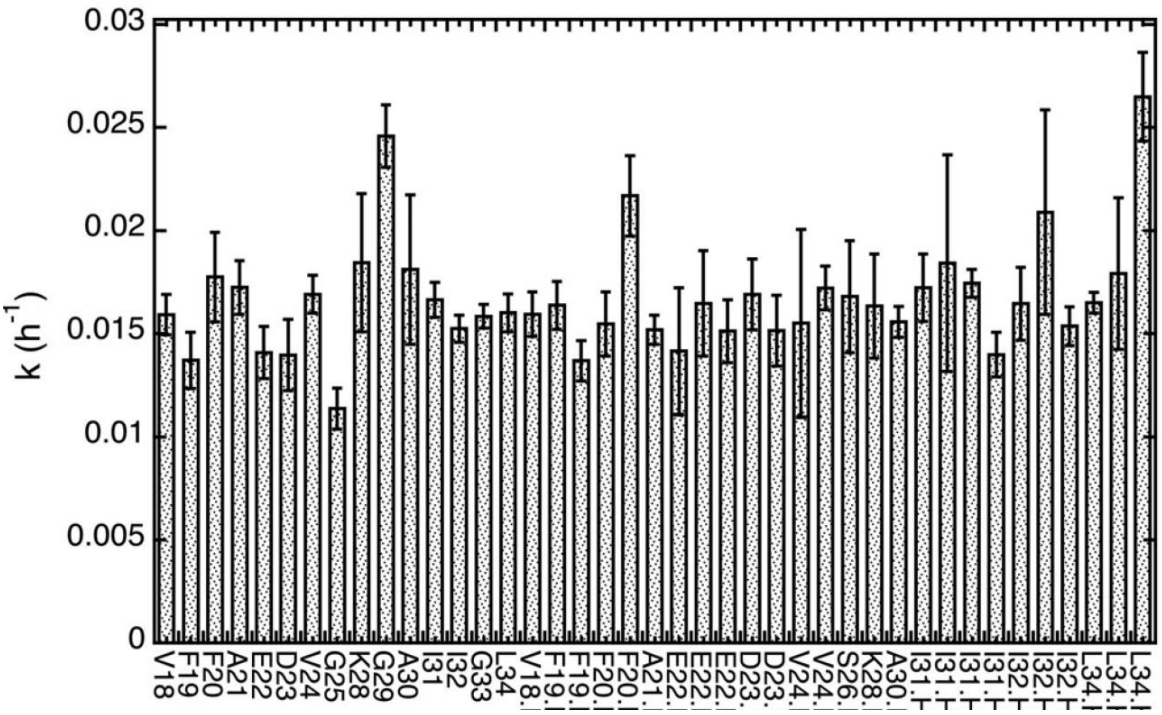

Figure 2.5 Rate constants obtained from analysis of serial TOCSY spectra of Aβ16–34. Data were analyzed as a pseudo-firstorder approach to equilibrium, as described in text. Data represent means from three experiments on replicate samples; error bars are SDs for the rate constant parameter. TOCSY, total correlational spectroscopy.

2.2.7 Kinetics of peak decay for Cys-Aβ16–34

In contrast to Aβ16–34, attempting to fit data on Cys-Aβ16–34 showed clear disagreement with the pseudofirst-order kinetic scheme. We hypothesized the following kinetic scheme:

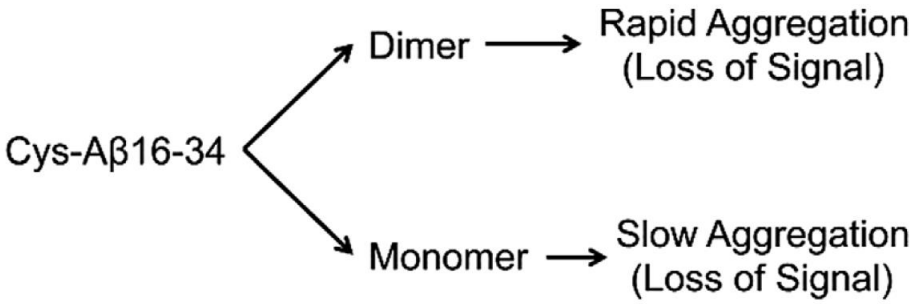

Whereas reactions of both Aβ16–34 and Cys-Aβ16–34 represented an approach to equilibrium, dimerization of Cys-Aβ16–34 is followed by very rapid precipitation of the peptide, with little dimer remaining in solution, while monomer precipitates at a rate similar to that of Aβ16–34. This is borne out by sodium dodecyl sulfate polyacrylamide gel electrophoresis (SDS-PAGE) of peptide remaining in solution at the end of the kinetics experiment (Figure SI 2.17), which shows a higher proportion of monomeric peptide remaining in solution than in the pellet, which was mostly dimeric. Thus,

$$2A \xrightarrow{k_2} A_2 \tag{3a}$$

$$A + A_n \xrightarrow{k_1} A_{n+1} \tag{3b}$$

where A and A2 are monomeric and dimeric peptide, An and An+1 fibrils or large oligomers not observable in TOCSY experiments, and k1 and k2 are rate constants. Thus, the rate equation is given by:

$$\frac{dA}{dt} = -k_1[A_n][A] - k_2[A]^2 \tag{4}$$

that is, parallel pseudo-first- and second-order reactions. Since the concentrations of oligomers and fibrils are low compared with monomer and do not undergo large changes with time, the first term on the right side of the above equation can be written as a pseudo-first-order reaction, that is,

$$\frac{dA}{dt} = -k'[A] - k_2[A]^2 \tag{5}$$

where k' is the pseudo-first-order rate constant. Integrating this differential equation yields:

$$A = \frac{(A_0 - A_{eq}k')}{((A_0 - A_{eq})k_2 + k')e^{k't} - (A_0 - A_{eq}k_2)} + A_{eq} \quad (6)$$

Or, put into terms of peak volumes:

$$V = \frac{(V_0 - V_{eq}k')}{((V_0 - V_{eq})k_2 + k')e^{k't} - (V_0 - V_{eq}k_2)} + V_{eq} \quad (6)$$

The solution of this differential equation is given in Supporting Information. From this analysis (Figures 2.6a,b and SI 2.18), the pseudo-first- and second-order rate constants averaged over all the analyzed TOCSY cross peaks were 0.0022 ± 0.0064hr $^{-1}$ and 0.10 ± 0.01 volume units (VU)$^{-1}$ hr^{-1}, respectively (mean ± SD). Additional statistical analyses of these fits include calculation of the Akaike information coefficient.[96–98] (see Supporting Information) and likelihood functions.[99–101] (Figure SI 2.19). Although the units of these second-order rate constants cannot be compared directly to those obtained from disulfide bond formation (Figure 2.4), the first half-lives were quite similar: 10 hr at 15°C in both cases. An additional point is that the range of second-order rate constants was fairly narrow, from 0.08 to 0.13 VU^{-1} hr^{-1}. This point is also reflected in the fact that the SD for the rate constants was 10% of the mean value, that is, 0.10 ± 0.01 VU^{-1} h^{-1}. Thus, in addition to accelerating the fibrillization of Cys-Aβ16–34 compared with Aβ16–34, the addition of the Cys residue has an ordering effect on aggregation. The mean value for Veq for Cys-Aβ16–34 was 0.24 ± 0.049 (mean ± SD), compared with 0.81 ± 0.051 for Aβ16–34, confirming that Cys-Aβ16–34 was less soluble than Aβ16–34. Finally, the above serial TOCSY experiment was repeated in the presence of 100 mM tris(2-carboxyethyl) phosphine (TCEP). This concentration of TCEP retards but does not eliminate disulfide bond formation. In general, the second-order rate constants were 72% those observed in the absence of TCEP (Figure SI 2.20).

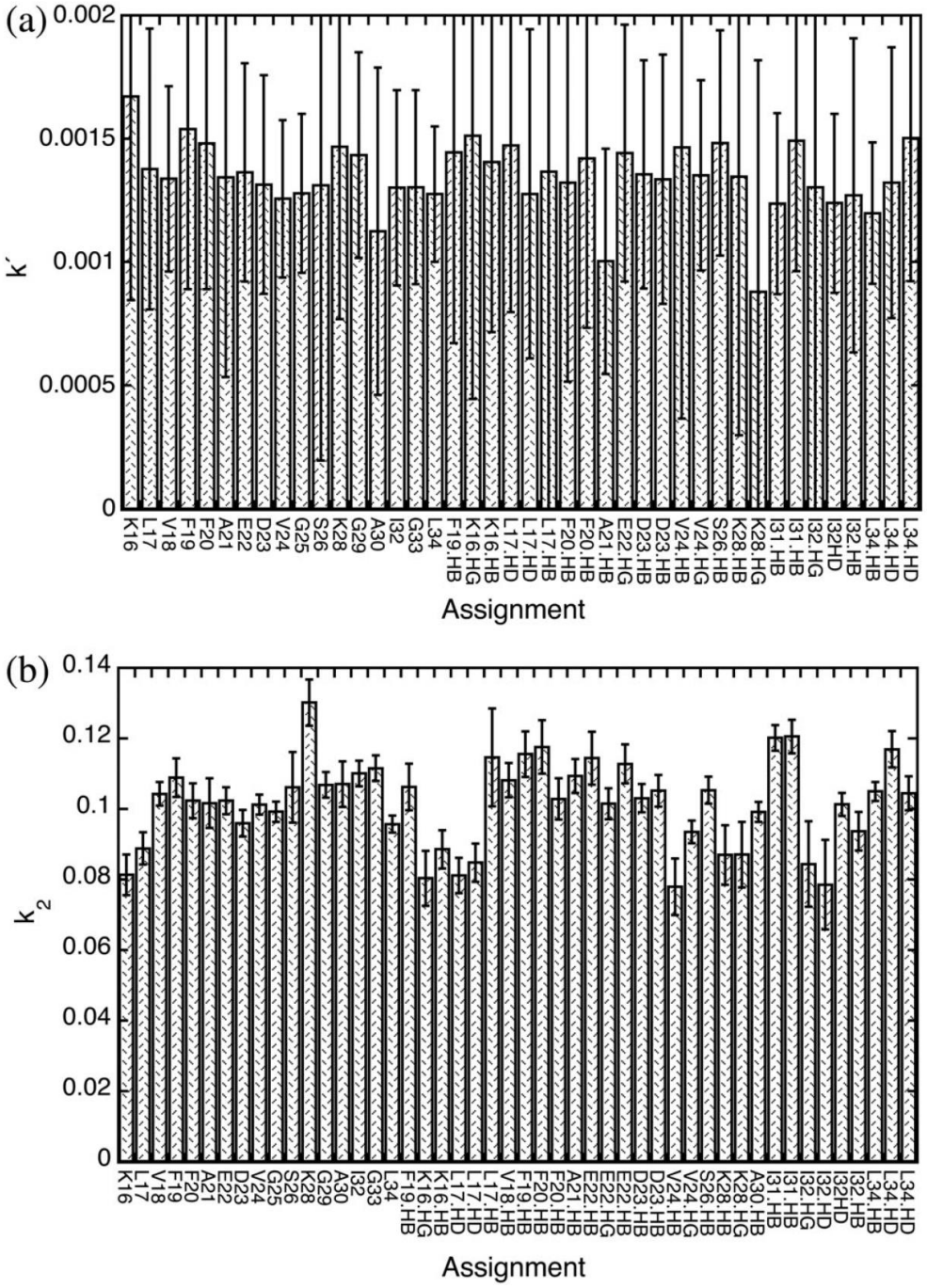

Figure 2.6 Rate constants obtained from analysis of serial TOCSY spectra of Cys-Aβ16–34. Data were analyzed as a combined second-order and pseudo-first-order approach to equilibrium, as described in text. Data represent means from three experiments on replicate samples; error bars are SDs for the rate constant parameter. (a) Pseudo-first-order rate constants. (b) Second-order rate constants. TOCSY, total correlational spectroscopy.

2.3 Discussion

In this article, we compared internal fragments of Aβ, all of which contain the central segment, Aβ21–30, a hydrophilic, flexible region which, in Aβ fibrils and some oligomers, forms a "bend" between the two parallel, in register β-sheets.[36,102–104] In the longer peptides, Aβ16–34 and Cys-Aβ16–34, as in Aβ1–40 and Aβ1–42, this central domain is flanked by stretches of hydrophobic amino acids. We compared Aβ16–34 to Cys-Aβ16–34 and found that the Cys residue increased the rate of fibril formation, and had other effects on kinetics (discussed further, below). Both peptides formed typical amyloid fibrils, as shown by ThT fluorescence and transmission electron microscopy. Both peptides were unstructured in solution by CD spectroscopy, and in ^{1}H,^{1}H-NOESY (and ^{1}H,^{1}H-ROESY) experiments, no long-range nOes were observed in any of the peptides examined. The results above demonstrate the following three points: 1. A putative structured core domain (Aβ21–30) is monomeric and highly soluble, and is unstructured by CD and NMR spectroscopy. Although in theory this region could serve as a "focal point" to organize aggregation, we saw no evidence for structure in Aβ21–30, nor in congeners of Aβ21–30 in which we attempted to stabilize marginally stable structures in Aβ21–30 by the addition of a Cys residue or cyclization. 2. Aβ16–34 and Cys- Aβ16–34, in which the above peptide is extended to include hydrophobic residues at each end, was able to aggregate and form typical amyloid fibrils. 3. The addition of a Cys residue to the N-terminus of Aβ16–34 yields a peptide, Cys-Aβ16–34, that fibrillizes more rapidly, and has a lower final solubility that Aβ16–34 itself. The kinetics of fibrillization was followed in serial NMR experiments. The more rapid fibrillization and lower final solubility were apparent in serial ^{1}H,^{1}H-TOCSY experiments, where the final peak volumes (Veq in Equations 2 and 7) were uniformly higher for Aβ16–34 than for Cys-Aβ16–34. No peak broadening was observed. The disulfide bond formed by Cys-Aβ16–34 appears to provide a "focal point" for rapid fibrillization of the peptide. Aβ16–34, lacking such a focal point, forms fibrils more slowly, and retains greater final solubility. In Cys-Aβ16–34, the N-terminal Cys allowed

formation of stable dimers, and once formed, these dimers fibrillized very rapidly. The disulfide bonded Cys residues, then, seemed to act as a “focal point” which organized the aggregation process. Once the disulfide was formed, the remainder of the peptide appears to “zip up” and form an insoluble fibril. Although there are no Cys residues in full-length Aβ peptides, of course, metal ions[41,105–114] or lipid surfaces,[15,115] among other heterogeneous nucleators could subsume the role of the Cys residue in Cys-Aβ16–34 and act as a “focal point” for aggregation of full length Aβ peptides. The formation of amyloids begins with nucleation, at which point the peptide begins to acquire β-sheet structure, developing in a previously unstructured peptide. The intermediates and final products in the process of fibril growth (extension) would be too large to observe by solution NMR. Thus, we infer that our observations bear upon the early stages of amyloid formation, including nucleation. We propose, then, that the nucleation of Aβ aggregation could consist of two theoretically distinct processes, illustrated in the scheme of Figure 2.7. Metal ions, for example, or other types of heterogeneous nucleators could lead to peptide-peptide association; this would, in turn, bring hydrophobic side chains close to one another and thereby favor a more stable complex made through the hydrophobic effect. An additional factor is the FF motif in full-length Aβ peptides and in Aβ16–34 and Cys- Aβ16–34, but not Aβ21–30: this motif has been shown to form 310 helices which can act as an oligomerizing precursor to amyloid fibrils, especially in a membrane environment.[116–119] As expected, NMR peak decay of Aβ16–34 and Cys- Aβ16–34 followed different kinetic schemes. The kinetics of peak decay for Aβ16–34 was consistent with a pseudofirst- order rate equation. In contrast, the kinetics of peak decay for Cys-Aβ16–34 was dominated by the formation of disulfide bonds, and hence by a second-order reaction. Addition of TCEP to Cys-Aβ16–34 reduced the level of disulfide bond formation and slowed the rate of decay of peak volumes. One of the fundamental features of amyloids is their structural polymorphism. At the same time, seeding solutions of an amyloidogenic peptide with fibril seeds tends to produce replicate fibrils,[57,58,60,61,75,120] indicating that much or most of this polymorphism arises during the nucleation phase, not during fibril

growth/extension. Furthermore, the degree of polymorphism is not necessarily the same for all amyloidogenic peptides, so there can be greater or lesser degrees of polymorphism for various amyloids. The kinetics of fibrillization of Aβ16–34 and Cys-Aβ16–34 suggest that in the latter peptide, there is a nidus at which aggregation starts, and this nidus not only accelerates but also orders the aggregation process. This could lower the degree of polymorphism of the latter peptide. For Aβ16–34, which lacks both the disulfide and the His residues that bind divalent metals ions in Aβ1–40, the eventual formation of fibrils appears to depend mainly on what remains in this peptide out of all the residues in Aβ1–40, that is, the hydrophobic (mainly aliphatic) amino acids. The hydrophobic amino acids are sufficient to lead to fibril formation of Aβ16–34, since Aβ21–30 and cyclo-Aβ21–30, lacking these residues, do not fibrillize at all. Fibrillization of Aβ16–34, however, is a slow and apparently random process that is delayed by the lack of a clearly defined starting point, which the Cys residue in Cys-Aβ16–34 or the metal ions in Aβ1–40 provides.

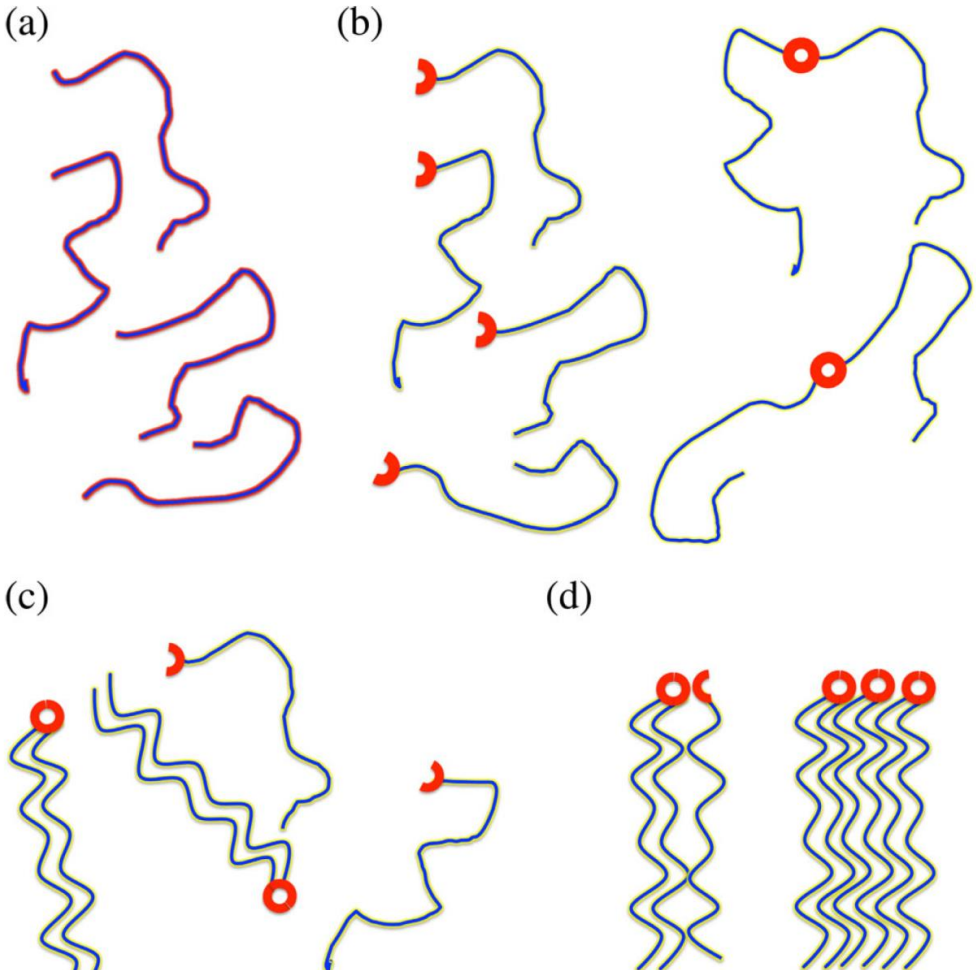

Figure 2.7 Schematic showing how the Cys residue in Cys-Aβ16–34 might accelerate and order fibrillization of this peptide compared with that of Aβ16–34. (a) Aβ16–34, containing no Cys or metal-binding sites, is unstructured in solution, and self-associates only through weak and nonspecific interactions, for example, between hydrophobic side chains. (b) Cys-Aβ16–34 is also unstructured in solution, but can form disulfide bonds.(c) Formation of disulfide bonds favors interactions between side chains and backbone moieties in the linked chain, and thus can serve as a nidus to accelerate and order formation of fibrils. (d) As additional molecules bind to this growing aggregate, with continued disulfide bond formation, the aggregate grows and precipitates

2.4 Materials and Methods

2.4.1 Synthesis of Linear Peptides

Peptides synthesized for these studies are depicted in Figure 2.1 and listed in Table SI 2.1. Peptides were synthesized using an Applied Biosystems 433A synthesizer (Foster City, CA) as previously described.[121] Briefly, peptides were synthesized with an Fmoc-Wang resin on a 0.25 mM scale with FastMoc chemistry, using Nhydroxybenzotriazole and 2-(1H-benzotriazol-1-yl)- 1,1,3,3,-tetramethyluronium hexafluorophosphate as coupling reagents (CSBio). Coupling times were extended by 3.3 times normal, and residues V18, V24, G25, S26, and N27 were doubly coupled. After synthesis, peptides were cleaved from the resin in 95% TFA, 2.5% water, and 2.5% triisopropylsilane (TIS) for Aβ21–30 and Aβ16–34; and in 94% TFA, 2.5% H2O, 2.5% TIS, and 1.0% ethanedithiol for Cys-Aβ21–30, Cys- Aβ16–34, and Aβ13–38 (all vol:vol). After 2 hr of cleavage, peptides were purified by reverse phase high performance liquid chromatography (HPLC), using a Preparative Zorbax C18 column, on a Hewlett- Packard 1050 HPLC, with a gradient between solvents A (0.1% [vol:vol] TFA in water) and B (0.1% TFA [vol:vol] in acetonitrile), the exact gradient depending on the peptide. Peptides were checked for purity (>95%) by analytical reverse phase (C18) HPLC and matrix-assisted laser desorption ionization-time of flight (MALDI-TOF) or electrospray ionization liquid chromatography (ESI LC)- mass spectrometry, as previously described.[121] All peptides were stored at −20°C or −80°C.

2.4.2 Synthesis of Cyclic Peptides

To make cyclic peptides, peptides were made with an N-terminal Cys residue, incorporated in place of one of the Ala residues (as indicated below), and a C-terminal thioester, so that cyclization could be carried out by a native chemical ligation reaction.[122–124] Thus, we synthesized NH–CEDVGSNKGA–SR, which is Aβ21–30, with Cys substituted for Ala21, and with a C-terminal thioester (R = leucyl mercaptopropionic acid). Peptide

chains were extended using optimized manual Boc Solid Phase Peptide Synthesis.57–59 Peptides were then simultaneously deprotected and cleaved from the resin by treatment with anhydrous hydrogen fluoride (HF) containing p-cresol (9:1, vol:vol) for 1 hr at 0C. After evaporation of the HF under reduced pressure, crude products were precipitated and triturated with chilled diethyl ether. The peptide products were then dissolved in 50% aqueous acetonitrile and purified, or lyophilized for storage. Cyclization was carried out by native chemical ligation, essentially as described elsewhere.[125,126] Briefly, peptides at 2 mg/ml were dissolved in 100 mM sodium phosphate, pH 7.20 and 10 mM TCEP. To monitor the course of the reaction, small aliquots of the reaction mixture were examined by analytical reverse phase-high performance liquid chromatography (RP-HPLC). Cyclization of the deprotected linear peptides was very efficient, taking less than 1 hr. After forming the cyclic peptide by native chemical ligation, Cys residues were converted to Ala by reductive desulfuration, essentially as described elsewhere.[127] Briefly, Raney nickel was prepared by adding 25 mg NaBH4 to 150 mg $Ni(OAc)_2(H_2O)_2$ dissolved in 2 ml of deionized H2O. After 5 min, the slurry was filtered through a medium sintered glass funnel. 0.5 mg of peptide was dissolved in 2 ml of 35 mM TCEP, 6 M urea and 200 mM sodium phosphate, pH 6.80. The Raney nickel slurry was added to the peptide solution. The reaction was monitored by HPLC using a C18 column maintained at 60°C, and using a 20:80 to 60:40 acetonitrile:H_2O (both 0.1% TFA, vol:vol) gradient. The peaks were checked using MALDI-TOF, or more recently, by LC-ESI mass spectrometry. Purification of cyclic peptides was essentially as described above. An example of this reaction is shown in Figure SI 2.21.

2.4.3 Electron Microscopy

Peptides were dissolved directly into 10 mM phosphate buffer, pH 7.20, 0.02% (wt:vol) NaN3 at room temperature to a final peptide concentration of 500 μM. A disaggregation procedure was not performed, because the goal of these experiments was to determine whether the peptides were capable of forming oligomers and fibrils at all. Solutions were

allowed to aggregate at 37°C for 48 hr. Then, solutions were centrifuged at 16,000g for 3 min. Most of the supernatant was discarded, and the remaining solution and fibrillar material was vortexed for 3 s. The slurries were then applied to glow-discharged, 400-mesh carbon-coated support films. All samples were stained with 0.1% (wt: vol) uranyl acetate. Excess solution was wicked off with paper tissue (Kimwipes), and the grids were dried at room temperature. Micrographs were taken on an FEI Tecnai F30st-STEM microscope at magnifications of ×15,000, ×49,000, and ×98,000. The CCD camera multiplied the magnification by a factor of ×1.4.

2.4.4 Circular Dichoric Spectroscopy

Samples were freshly prepared at peptide concentrations of 100–500 μM in 10 mM phosphate buffer, pH 7.20, 0.02% (wt:vol) NaN_3. In general, freshly dissolved samples were used, because at higher concentrations (≥300 μM) of Aβ16–34 and Aβ13–38, fibrils formed to some extent after an incubation of 4–6 hr. Samples were centrifuged at 16,000g for 3 min prior to measuring the spectra, and only the supernatant was examined. CD spectra were recorded using an Aviv (Lakewood, NJ) model 202 spectropolarimeter with a temperature-controlled cuvette holder. Three hundred microliters of each sample was added to a 0.1 cm path-length cell (Starna), and three scans were obtained from 280 to 180 nm at intervals of 1 nm with a 2 s averaging time. The temperature of the cuvette holder was 25°C. The bandwidth was 1 nm. Data were subsequently processed by zeroing each spectrum individually by subtracting the solvent baseline, and averaging the three spectra. Ellipticities were converted to mean residue ellipticities (deg cm^2 $dmol^{-1}$).

2.4.5 Size Exclusion Chromatography

Fresh solutions of Aβ21–30, Aβ16–34, and Cys-Aβ16–34 at concentrations from 100 to 500 μM were prepared in 10 mM phosphate buffer, pH 7.20, 0.02% (wt:vol) NaN3 immediately prior to chromatography. To calibrate the column, molecular weight standard

peptide solutions (100 µl, 1 mg/ml) and glycine (100 µl, 1 mg/ml) were injected onto a Superdex Peptide 10/300 column (GE Healthcare) attached to an Agilent model 1100 HPLC. Chromatography of Aβ21–30, Aβ16–34, and Cys- Aβ16–34 was performed using a mobile phase of 10 mM sodium phosphate, pH 7.40 (also containing 0.02% NaN3, wt:vol); flow rate was 0.5 ml/min. Column temperature was room temperature (generally 22°C), and the effluent was monitored at by UV absorbance at 220 nm. In some experiments, as indicated in Section 2.2, 0.1% (vol:vol) β-ME was included in the solvent.

2.4.6 Analytical Ultracentrifugation

Fresh samples of Aβ21–30 and Aβ16–34 were prepared in 10 mM sodium phosphate, pH 7.20, 0.02% (wt:vol) NaN_3 to a concentration of 250 µM. A buffer blank was also prepared. In order to avoid contamination by dust or other large particles, samples centrifuged twice at 16,000g for 3 min, followed by filtration through a 0.22 µm syringe filter (Corning; Corning, NY) into a separate, autoclaved Eppendorf tube. The samples were then centrifuged at the Biophysical Core Facility at the University of Chicago, at 36,000 rpm for 72 hr, at 20°C. UV scans were measured every 2 hr at 220 and 235 nm. Equilibrium was attained in this time, as shown by the lack of change in the absorbance gradient over the previous 24 hr. Apparent molecular weights were obtained from the equation:

$$ln(A) = \frac{M(1 - \bar{v}p)\omega^2 r^2}{2RT} + C$$

where A = absorbance, M = weight-averaged molecular weight, v = partial specific volume, ρ = solvent density (1.02 g/cm3), ω = angular velocity (rad/s), r = distance from the center of rotation (cm), R = gas constant = 8.3 × 107 $ergK^{-1}$ mol^{-1}, T = 293 K, and C = integration constant. Partial specific volume was determined from amino acid composition using the program SEDNTERP (for discussion, see Reference [128]). For Aβ21–30 and Aβ16–34, these values were 0.698 and 0.770, respectively. In each case, three separately made samples were analyzed, and the results were aggregated to calculate M.

2.4.7 Peptide aggregation by sedimentation assay with SEC

Aggregation of peptides into fibrils was measured using a sedimentation assays (for example, see Reference[95]). For a typical aggregation assay, 5 mg of lyophilized, HPLC purified Aβ16–34 or Cys-Aβ16–34 was dissolved in neat DMSO to a concentration of 1.5 mM, and divided into two replicate solutions. Peptide concentrations were calculated from absorbance at 257 nm (extinction coefficient = 400 M^{-1} cm^{-1}, due to the two Phe residues), and in the case of Cys-containing peptides, using the Ellman assay (see below). To start aggregation, 50 mM sodium phosphate, pH 7.40, was added to give the desired peptide concentration, typically 100 μM. Peptide was incubated at 4C. Because the second replicate solution could not be analyzed simultaneously with the first, the second replicate solution was initially stored at 4C, and pH 2–3 for 60min (the length of time needed to analyze the first sample chromatographically) before adding buffer to raise the pH. The two samples, although treated slightly differently, gave essentially identical results. Immediately after adding buffer, and at various times thereafter, 100 μl aliquots were removed, centrifuged for 10 min at 15,000g; the top 50 μl was removed and injected onto a Superdex Peptide 10/300 column, as described above. The peak areas corresponding to monomeric, dimeric, and oligomeric peptide were recorded as a function of time. As described in Section 2.2, Aβ16–34 showed only a monomer peak, whereas some samples of Cys-Aβ16–34 showed monomer, dimer, and oligomer peaks.

2.4.8 ThT Fluorescence

In some instances, ThT fluorescence of precipitates was measured using standard assays,[129,130] in order to document that the precipitates were amyloids. In some ThT fluorescence experiments on Cys-Aβ16–34, indicated in Section 2.2, 0.1% (vol:vol) β-ME was included in the solvent. Peptide concentrations, solvents, and other conditions were as described in the previous section. As previously described56 (see Figure 2.3a), for peptides showing a lag phase in aggregation, kinetics were analyzed using a stretched

exponential equation; for peptides aggregating without a lag phase, the equation of a first-order approach to equilibrium was used.

2.4.9 Dissolving peptides for NMR Experiments

In general, the goal in dissolving the various Aβ peptides was to obtain as complete disaggregation as possible. Accordingly, the following procedure was followed in most cases: peptide was dissolved initially in neat HFIP, and then lyophilized (the shorter Aβ peptides [Aβ21–30 and cyclo-Aβ21–30] required no such disaggregation procedure and the same results were obtained with or without such a procedure). The lyophilized powder was then dissolved in neat DMSO (for NMR, D6-DMSO). In kinetics experiments, described below, aggregation was initiated by diluting this solution with 0.05 M sodium phosphate, pH 7.40 so that the final peptide concentration was 100 μM and DMSO concentration was 2% (vol: vol). Because of residual TFA from peptide purifications, the final pH was 7.1 as measured by microelectrode, and in some cases, by the position of 0.5 mM Tris and/or (4-(2-hydroxyethyl)-1-piperazineethanesulfonic acid) (HEPES) added to the sample as a pH indicator.[131] Any undissolved material (generally not visible) was removed by centrifugation (16,000g). Initially, an approximate peptide concentration was determined initially by A257 using $\varepsilon = 1{,}400 M^{-1}\ cm^{-1}$. Actual final peptide concentration was determined by Bradford assay calibrated by amino acid analysis of at least triplicate samples. For some experiments, for example, obtaining natural abundance $^{1}H,^{15}N$- and $^{1}H,^{13}C$-HSQC spectra, peptide concentration was considerably higher, up to 3 mM for Aβ21–30 and its variants, and 300 μM for Aβ16–34 or Cys-Aβ16–34. $^{1}H,^{1}H$-TOCSY, -ROESY,[132,133] and -NOESY, and $^{1}H,^{15}N$and $^{1}H,^{13}C$-HSQC spectra were acquired at the NMR Facility of the University of Chicago, using either a 500 or 600 MHz Bruker Avance spectrometer (with Topspin 3), at temperatures from 5°C to 35°C, as indicated in Section 2.2. NMR assignments were obtained at 5–25°C in 5°C increments. Spectra were processed using either TopSpin or NMRPipe,[134] and further analyzed using Sparky, NMRView (from One Moon Scientific, Inc.), and CARA.[135]The spectra were referenced using

sodium trimethylsilylpropanesulfonate (DSS).

2.4.10 Serial measurements of 2D homonuclear correlation spectra

Serial ^{1}H,^{1}H-TOCSY, and in some cases, serial ^{1}H, ^{1}H-NOESY or ^{1}H,^{1}H-ROESY spectra were obtained for two reasons. First, serial spectra were obtained to observe decay of peaks, associated with aggregation, at a site-specific level. In these experiments, lyophilized peptides were dissolved as described above. Serial TOCSY spectra were obtained every 1.5 hr for 1–5 days (the length of the experiment depended on the rate of fibrillization); serial NOESY spectra required 3 hr per spectrum. Periodically, 1D ^{1}H spectra were obtained between serial TOCSY or NOESY spectra. Equations for analyzing these kinetics data are given in Section 2.2. The units of peak areas and volumes are referred to simply as Area or VU, and are not otherwise defined. In general, all kinetics experiments were performed on three replicate samples of peptide solution, and the results presented represent mean values obtained for the three replicates. Second, as will be described in Section 2.2, no long range nOes or rOes were observed in the spectra of any of the peptides examined, including Aβ21–30, Cys- Aβ21–30, cyclo-Aβ21–30, Aβ16–34, and Cys-Aβ16–34. On the possibility that such nOes or rOes appeared in spectra only transiently, however, we assessed changes in these spectra over time, by acquiring serial spectra (^{1}H,^{1}H-TOCSY and -NOESY). As described in Section 2.2, no new peaks developed over the course of these experiments.

2.4.11 TALOS+ torsional angle estimates and PyMol plotting

Chemical shift data for ^{1}H, ^{15}N, and ^{13}C atoms were obtained from NMR peak assignments for each backbone residue and corresponding side chains for Aβ21–30,cyclo-Aβ21–30, Aβ16–34, and Cys-Aβ16–34. These chemical shift data were then uploaded to the TALOS+website[136,137] (http://spin.niddk.nih.gov/bax/nmrserver talos/) for data processing, to obtain information on backbone residue torsional angles and secondary struc-

ture probabilities, with S2 values indicating strength of prediction.[138]

2.4.12 Measurement of disulfide bond formation by thiol assays

For the Cys-containing peptide, Cys-Aβ16–34, the rates of disulfide bonds formation were measured under the same conditions that were used for measurements of serial NMR spectra. After making solutions of Cys-Aβ16–34 described above, the solution was divided among three glass vials, each containing 200 µl. To initiate formation of disulfide bonds, 20 µl of 100 mM sodium phosphate, pH 7.40, was added to each tube. Thiols were assayed using the Ellman reagent at t = 0, and again at various intervals.[139–141] For the Ellman test, a stock solution of 40 mg of Ellman reagent (5,50-dithiobis-(2-nitrobenzoic acid)) was made in 10 ml of sodium phosphate, pH 8.00, and stored at 4C. For each assay, 33 µl of this stock solution was mixed with 20 µl of sample and 922 µl of 0.1 M sodium phosphate, pH 8.50. This mixture was allowed to react at room temperature for 15 min, and then absorbance at 412 nm was measured; a buffer control was subtracted from this value at each time point. Concentration of free thiol was calculated using an extinction coefficient (for the thiolate of Ellman reagent) of 14,150 M^{-1} cm^{-1}.

2.4.13 SDS-PAGE of Cys-Aβ16–34 after serial TOCSY spectra

To assess the proportion of monomeric and disulfidelinked dimeric Cys-Aβ16–34 in pellet and supernatant after serial TOCSY experiments, the peptide was first centrifuged at 16,000g and divided into supernatant and pellet, and each fraction was analyzed by Tris-tricine SDSPAGE[142] of Cys-Aβ16–34. To obtain a dimer standard for SDS-PAGE, Cys-Aβ16–34 was oxidized using H2O2 by the method of Sidova et al.[143] Experimental details and the results are presented in Supporting Information.

2.5 Supporting Information

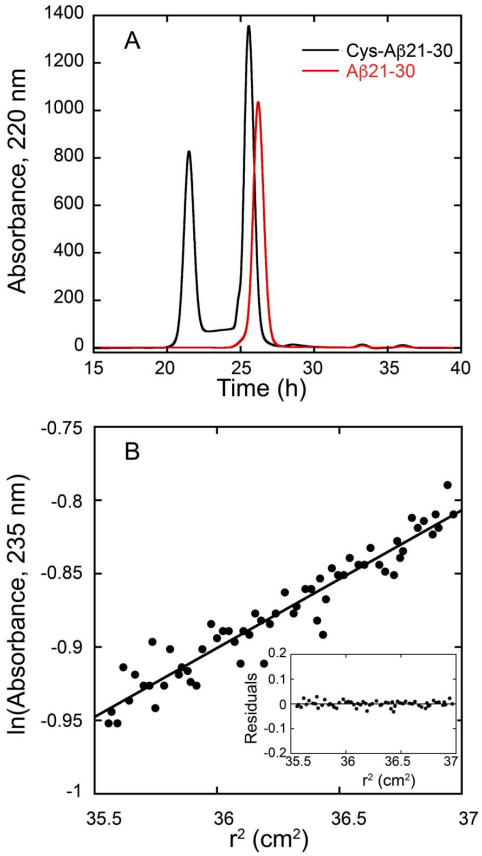

Figure 2.8 (A) Size exclusion chromatography Aβ21-30, using a Superdex Peptide 10/300 column (GE Healthcare) attached to an Agilent model 1100 HPLC. Eluent was 50 mM phosphate buffer, pH 7.20, 0.02% (w:v) NaN_3.From the calibration curve (not shown), the peptide elutes as a single peak with an apparent molecular weight of 103, consistent with monomer. Also shown is Cys-Aβ21-30, which has peaks of monomeric and dimeric peptide. (B) Analytical ultracentrifugation (sedimentation equilibrium) of Aβ21-30. The line represents the best fit of experimental points to the equation:

$$ln(A) = \frac{M(1-\bar{\nu}p)}{2RT} + C$$

where A = absorbance, M = weight-averaged molecular weight, $\bar{\nu}$ = partial specific partial specific volume, ρ = solvent density (1.02 g/cm^3), □ = angular velocity (rad/s), r = distance from the center of rotation (cm), R = gas constant = 8.3*10^7 erg K^{-1} mol^{-1}, T = 293 K, and C = integration constant. The inset shows the residuals. From this analysis, we obtained M = 963 (calculated molecular weight = 947.0 g mol^{-1}).

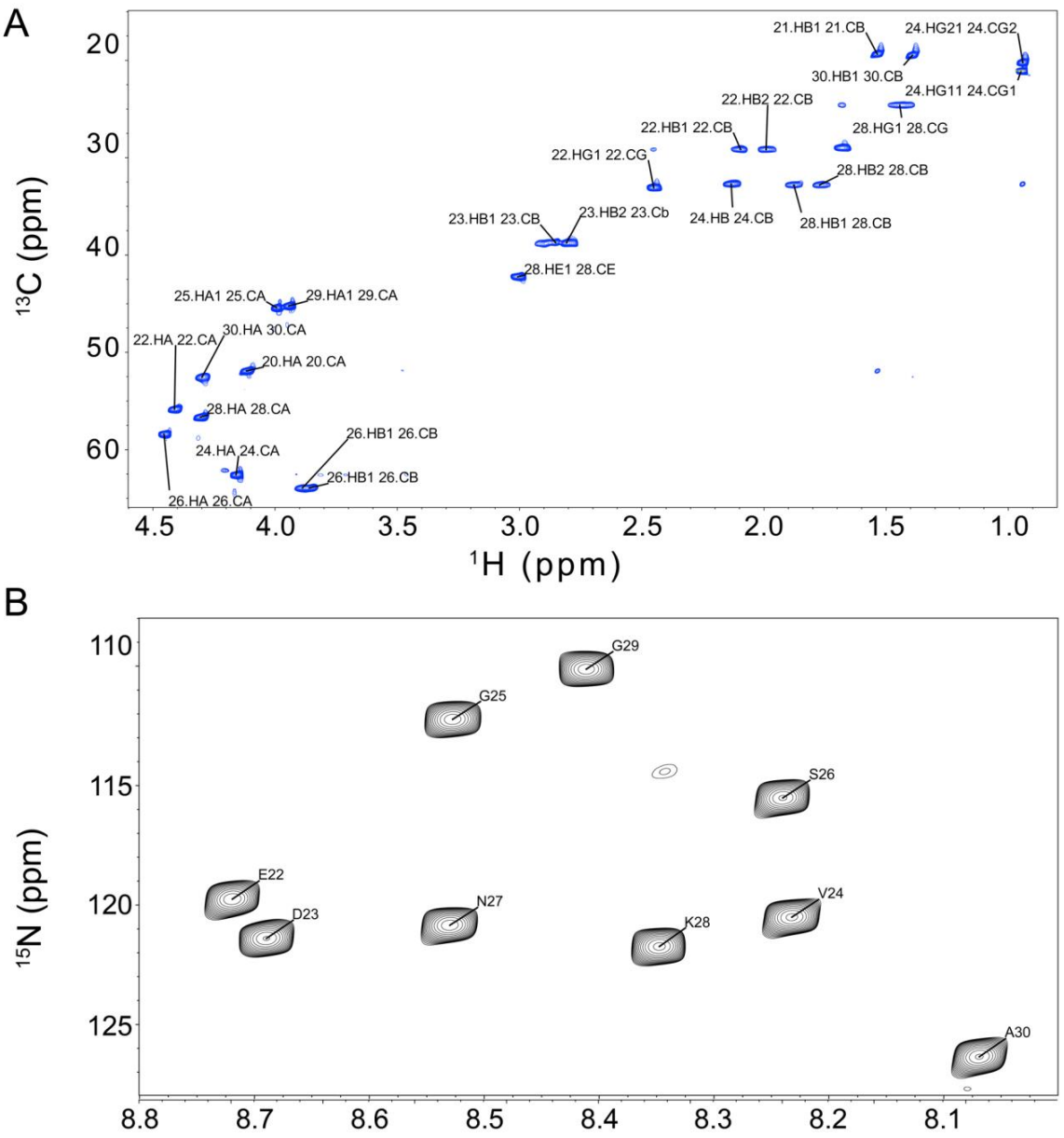

Figure 2.9 (A) ^{1}H,^{13}C-HSQC spectrum of Aβ21-30, with assignments.(B)^{1}H,^{15}N-HSQC spectrum of Aβ21-30 with assignments.

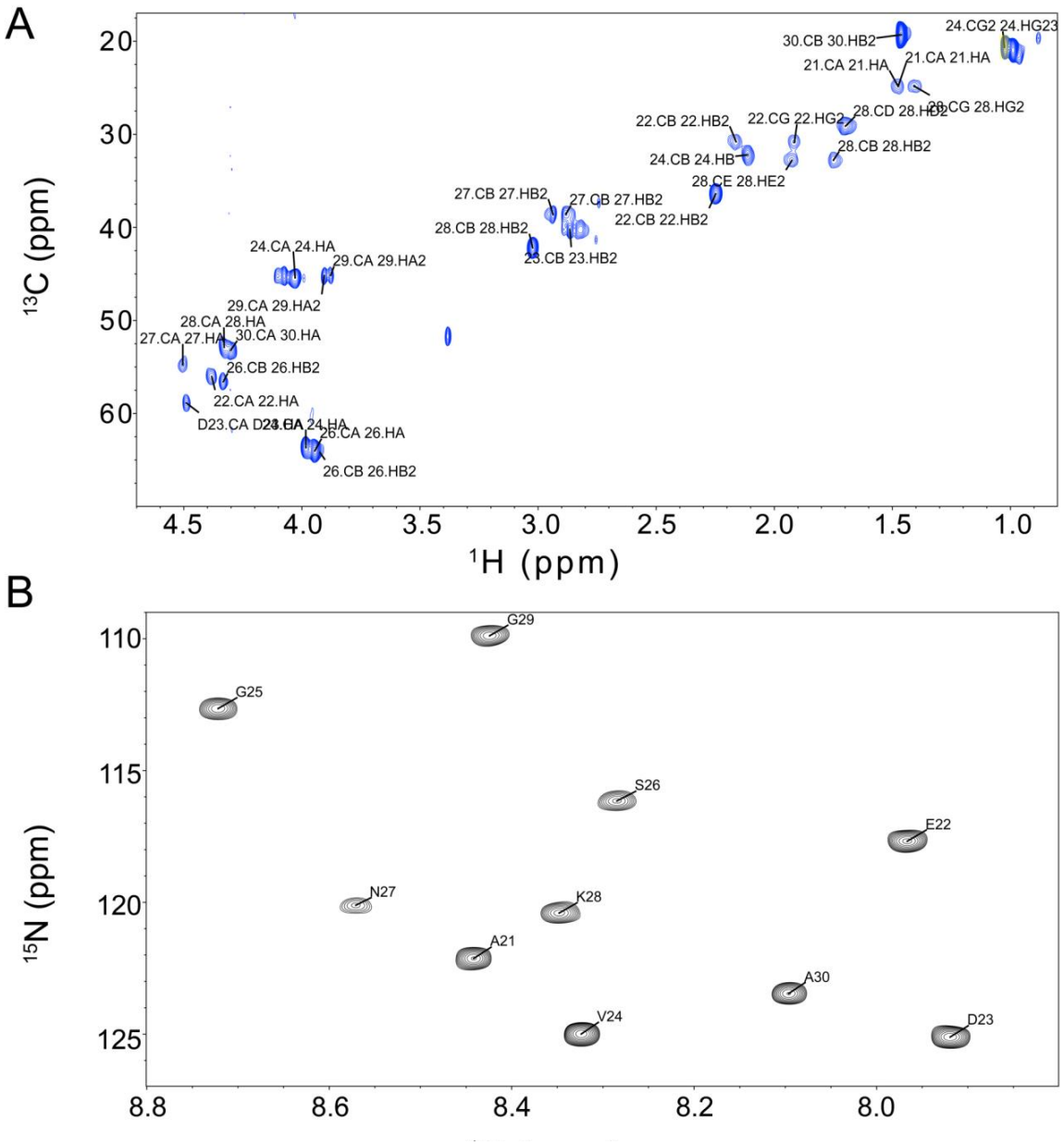

Figure 2.10 (A) ^{1}H,^{13}C-HSQC spectrum of cyclo-Aβ21-30, with assignments. (B) ^{1}H,^{15}N-HSQC spectrum of cyclo-Aβ21-30 with assignments.

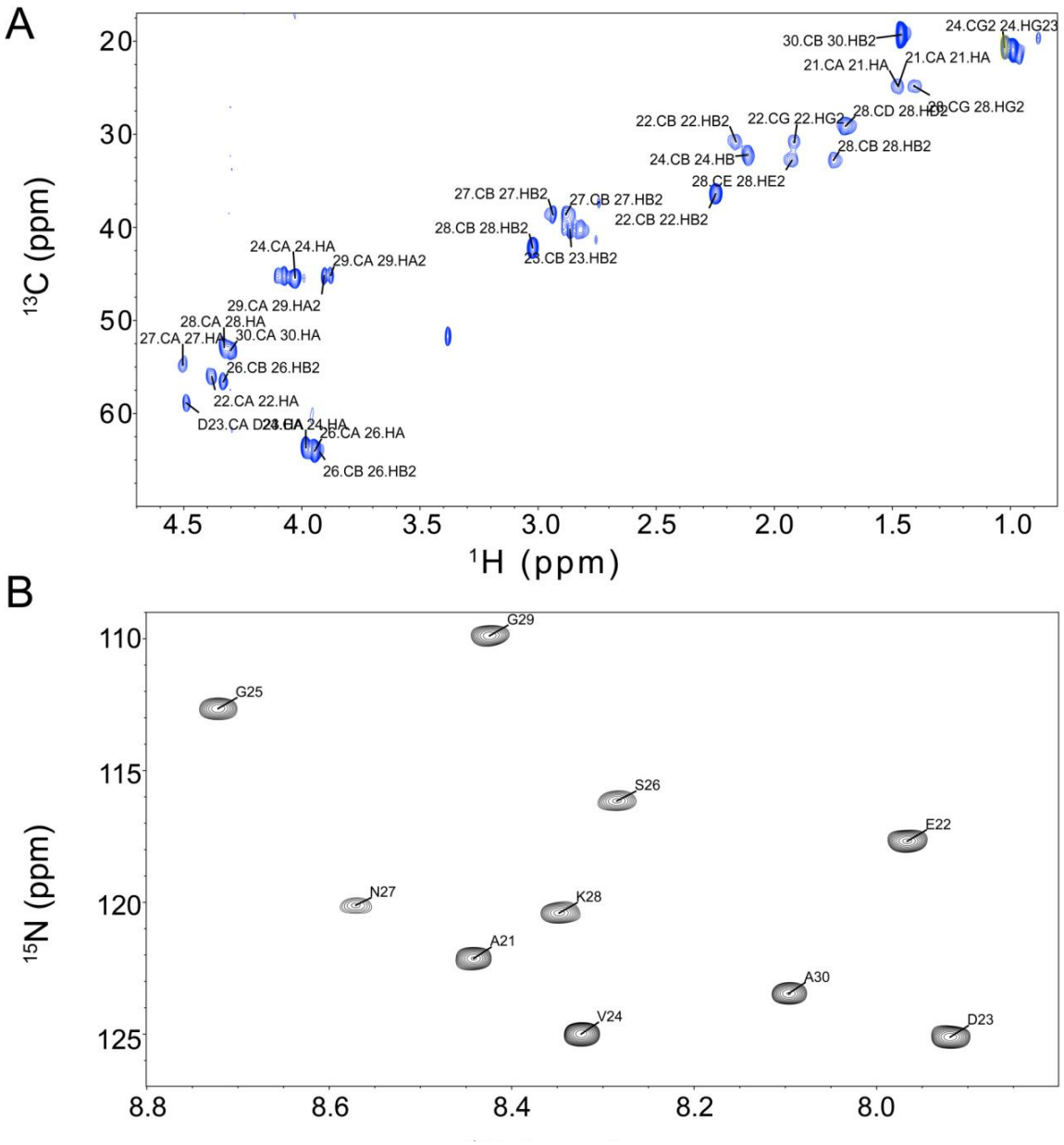

Figure 2.11 ^{1}H,^{1}H-TOCSY (A) and -NOESY (B) spectra of Aβ16-34. Peptide was at 100 μM, 50 mM sodium phosphate, pH 7.4, 15°C

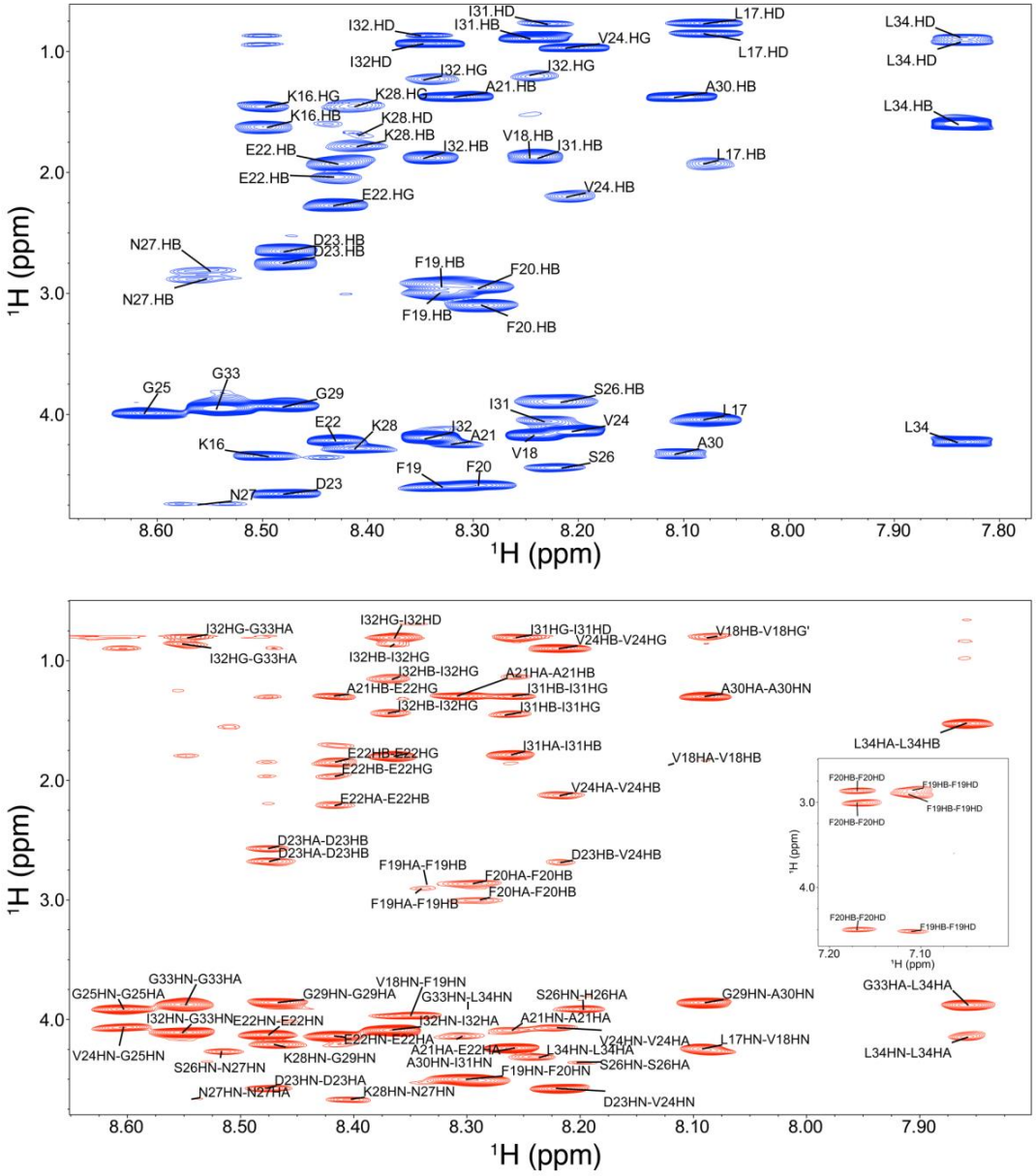

Figure 2.12 ^{1}H,^{1}H-TOCSY (A) and -NOESY (B) spectra of Cys-Aβ16-34.Peptide was at 100 μM, 50 mM sodium phosphate, pH 7.4, 15°C.

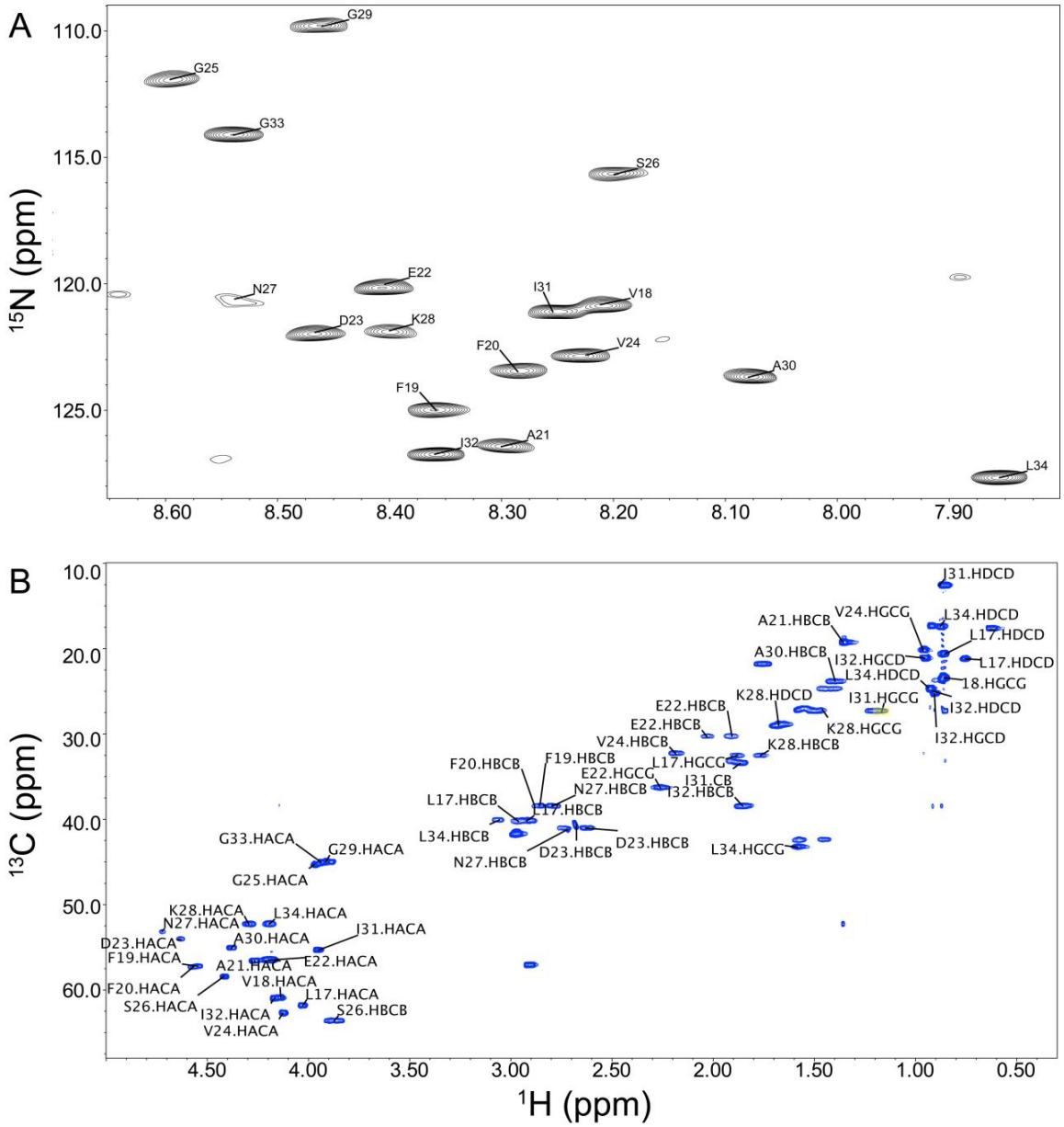

Figure 2.13 ^{1}H,^{15}N-HSQC (A) and ^{1}H,^{13}C-HSQC (B) spectra of Aβ16-34.Peptide was at 100 μM, 50 mM sodium phosphate, pH 7.4, 15°C.

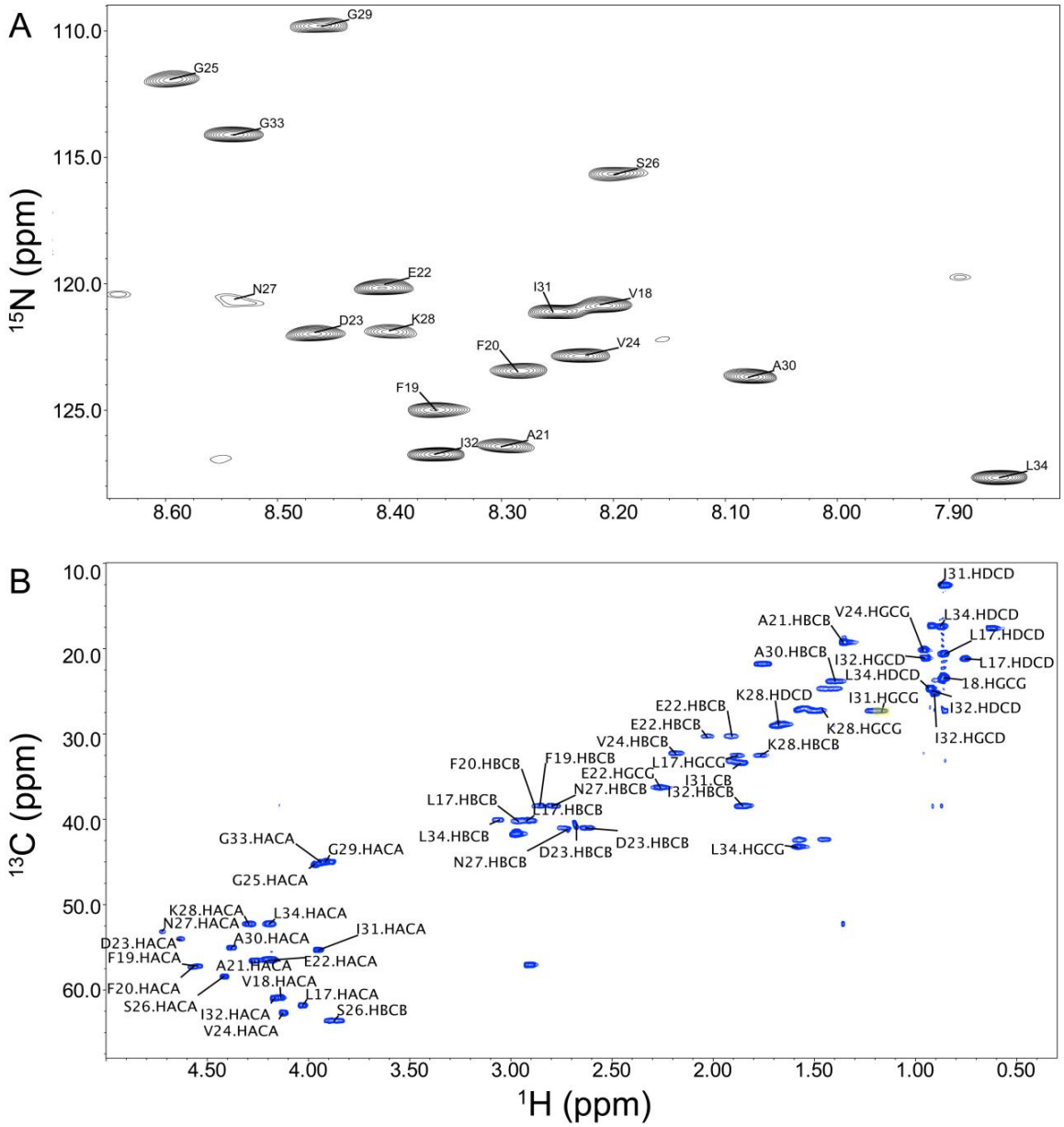

Figure 2.14 ^{1}H,^{15}N-HSQC (A) and ^{1}H,^{13}C-HSQC (B) spectra of Cys-Aβ16-34.Peptide was at 100 μM, 50 mM sodium phosphate, pH 7.4, 15°C.

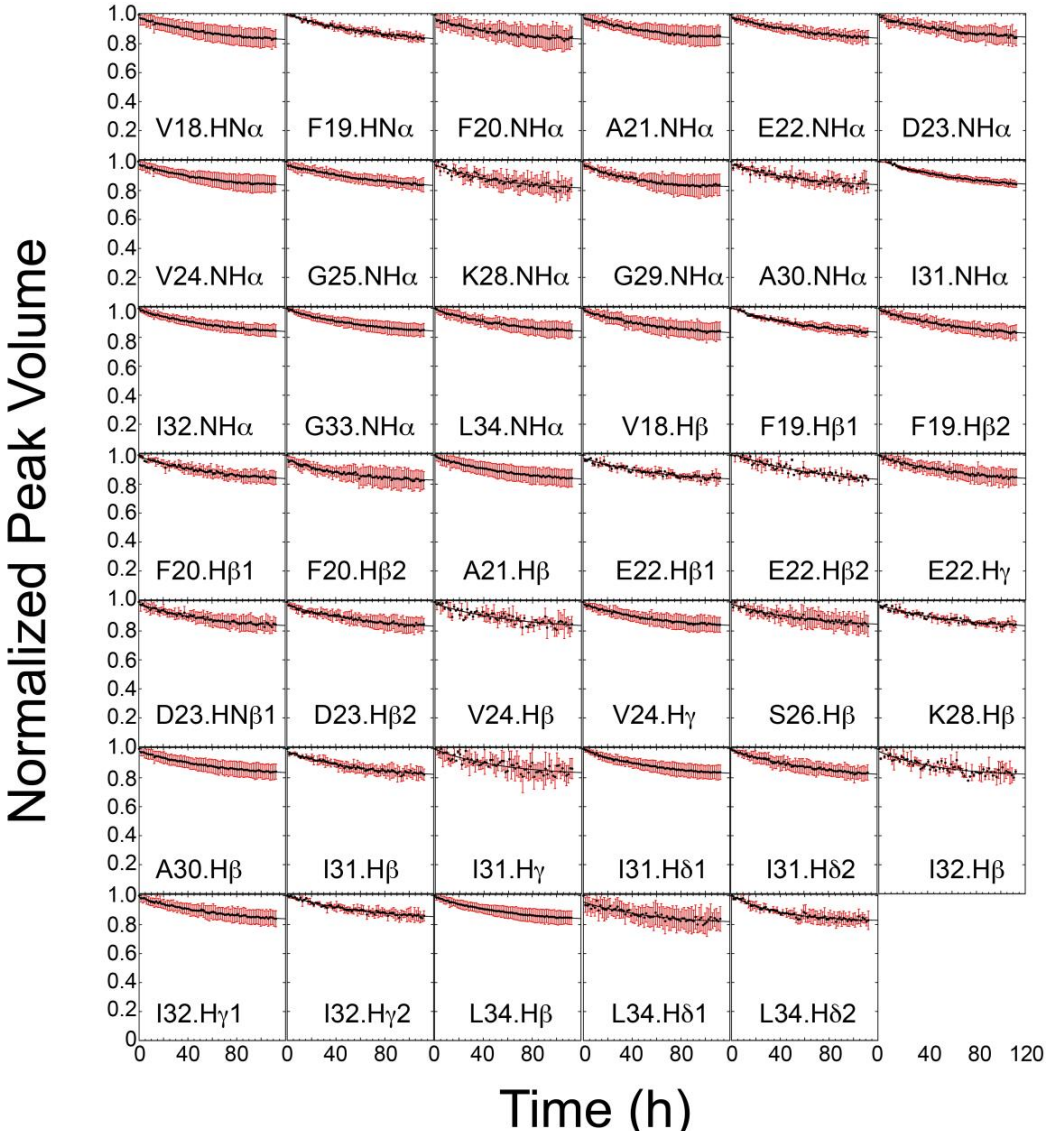

Figure 2.15 Decay of peak volume with time for individual peaks in serial 1H,1H-TOCSY experiments on Aβ16-34, under conditions described in the text. Peak volumes were analyzed using Equation 2, i.e., pseudofirst-order approach to equilibrium. Each graph represents the mean results in three separate experiments, i.e., three separate samples. Error bars are the standard deviations on each mean value.

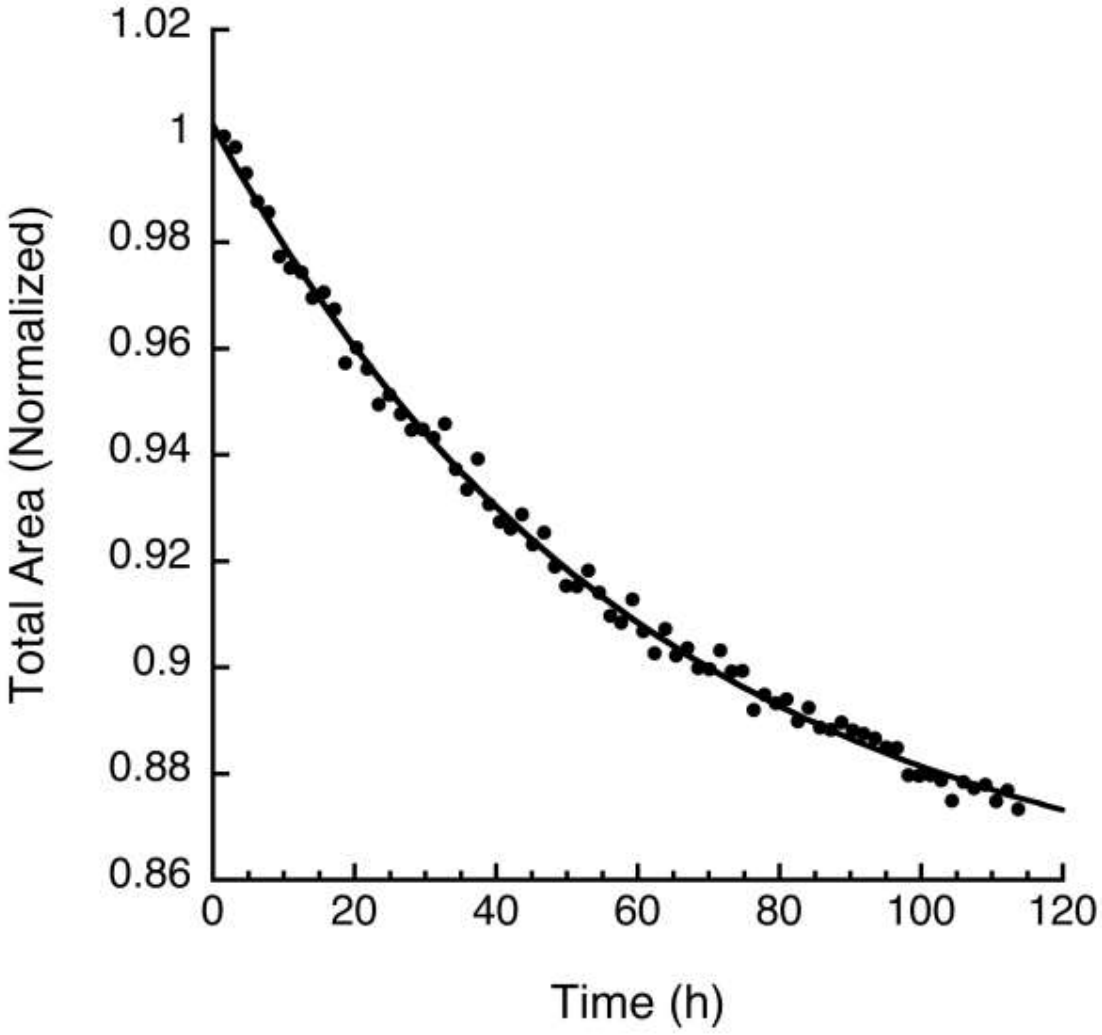

Figure 2.16 Decay of peak intensities in ^{1}H-1D spectra of Aβ16-34, under the conditions described in the text. Spectra were converted to numeric files using the command "convbin2asc" in TopSpin or using an in-house program. The portions of the spectra from 7 to 9 ppm were integrated using an in-house program; these values are plotted in the graph. Kinetics was that of a pseudofirst-order approach to equilibrium, Equation 2 in the main text. The rate constant was 0.026 h^{-1}, Aeq was 0.88 (when A0 was normalized to 1), i.e., most of the peptide remained in solution.

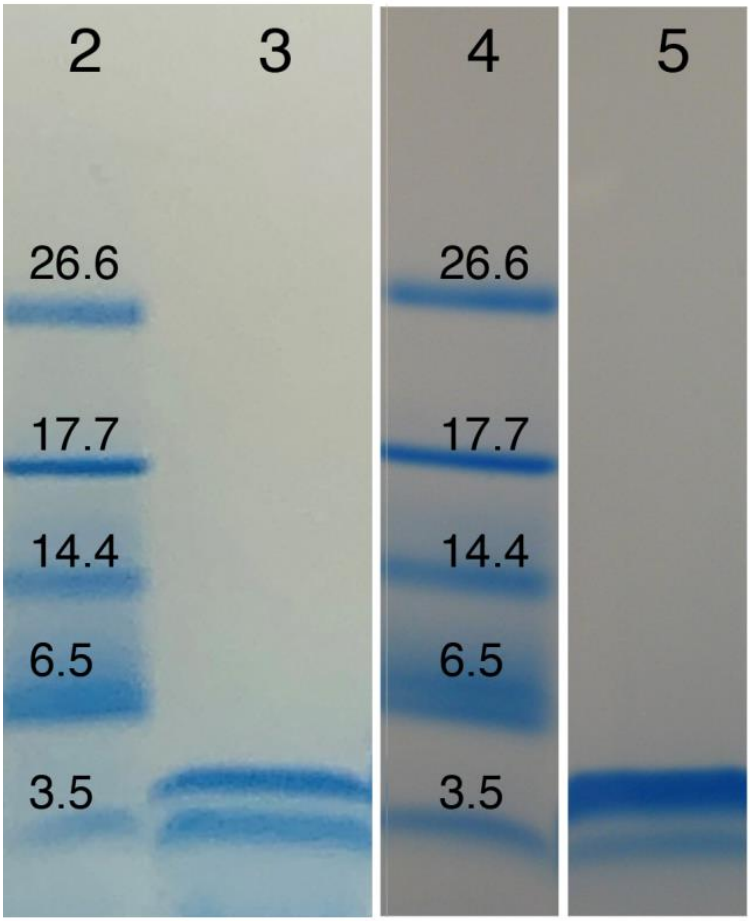

Figure 2.17 Tris-tricine SDS-PAGE[144] of Cys-Aβ16-34. Lanes 1-3: Peptide was removed from the NMR tube after 72 h of a serial TOCSY NMR experiment, centrifuged at 16,000 x g, and divided into supernatant and pellet. Protein (fibrils) in the pellet (lane 1) was dissolved in SDS-PAGE sample buffer and 1 µL was loaded onto the gel. Protein in the supernatant was concentrated by lyophilization, and then dissolved directly into 100 µL of sample buffer without reductant; 4 µL was loaded onto the gel (lane 3). In all cases, sample buffer was 450 mM Tris-HCl, 12% (v:v) glycerol, 4%(w:v) SDS, 0.0025% (w:v) Coomassie Blue G, 0.0025% (w:v) Phenol Red, pH 8.45. Lanes 4 and 5 are from another gel (with an intervening lane removed). Lane 5 is a sample of Cys-Aβ16-34 dimerized using the method of Sidova et al. (77). Briefly, solid peptide was dissolved in 100 µL of the following: 96.33 µL of 50 mM sodium phosphate (pH 7.4) + 1 µL of 0.3% (v:v) H_2O_2 + 1.5 µL of methanol + 1.17 µL of 17% (v:v) SDS. This mixture was incubated at 20°C for 40 minutes, after which it was analyzed by SDS-PAGE. Lanes 2 and 4 are molecules weight markers (BioRad), as indicated.

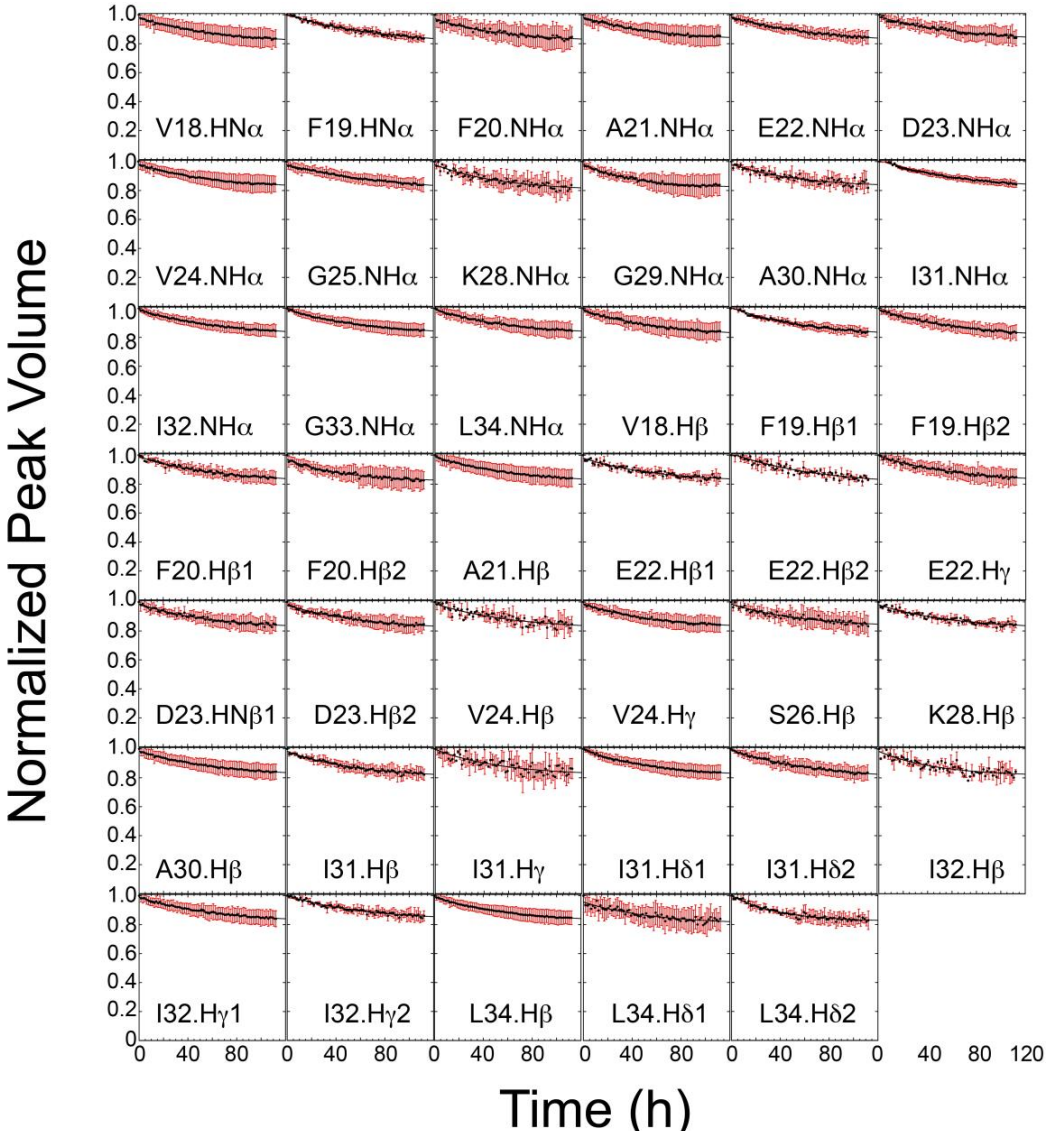

Figure 2.18 Decay of peak volume with time for individual peaks in serial $^{1}H,^{1}H$-TOCSY experiments on Cys-Aβ16-34, under conditions described in the text. Peak volumes were analyzed using Equation 7, i.e., parallel pseudofirst- and second-order reactions. Each graph represents the mean results in three separate experiments, i.e., three separate samples. Error bars are the standard deviations on each mean value.

2.6 Akaike Information Coefficient and Likelihood Functions

We calculated the Akaike Information Coefficient (AIC), i.e., AIC = n*log (SS) + m, where n=number of points, SS = sum of squares, and m = number of parameters.[98–100]

By this criterion, the above equation, which contains four parameters, still provides a better fit than the simpler second-order approach to equilibrium (the equation of which has three parameters). The pseudofirst-order rate constants are underdetermined and contributed less to the overall rate than the second order rate constants, however. The error bars in Figure 2.6A (representing errors on the pseudofirst-order rate constants obtained from curve fitting) are larger than those in Figure 2.6B (representing errors on second-order rate constants). That the pseudofirst-order rate constants were less important to the overall rate than second-order rate constants was also shown by the following.

The data from signals for each residue were fit to a kinetic model by calculating the likelihood function[101–103] that the model parameters (k_1, k_2, A_0, A_{eq}, σ; i.e., the 1st and 2nd order rate constants, the initial and equilibrium peak volumes, and the noise in these volumes) describe the measured values of peak intensity, f(measured,i). The likelihood function, P, is given by:

$$P = \frac{N}{\sigma^{n+2}} e^{-0.5\chi^2} \qquad \text{(Equation S1)}$$

where

$$\chi^2 = \frac{\sum_{i=1}^{n} (f_{\text{measured,i}} - f_{\text{simulated,i}})^2}{\sigma^2} \qquad \text{(Equation S2)}$$

where n is the number of data points measured, and N is a normalization factor that normalizes the total probability to one. $f_{(\text{simulated,i})}$ is the simulated volume of the peak, calculated from the 2nd order or combined 1st and 2nd order models presented above. The 2nd order model has one less parameter (it does not have the parameter k1) than the combined model. The likelihood function, P, is calculated on a grid of parameter values

using the program Mathematica. The maximum of P gives the most likely values of the parameters, while the distribution of P with the parameters determined their errors. A typical result of this analysis is given for the TOCSY peak, A21.HN-A21.HA, in Supporting Figure SI 2.19, below.

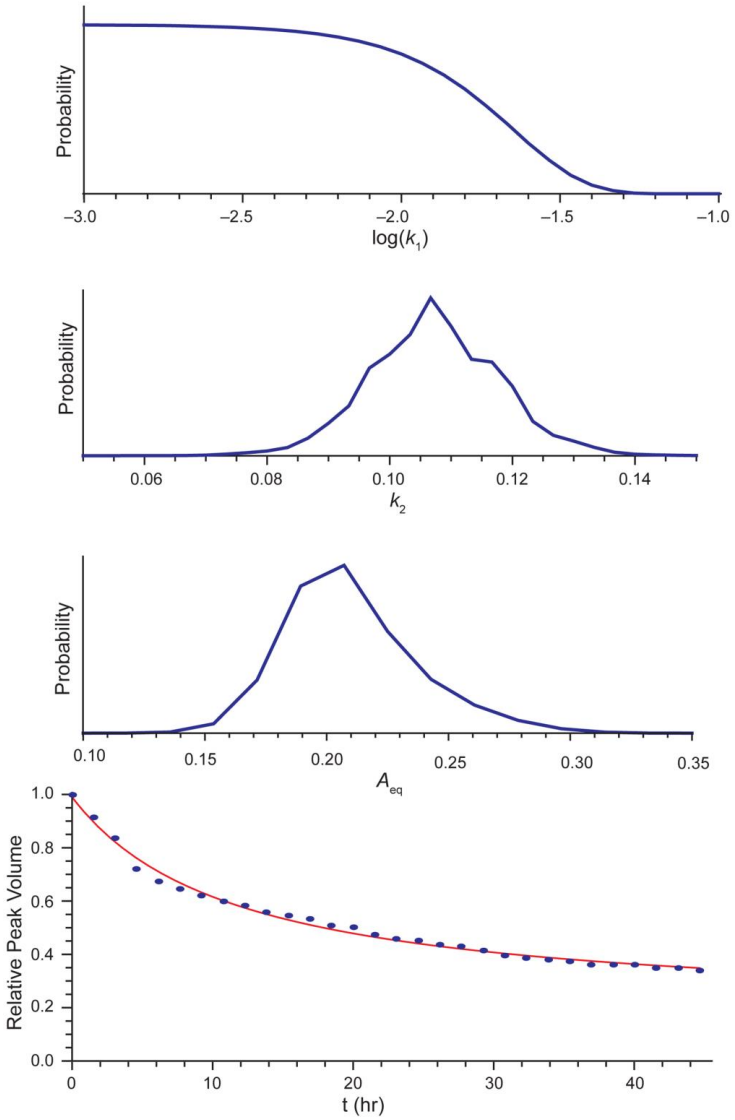

Figure 2.19 Result of likelihood function analysis for the decay of the HN-HA cross peak of Ala21 in serial TOCSY spectra of Cys-Aβ16-34. Data were analyzed by Equation S1, above. The model parameters (k_1, k_2, A_0, A_{eq}, σ; i.e., the 1st and 2nd order rate constants, the initial and equilibrium peak volumes, and the noise in these volumes) were analyzed. The top three panels show the probabilities of k_1, k_2 and A_{eq} given the decay data, while the bottom panel shows the best fit to these data. The probability distributions provide a measure of the best fit value and the error in these values. Most significantly, while we found by comparing pure second-order kinetics to a mixture of pseudofirst- and second-order kinetics that the mixed kinetic model better described the data, a precise value of k_1 was not determined. The top panel shows that its value must be below $10^{-1.7}$ h^{-1}, while the second and third panels show that the values for k_2 and A_0 are well defined. This analysis confirms that the reaction is dominated by the second-order process.

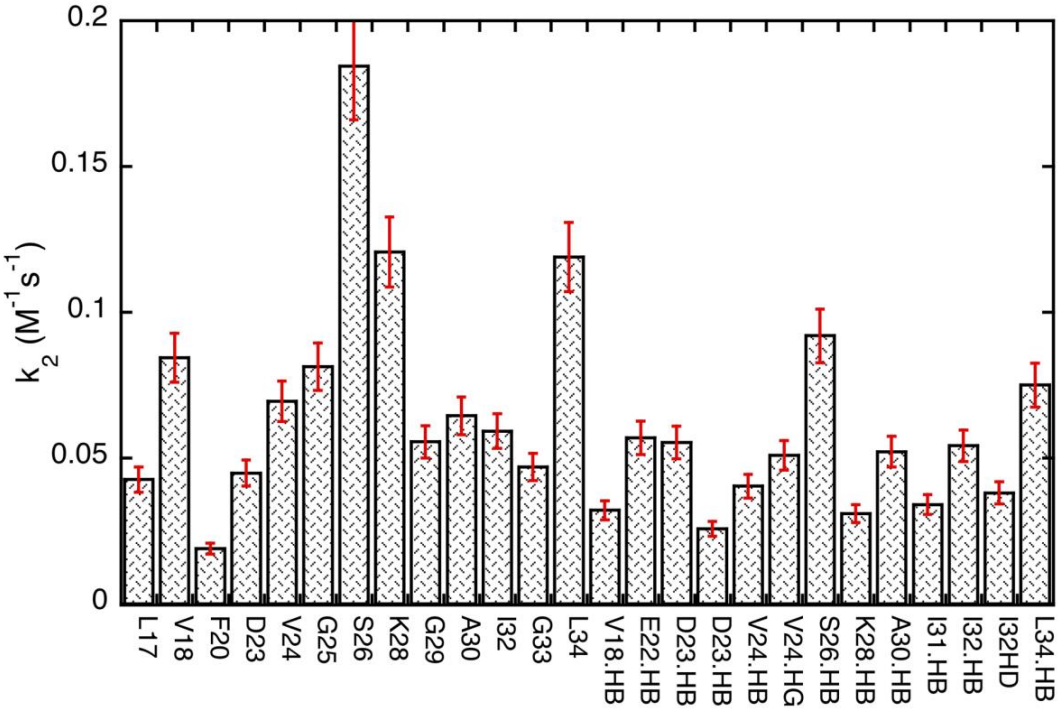

Figure 2.20 Rates for Cys-Aβ16-34 in the presence of TCEP. Figure shows the results of a single experiment; error bars are standard deviations on the parameter, k_2 (second-order rate constant) obtained from nonlinear least squares fit of the data to Equation 7.

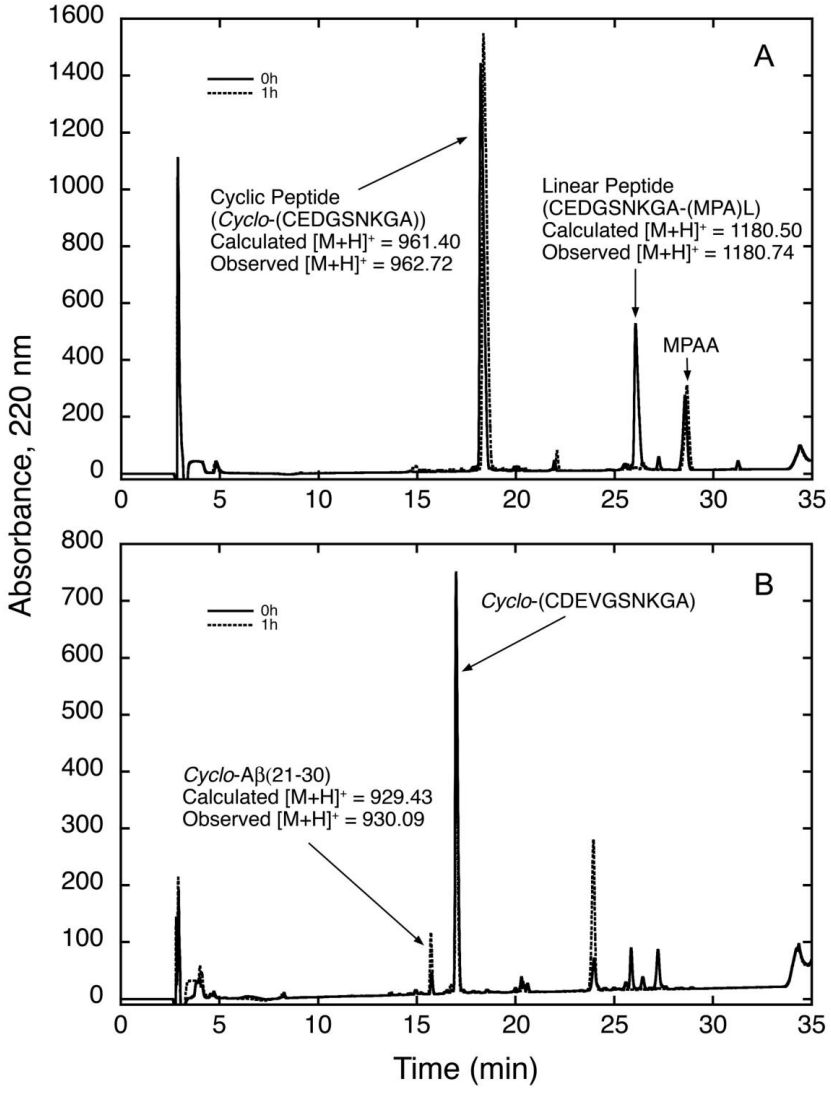

Figure 2.21 Cyclization by native chemical ligation, followed by desulfurization using Raney nickel. (A) Cyclization of (H)-CEDVGSKNGA-(MPA)-L-(OH), where MPA = mercaptopropionic acid, by native chemical ligation. Chromatography, using C18 column as described in Methods, was a gradient over 30 minutes from 100% A to 70% A: 30% B, where A = water:TFA (100:0.1, v:v) and B = acetonitrile:TFA (100:0.1, v:v). Chromatography is at room temperature, and effluent absorbance is monitored at 220 nm. Starting material elutes at 26.06 minutes; calculated [M+H]+ = 1180.50, observed [M+H]+ = 1180.74. The product, cyclo-(CEDVGSNKGA), elutes at 18.34 minutes; calculated [M+H]+ = 961.40, observed [M+H]+ = 962.72 the reaction is very efficient and is nearly complete at the “t = 0h”, i.e., chromatography of the starting material. (B) Desulfurization of the product of the above reaction using Raney nickel. The product, Cyclo-Aβ21-30; is the growing peak at 15.75 minute; calculated [M+H]+ = 929.43, observed [M+H]+ = 930.09.

Table 2.1: Peptides Synthesized for These Studies

$A\beta_{21\text{-}30}$	NH2-AEDVGSNKGA^{30}-COOH
Cyclo-$A\beta_{21\text{-}30}$	(–AEDVGSNKGA^{30}–)
$A\beta_{16\text{-}34}$	NH2-KLVFF^{20}AEDVGSNKGA^{30}IIGL-COOH
Cys-$A\beta_{16\text{-}34}$	NH2-CKLVFF^{20}AEDVGSNKGA^{30}-IIGL-COOH
$A\beta_{13\text{-}38}$	NH2-HHQKLVFF^{20} AEDVGSNKGA^{30}IIGLMVGG-COOH

Table 2.2: ^{13}C and ^{15}N NMR chemical shift values (ppm) for Aβ16-34, referenced to DSS

Residue	NH	Cα	Cβ	Cβ	Cγ	Cδ	Cδ
K16							
L17		61.83	40.25	40.18	32.54	20.66	21.2
V18	120.82	60.94			23.41		
F19	125	57.22	38.37				
F20	123.47	57.27	38.52				
A21	126.44	56.6	19.3				
E22	120.01	56.51	30.26	30.32	36.31		
D23	121.92	54.11	41.03	40.63			
V24	122.81	62.73	32.32		20.21		
G25	111.92	45.29					
S26	115.67	58.39	63.64				
N27	120.6	53.1	41.18	38.46			
K28	121.85	52.3	32.52		27.14	28.97	
G29	109.82	44.99					
A30	123.7	55.11	23.79				
I31	121.11	55.33	33.45		27.41	12.63	
I32	126.74	60.96	38.44			24.94	25.31
G33	114.11	45.02					
L34	127.66	52.28	40.07		43.27	24.54	

Table 2.3: ^{1}H NMR chemical shift values (ppm) for Aβ16-34, referenced to DSS

Residue	NH	Hα	Hβ	Hβ	Hγ	Hγ	Hγ	Hδ	Hδ
K16									
L17									
V18	8.25	3.97	1.78		0.69				
F19	8.37	4.51	2.92	2.85					
F20	8.29	4.49	3	2.86					
A21	8.31	4.14	1.29						
E22	8.42	4.12	1.96	1.84	2.2				
D23	8.48	4.57	2.67	2.56					
V24	8.22	4.06	2.12		0.89				
G25	8.6	3.92							
S26	8.2	4.36	3.81						
N27	8.53	4.66	2.8	2.73					
K28	8.41	4.2	1.83	1.7	1.37			1.59	
G29	8.47	3.85							
A30	8.09	4.23	1.29						
I31	8.26	4.08	1.83		0.81	1.12	1.43	0.69	
I32	8.37	4.1	1.8		0.85	1.15	1.43	0.78	
G33	8.55	3.87	1.52					0.8	0.84
L34	7.86	4.15							

Table 2.4: ^{13}C and ^{15}N NMR chemical shift values (ppm) for Cys-Aβ16-34, referenced to DSS

Residue	N	Cα	Cβ	Cβ	Cγ	Cγ	Cδ
K16	124.85	56.41	27.23				
L17	122.14	61.85	40.25	40.18	32.94		20.64
V18	120.82	60.96			23.43		
F19	126.74	57.3	38.5				
F20	123.33	57.26	38.53				
A21	126.46	56.63	19.32				
E22	120.18	56.51	30.34	30.32	36.34		
D23	122	54.07	41.09	40.74			
V24	120.95	62.75	32.322		20.24		
G25	111.97	45.34					
S26	115.67	58.49	63.66				
N27	120.77	53.22	38.48	41.09			
K28	121.96	52.33	32.77		24.79		28.99
G29	109.82	45.05					
A30	123.7	55.14	24.79				
I31	121.11	57.5	33.04		27.36		12.63
I32	124.83	60.96	38.5		21.11	25.29	24.76
G33	114.11	45.11					
L34	127.66	52.3	40.1		24.89	43.27	17.49

Table 2.5: ^{1}H NMR chemical shift values (ppm) for Cys-Aβ16-34, referenced to DSS

Residue	NH	Hα	Hβ	Hβ	Hγ	Hγ	Hγ	Hδ	Hδ
K16	8.52								
L17	8.08								
V18	8.21	3.97	1.78		0.69				
F19	8.36	4.51	2.92	2.85					
F20	8.28	4.49	3	2.86					
A21	8.3	4.14	1.29						
E22	8.41	4.12	1.96	1.84	2.2				
D23	8.47	4.57	2.67	2.56					
V24	8.22	4.06	2.12		0.89				
G25	8.6	3.92							
S26	8.2	4.36	3.81						
N27	8.54	4.66	2.8	2.73					
K28	8.4	4.2	1.83	1.7	1.37			1.59	
G29	8.47	3.85							
A30	8.08	4.23	1.29						
I31	8.25	4.08	1.83		0.81	1.12	1.43	0.69	
I32	8.34	4.1	1.8		0.85	1.15	1.43	0.78	
G33	8.54	3.87	1.52					0.8	0.84
L34	7.86	4.15							

Table 2.6: ^{13}C and ^{15}N NMR chemical shift values (ppm) for Aβ 21-30, referenced to DSS

Residue	N	Cα	Cβ	Cβ	Cγ	Cγ	Cϵ
A21		51.91	19.36				
E22	119.75	55.85	29.17	29.17	33.08		
D23	121.4		38.74	38.76			
V24	120.51	62.58	32.71		21.11	20.25	
G25	112.23	45.41					
S26	115.52	58.42	63.93	63.94			
N27	120.85	62.17					
K28	121.74	53.28	32.81		24.61		42.25
G29	110.13	45.23					
A30	126.35	52.57	19.49				

Table 2.7: ^{1}H NMR chemical shift values (ppm) for Aβ 21-30, referenced to DSS

Residue	NH	Hα	Hβ	Hβ	Hγ	Hγ
E22	8.64	4.41	2.47	2.43		
D23	8.61	4.74	2.9	2.79		
V24	8.16	4.16	2.15		0.97	0.93
G25	8.45	3.99				
S26	8.17	4.46	3.89			
N27	8.45	4.74	2.83	2.8		
K28	8.27	4.3	1.88	1.77	1.44	
G29	8.34	3.94				
A30	7.99	4.3	1.39			

Table 2.8: ^{13}C and ^{15}N NMR chemical shift values (ppm) for cyclo-Aβ21-30, referenced to DSS

Residue	N	Cα	Cα	Cβ	Cβ	Cγ	Cγ	Cδ	Cϵ
A21	122.13	53.21		19.3					
E22	117.68	56.03		30.79		30.79	36.38		
D23	125.11	54.78		40.27					
V24	125	60.62		32.21		20.64			
G25	112.65	45.41	45.22						
S26	116.15	58.87		63.63	63.99				
N27	120.11	50.76		38.6	38.57				
K28	120.41	56.6		32.77	32.8	24.82		29.11	42.2
G29	109.89	45.16	45.21						
A30	123.46	52.88		24.85					

Table 2.9: ^{1}H NMR chemical shift values (ppm) for cyclo-Aβ 21-30, referenced to DSS

Residue	NH	Hα	Hα	Hβ	Hβ	Hγ	Hγ	Hδ	Hϵ
A21	8.43	4.19		1.36					
E22	7.94	4.29		1.82		2.15	2.07		
D23	7.89	4.41		2.77					
V24	8.32	3.88		2.01		0.91			
G25	8.71	3.93							
S26	8.26	4.39		3.84					
N27	8.56	4.65		2.84	2.78				
K28	8.33	4.23		1.83	1.63	1.31		1.39	2.92
G29	8.41	3.99	3.79						
A30	8.09	4.22		1.37					

2.7 Solution of Differential Equation 5

$$\frac{dA(t)}{dt} = -k'[A(t)] - k_2[A(t)]^2$$

where A(t) = (V-V_{eq}), a function of t. This can be solved as a Bernoulli's equation. Adding k´[A(t)] to both sides:

$$\frac{dA(t)}{dt} + k'[A(t)] = -k_2[A(t)]^2$$

Dividing both sides by –$[A(t)]^2$:

$$\frac{-\frac{dA(t)}{dt}}{[A(t)]^2} - \frac{k'}{[A(t)]} = k_2$$

Let:

$$x(t) = \frac{1}{A(t)}$$

which yields:

$$\frac{dx(t)}{dt} = \frac{-\frac{dA(t)}{dt}}{[A(t)]^2}$$

$$\frac{dx(t)}{dt} - k'x(t) = k_2$$

Let:

$$y(t) = e^{\int -k'dt} = e^{-k't}$$

Multiply both sides by y(t):

$$e^{-k't}\frac{dy(t)}{dt} - (k'e^{-k't})y(t) = k_2e^{-k't}$$

Now apply the reverse rule:

$$q\frac{dp}{dt} + p\frac{dq}{dt} = \frac{d}{dt}(fg)$$

Thus,

$$\frac{d}{dt}(e^{-k't})y(t) = k_2e^{-k't}$$

Integrate with respect to t:

$$\int \frac{d}{dt}(e^{-k't})y(t)dt = \int k_2(e^{-k't})dt$$

$$(e^{-k't})y(t) = -\frac{k_2(e^{-k't})}{k'} + C'$$

Dividing both sides by $y(t) = (e^{-k't})$,

$$y(t) = -\frac{k_2}{k'} + C'e^{k't}$$

Solving for A(t):

$$A(t) = \frac{1}{x(t)} = \frac{k'}{-k_2 + C'e^{k't}}$$

At t=0, A=A_0(where A_0 = V_0-V_{eq} and V_0 = peak volume at t=0):

$$C' = \frac{k'}{A_0} + k_2$$

Substituting this expression for C′, rearranging, and substituting A = V – V_{eq} and A_0 = V_0 – V_{eq} yields Equation 7:

$$V = \frac{(V_0 - V_{eq}k')}{((V_0 - V_{eq})k_2 + k')e^{k't} - (V_0 - V_{eq}k_2)} + V_{eq}$$

CHAPTER 3

A VERSATILE METHOD FOR PRODUCING LABELED OR UNLABELED Aβ55, Aβ40, AND OTHER β-AMYLOID FAMILY PEPTIDES

3.1 Introduction

Expression and purification of Aβ peptides, including transmembrane peptide- containing fragments of the β-amyloid precursor protein (β-APP), represents a particular challenge. Such methods are needed for producing uniformly isotopically- labeled peptides, as well as unlabeled peptides for diverse other applications. Several methods already exist for producing these peptides, usually as fusion proteins with Glutathione-S- transferase or others [145–152], and in some cases, a HexaHis tag. [146,153,154] One group has expressed a peptide containing Aβ and the C-terminus of Aβ-APP, Aβ99, as a HexaHis fusion protein without cleaving the HexaHis tag. [155,156] Most of these methods, however, generally have one potential drawback: they involve a folded protein – either as a fusion partner for the Aβ peptides, and/or as an enzyme used to cleave the Aβ peptide from its fusion partner. This is problematical because of the strong tendency of Aβ peptides to aggregate, and their limited solubility, which is especially severe for Aβ peptides containing the transmembrane (TM) domain of β-APP. In general, purification of these peptides requires fairly harsh conditions, such as low pH for RPHPLC, and/or the inclusion of detergents and denaturants in chromatographic solvents. These harsh conditions inhibit or eliminate the binding of fusion partners, such as GST, to affinity columns that might otherwise be used for purifying these peptides. Detergents and denaturants, needed to solubilize TM peptides, also can inhibit or eliminate the activity of enzymes like thrombin or Factor Xa that are used to cleave TM-peptides from their fusion partners. Here we present a straightforward and versatile set of methods for producing Aβ, TM-Aβ, and related peptides under relative harsh

conditions (i.e., acidic or denaturing conditions, including the presence of detergents). In principle, these methods should also be applicable to other types of strongly aggregating peptides. We will describe, below, a DNA plasmid containing a HexaHis tag linked to DNA encoding Aβ40 or TM-Aβ (Aβ55), containing amino acids 1–55 of β-APP, i.e., full-length Aβ with the TM-domain of β-APP. The use of the HexaHis tag, rather than a folded protein fusion partner, allowed for purification under harsh and denaturing conditions. In earlier experiments, the fusion site was a Factor Xa cleavage site, which is still useful in the case of Aβ40. The use of this cleavage site, however, is not optimal for the case of Aβ55 or other TM-peptides, which have an even more severe tendency towards self-aggregation and precipitation than does Aβ40. Accordingly, we have substituted a cleavage site for the chemical reagent, BNPS- Skatole, which cleaves selectively after Tryptophan, an amino acid not present in either Aβ or the TM domain of β-APP. It is a non-abundant amino acid in proteins generally, and is uncommon within transmembrane domains (though it is more abundant in juxtamembranous portions of proteins[157–159]); thus, this method may be useful for those proteins lacking tryptophan in relevant positions. We will also describe conditions for maximizing the yields of the final peptide products using this reagent, and minimizing its side reactions.

3.2 Results

3.2.1 DNA construct of HexaHis-tagged Aβ40 and Aβ55

DNA constructs, containing the sequence of either Aβ40 or Aβ55, were produced to contain either a factor Xa cleavage site or a BNPS- skatole cleavage site (Figure 3.1a). Constructs containing a Factor Xa cleavage site are designated with -IEGR-in the name, e.g.,HexaHis- IEGR- Aβ55. Constructs containing a BNPS- Skatole cleavage site are designated with -W- in the name, e.g., HexaHis-W- Aβ55. Predicted amino acid sequences of these constructs are also shown in the figure (Figure 3.1b). The construct also included a stop codon (TAA62) and the sites for two restriction enzymes, BamH1 and Not

1, as shown in the Figure. The construct was codon-optimized for E. coli expression by GenScript (GenScript Corporation, Piscataway, NJ, USA; www.GenScript.com), and supplied cloned into the pET-28a vector using its BamHI and NotI sites.

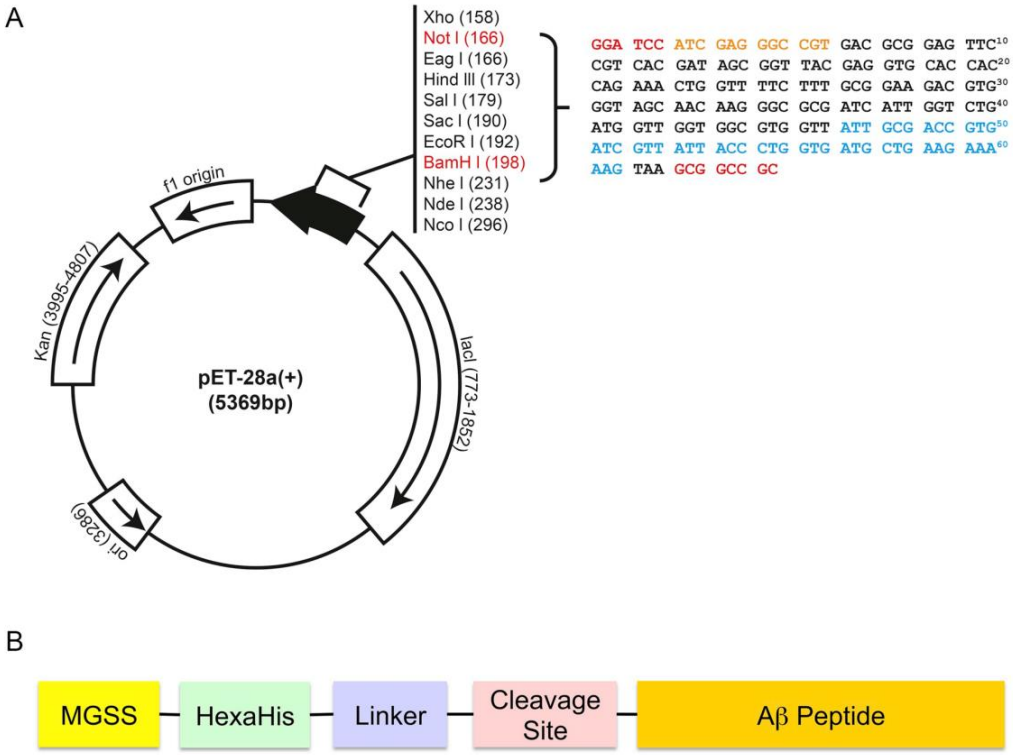

Figure 3.1 A: pET-28a (+) plasmid[160] with BamH1 (codon 1 and 2) and Not I (codon 63-end) cloning sites (red). The DNA constructs (Aβ40, black; additional residues in Aβ55, blue) are shown (right) and contain a factor Xa cleavage site (codon 3–6) highlighted in orange and a stop codon (TAA[62]). B: Amino Acid sequences of three expressed peptides. Each construct begins with Met (cleaved by E. coli Methionine aminopeptidase (MAP)[161] followed by a flexible linker (GSS) and a HexaHis sequence, a second flexible linker region (-SSGLVPRGSHMASMTGGQQMGRGS-), a cleavage site for either Factor Xa (-IEGR-) or BNPS-Skatole (-W-), and then the sequence of either Aβ40 ([1]DAEFRHDSGY [11]EVHHQKLVFF [21]AEDVGSNKGA [31]IIGLMVGGVV [40]) or Aβ55 (Aβ40-[41]IATVIVITLV[51]MLKKK55)

3.2.2 Growth of cells and peptide expression levels

Cell growth (Figure 3.2a) and peptide expression (Figure 3.2b) were robust. Yields of the expression fusion peptides, HexaHis-IEGR-Aβ40 and HexaHis-IEGR-Aβ55 were ∼ 8mg/L and 7–10 mg/mL of culture medium, respectively, when the cells were grown in M9 minimal medium. Yields of Aβ40 and Aβ55 after Factor Xa cleavage were ∼ 3–4 and 1–2 mg/L of culture medium, respectively, when cells were grown in M9 minimal medium. Similar yields were obtained for constructs containing the BNPS-Skatole cleavage site.

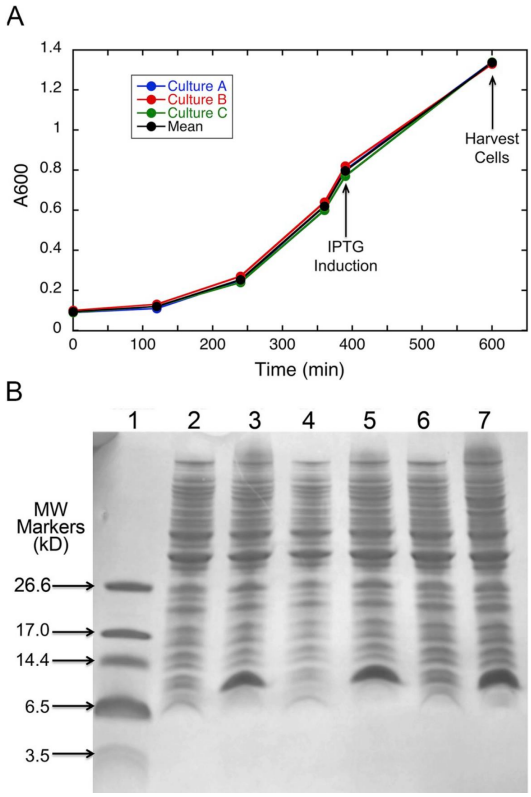

Figure 3.2 A: Growth curves of three samples of bacteria containing constructs for HexaHis-IEGR-Aβ55, grown in M9 minimal medium with ^{15}N–NH4Cl as the sole nitrogen source. Overnight cultures of the cells in LB yielded A600 = 0.93 ± 0.08 for these three cultures. Cells were washed, placed into M9 medium containing isotopic label, and grown in M9 as described in the text. Timing of induction with IPTG and harvesting is indicated in the figure. Mean of the three culture growth curves is also shown; standard deviations were calculated and plotted, but are smaller than data points. B: Expression of ^{15}NHexaHis- IEGR-Aβ55 in M9 medium. Lane 1=molecular weight markers, as shown. Lanes 2, 4, and 6: uninduced. Lanes 3, 5, and 7: induced using IPTG, as described.

3.2.3 Overall purification scheme

In all cases, little of the expressed protein was present in S1; most of it was in inclusion bodies, and therefore was present in pellet P1. Accordingly, several schemes were developed for purifying proteins from the inclusion bodies (Figure 3.3). As shown in the Flow Chart, these schemes consisted of the following elements (in some slightly different orders): 1) solubilization, using either Urea/Triton-X100 (for Aβ40 or Aβ55) or SDS (for Aβ55); 2) chromatographic purification, using a combination of Ni-NTA affinity chromatography, size exclusion chromatography (Superdex 200), and RP-HPLC; and 3) cleavage of the fusion proteins with either Factor Xa or BNPS-Skatole. For the following sections, see the purification table, with yields and estimated purity (Table 3.1).

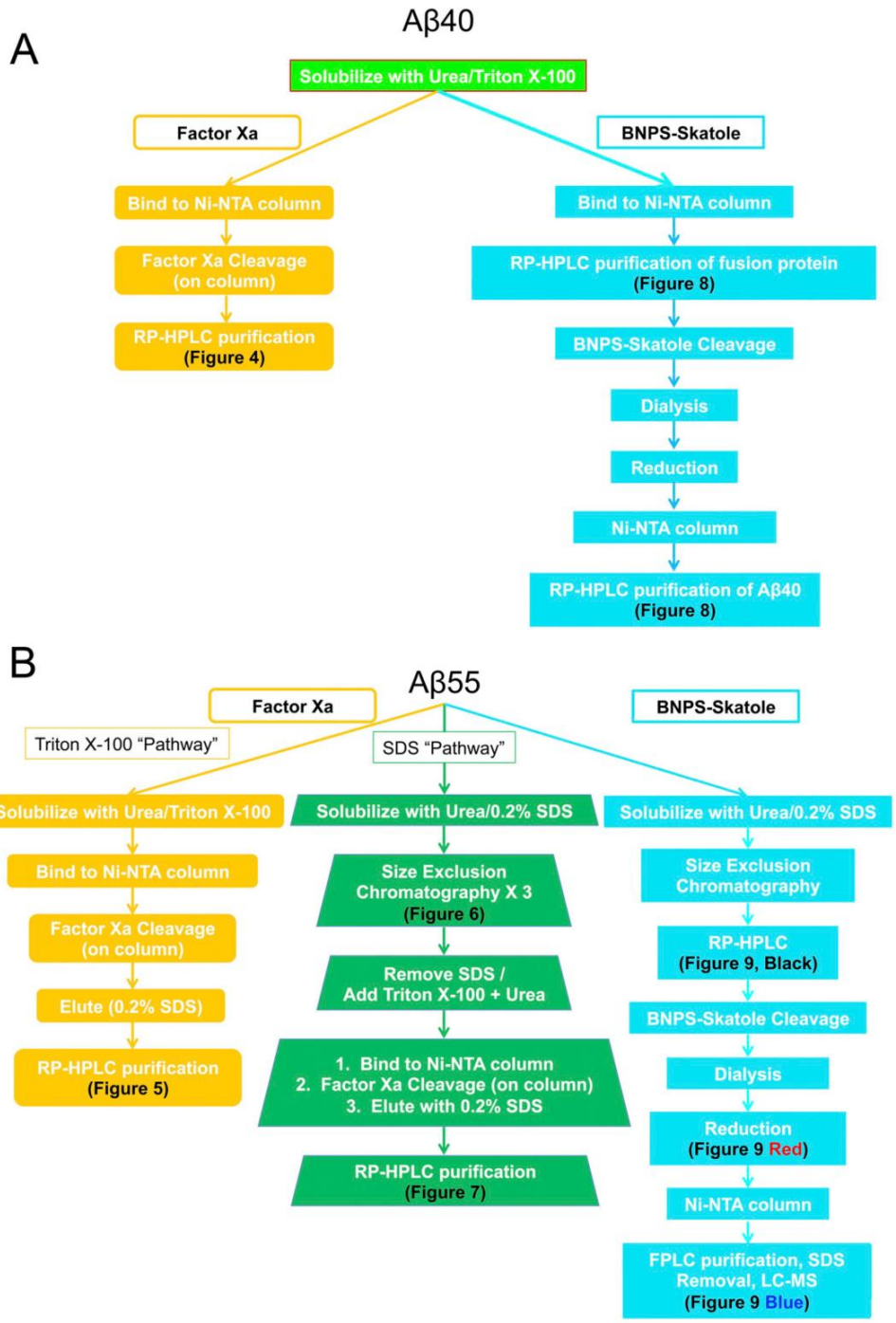

Figure 3.3 Flow Charts for purification of Aβ40 (A) and Aβ55 (B).

3.2.4 Purification of Aβ40

Two procedures were developed for purifying Aβ40: one including a cleavage of the fusion protein by Factor Xa (discussed here), and one including a cleavage by BNPS-Skatole (discussed below). Aβ40 pellets were effectively solubilized by 5.0M urea and 1% (w/ v) Triton X-100 (with 50mM Tris-HCl, 100mM NaCl, 10mM imidazole, pH 7.5). This solvent has the advantage that urea and Triton X-100 are easily removed by several methods. In addition, this solvent did not prevent binding of the fusion peptide to the column. After batch loading the peptide in this solvent onto the Ni-NTA column, the column was washed with 10 column volumes of 50mM Tris-HCl, 100mM NaCl, 1mM $CaCl_2$, pH 8.0. 40 unit/L of Factor Xa in the same buffer was added to the column and allowed to react with fusion protein overnight (∼16 h) at room temperature (∼20 °C). This led to essentially 100% cleavage of the fusion protein. The solution containing Factor Xa was eluted from the column, and the column was then eluted with 20 mL of the same buffer containing 500mM imidazole. This high concentration of imidazole was necessary to remove Aβ40 from the column because this protein is well known to bind divalent metal ions.[105,109,111–113,162–168] The effluent was then acidified using neat TFA (to pH ∼ 2–3) and then loaded onto the preparative RP-HPLC column in 5 mL batches and further purified as shown in Figure 3.4. Purified Aβ40 eluted from the column at ∼43 min (40% acetonitrile, v/v, for unlabeled Aβ40, m/ z = 1443.96 for +3 ion, MW = 4328.86, expected molecular weight=4329.9). A secondary cleavage site was also observed by mass spectrometry, between R5 and H6 (m/z = 1237.65 for +3 ion, MW = 3709.95, expected = 3711.21), amounting to ∼ 2–5% of the peptide; this secondary cleavage site has also been observed by others.[149] The truncated peptide was separated from Aβ40 by RP-HPLC; although not further characterized, it was likely the peak eluting at ∼38 min (37% acetonitrile, v/v).

Table 3.1: Yields of the dry peptides per liter of culture medium, determined in the process of the setup for this protocol

Peptide	Yield	Purity
His-IEGR-Aβ40	6–8 mg	$\geq$ 95% [a]
His-W-Aβ40	6–8 mg	$\geq$ 95% [a]
His-IEGR-Aβ55	7–10 mg	$\geq$ 95% [a]
His-W-Aβ55	7–10 mg	$\geq$ 95% [a]
Aβ40 (factor Xa)	3–4 mg	$\geq$ 95% [a]
Aβ40 (BNPS)	2–3 mg	$\geq$ 95% [a b]
Aβ55 (factor Xa)	1 mg	$\geq$ 95% [a]
Aβ55 (BNPS)	2 mg	$\geq$ 95% [a b]

[a] ≥ 95% purity by SDS-PAGE.

[b] ≥ 95% purity by SDS-PAGE; bromo-Tyr is≤1% by LC-MS; Met-oxide ≤ 1% by LC-MS.

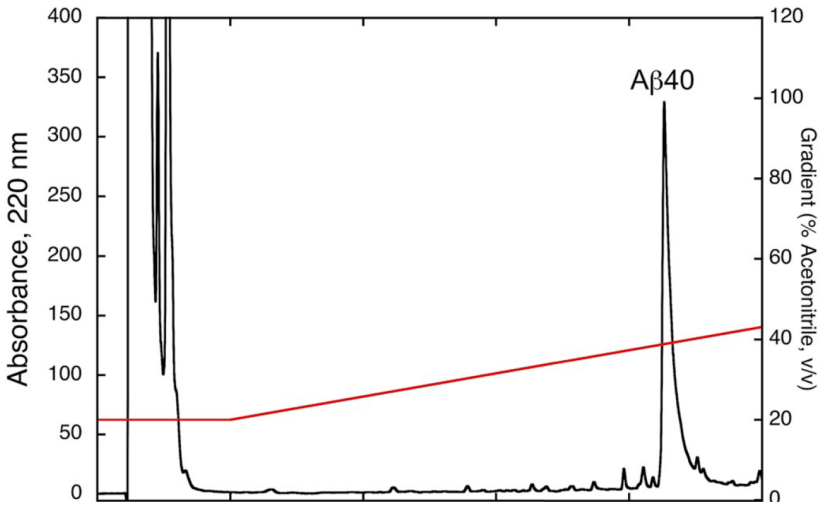

Figure 3.4 RP-HPLC puification of Aβ40 produced by Factor Xa cleavage of HexaHis-IEGR-Aβ40.

3.2.5 Purification of Aβ55

Purification of Aβ55 presents special challenges. In addition to the Aβ segment, which has a strong tendency towards self-aggregation, the Aβ55 peptide also contains a transmembrane domain, which has very poor water solubility. Accordingly, we developed two "pathways" for purifying this peptide in detergents, which we refer to as the Triton X- 100 Pathway, and the SDS Pathway. Although both "pathways" use both detergents, they differ in the points at which the detergents were added, and in the methods for removing detergents.

a. Triton X-100 Pathway: The pellet was washed with the following buffers to remove as much of the extraneous protein as possible: these washes with 50mM Tris-HCl, 150mM NaCl, 20mM β-mercaptoethanol, 1mM PMSF, pH 7.5, followed by three washes with the same buffer also containing 0.1% Triton X-100 (w/v) and 1M urea. These washes did not solubilize any of the Aβ55. The protein remaining in the pellet, including essentially all of the Aβ55, was solubilized in 50mM Tris-HCl, 150mM NaCl, 20mM β-mercaptoethanol, 1mM PMSF, pH 7.5 containing 1% (w/v) Triton X-100 and 5M urea. This lysate was applied in a single batch to a Ni-NTA column. The column was washed with 20 column volumes of 50mM Tris-HCl, 100mM NaCl, 1mM $CaCl_2$, pH 8.0 to equilibrate the column. The peptide was then cleaved using 40 units of Factor Xa in presence of 50mM Tris-HCl, 100mM NaCl, 1mM $CaCl_2$, pH 8.0 overnight at room temperature ($\sim$16 h at 20 °C). After the cleavage, the column was washed with 20 column volumes 50mM Tris, pH=8. Release of Aβ55 from the column required 0.2% (w/v) SDS, in two steps. (Attempts to release Aβ55 from the column using Triton X-100 and urea led to complications during RPHPLC because Triton X-100 and protein co-eluted as a single peak in several gradients.) The first elution was with $\sim$2 column volumes of 0.2% (w/v) SDS (with 50 mM Tris +100 mM NaCl, pH 8.0). The second elution was with 0.2% SDS and 1 M imidazole (with 50 mM Tris +100 mM NaCl, pH 8.0).

The protein then was further purified by RP-HPLC (Figure 3.5). Aβ55 eluted as a

doublet of peaks at ~63% acetonitrile in the gradient shown in the figure. Mass spectrometry showed that these peaks were Aβ55 and oxidized Aβ55, at Met35 (for Aβ55, m/ z = 1496.38 for +4 ion, MW = 5981.52, expected = 5982.06; for oxidized Aβ55, m/z=1500.19, MW=6000.76, expected=5997.52). The combined yield of Aβ55 was ~50–60% of the total quantity of HexaHis-IEGR-Aβ55 applied to the column, indicating that the cleavage by Factor Xa was not quantitative.

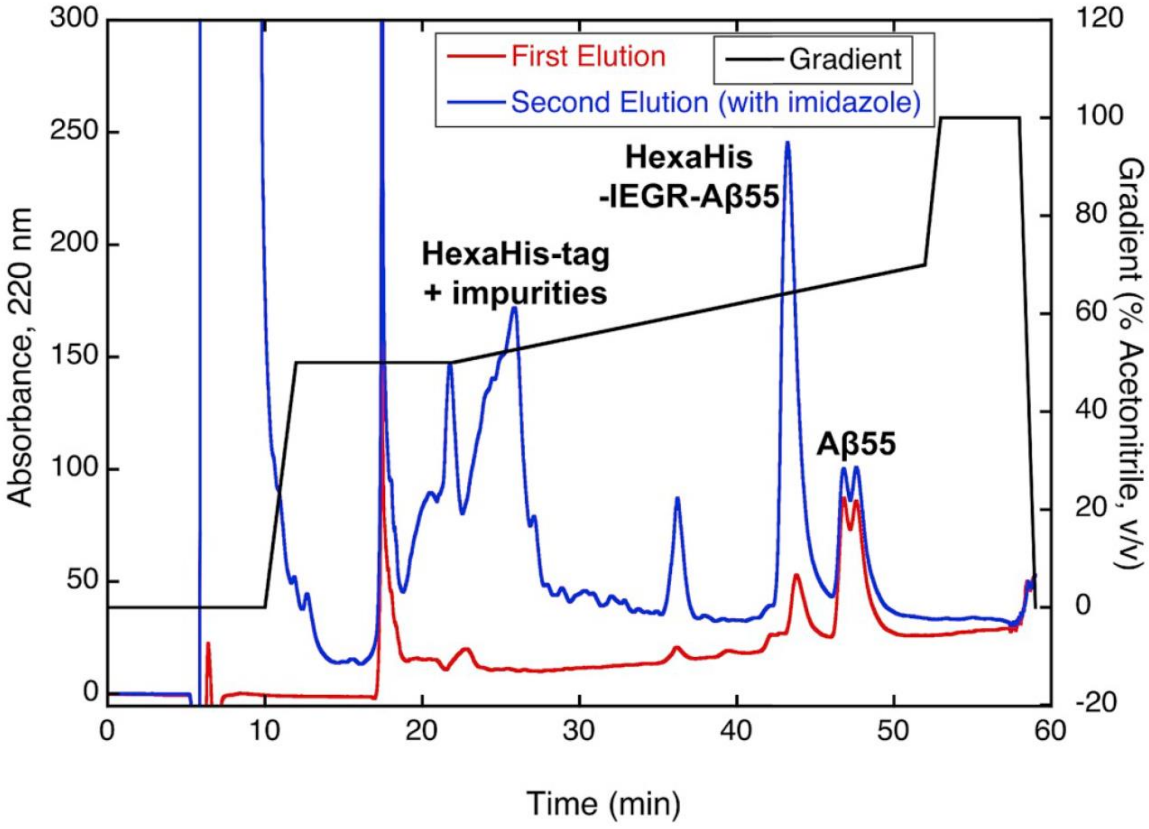

Figure 3.5 Aβ55 purified by the Triton X-100 "Pathway". HexaHis-IEGR-Aβ55 was solubilized using Triton X-100, and batch bound to a Ni-NTA column. After washing with buffer, the fusion protein was cleaved using Factor Xa, as described in the text. After the cleavage, Aβ55 was eluted from the Ni-NTA column in two steps: first, using a buffer with 0.2% (w/v) SDS, and second with the same buffer containing 0.2% (w/v) SDS and 1M imidazole. The eluted protein was further purified by RP-HPLC, as shown in the figure. Red=material from first elution, using buffer with 0.2% SDS; blue=material from second elution, using buffer with 0.2% SDS and 1M imidazole.

b. SDS Pathway: In this “pathway”, expressed proteins in pellet fraction P1 were solubilized using 0.2% (w/v) SDS instead of Triton X- 100 (buffer, including 5M urea, was otherwise the same as in the previous section). Protein was purified first using three rounds of Superdex 200 size exclusion chromatography, (Figure 3.6a). This successfully removes essentially all of the protein impurities (Figure 3.6b). Factor Xa cleavage required removing the SDS, which inactivates Factor Xa even at very low concentrations. SDS was removed either by dialysis or extraction using organic solvents. For dialysis[169], fractions containing Aβ55 were dialyzed twice against 50mM Tris, 150mM NaCl, 1% (w/v) Triton X-100, pH=8.0 at RT for 24 h. A final dialysis step was carried out at 4 °C using 50mM Tris, 150mM NaCl, 1% Triton X-100, 5M urea, pH 8.0), after which it was ready for batch binding to a Ni-NTA column. Alternatively, for organic solvent extraction, FPLC fractions containing Aβ55 were divided into 1 mL aliquots and lyophilized, and SDS was extracted by the method of Puchades et al.[170] After removal of SDS, protein was dissolved in 70/30 Acetonitrile/ water (0.1% TFA) lyophilized and re-dissolved into 50 mM Tris, 150 mM NaCl, 5 M urea, 1% Triton X-100, pH = 8 for batch binding to the Ni-NTA column. After washing the column with ∼20 column volumes of buffer (50 mM Tris +100 mM NaCl+1 mM CaCl2), the fusion protein was cleaved using Factor Xa, as described in the previous section. After the cleavage, Aβ55 was eluted from the Ni-NTA column in two steps: first, using a buffer with 0.2% (w/v) SDS, and second withthe same buffer containing 0.2% (w/v) SDS and 1M imidazole. The eluted protein was further purified by RP-HPLC, as shown in Figure 3.7a and b. As in the Triton X-100 “pathway”, the Aβ55 appeared as a doublet of peaks, the latter of which was oxidized at Met 35.

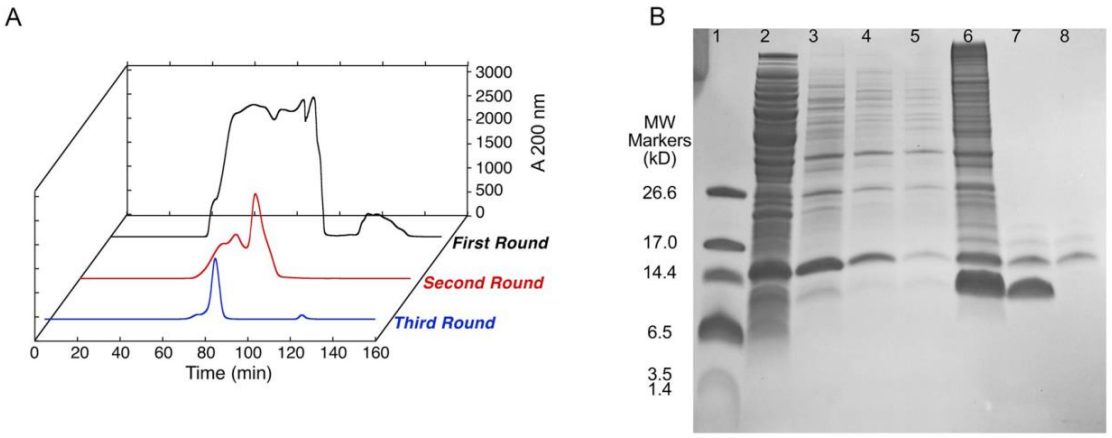

Figure 3.6 (A) Purification of HexaHis-IEGR-Aβ55 by three successive rounds of size exclusion chromatography (FPLC), using Superdex 200. (B) Tris-Tricine SDS-PAGE.Lanes are as follows: 1=Molecular weight markers. 2=Soluble fraction from lysed cells. 3–5=Pellets washed successively with lysis buffer containing 0.02% (w/v) SDS and 1M urea. 6. Pellets dissolved in lysis buffer containing 0.2% (w/v) SDS and 5M urea, and then applied to Superdex 200 SEC column. 7. Protein eluted from Superdex 200 column after three rounds of size exclusion FPLC. 8. Flow through from batch binding of FPLC purified HexaHis-IEGR-Aβ55.

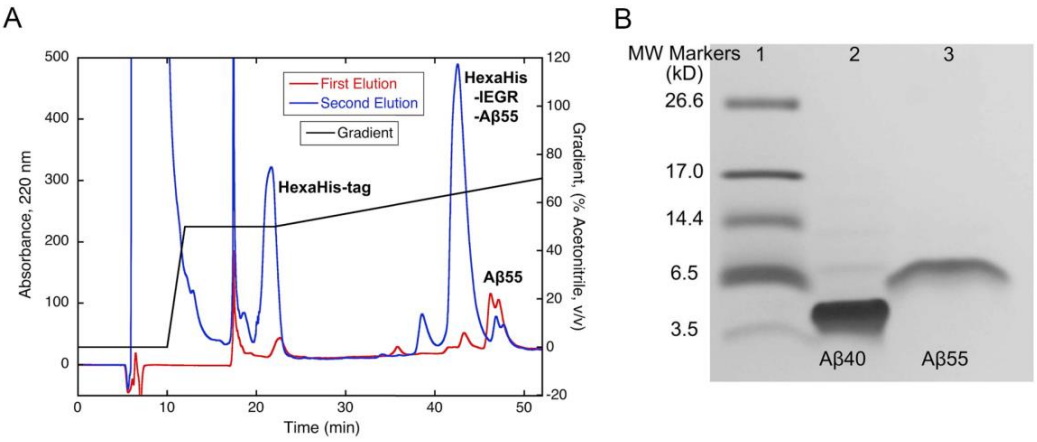

Figure 3.7 A: HexaHis-IEGR-Aβ55 was solubilized with lysis buffer containing 0.2% (w/v) SDS and 5M urea. It was then purified by three rounds of size exclusion chromatography (Figure 3.6a). SDS was removed by either dialysis or extraction as described in the text, and then batch bound to a Ni- NTA column. After washing with buffer (50 mM Tris +100 mM NaCl + 1 mM CaCl2), the fusion protein was cleaved using Factor Xa, as described in the text. After the cleavage, Aβ55 was eluted from the Ni-NTA column in two steps: first, using a buffer with 0.2% (w/v) SDS, and second with the same buffer containing 0.2% (w/v) SDS and 1M imidazole. The eluted protein was further purified by RP-HPLC, as shown in the figure. Red=material from first elution, using buffer with 0.2% SDS; blue=material from second elution, using buffer with 0.2% SDS and 1M imidazole. B: Tris-Tricine SDS-PAGE of purified Aβ40 and Aβ55, cleaved using Factor Xa. Lanes are as follows: 1=Molecular weight markers. 2=Aβ40 after cleavage and RP-HPLC purification. 3=Aβ55 after cleavage and RP-HPLC purification.

3.2.6 BNPS-skatole cleavage

The preceding procedures have an obvious shortcoming: the need for detergents and denaturants to solubilize strongly aggregating peptides, especially Aβ55, limits the usefulness of Factor Xa cleavage, since Factor Xa is inactivated by even very low concentrations of SDS. For example, even after exhaustive dialysis (against 50mM Tris, 150mM NaCl, 1% Triton X-100) to remove SDS, residual SDS inhibited Factor Xa and led to incomplete cleavage of the fusion protein. For this reason, we developed a fusion protein with a single Trp residue, which could be cleaved using BNPS-Skatole (2-(2′-nitrophenylsulfonyl)-3-

methyl-3- bromoindolenine). This reagent is effective even in the presence of SDS and Triton X-100, or other denaturants such as urea. It is an oxidizing and brominating agent that cleaves peptide bonds on the C-terminal side of unoxidized tryptophan (Trp) residues.[171–176] There are no Trp residues in either Aβ40 or Aβ55, nor in the remainder of the HexaHis fusion proteins other than the single Trp introduced in this construct. The main side reaction is bromination of Tyr residues. Only one Tyr residue is present in these constructs (Tyr 10 of Aβ40 or Aβ55), and this side reaction was greatly diminished by the addition of phenol as a scavenger.[174] Because of the large differences in the hydrophobicities of Aβ40 and Aβ55, somewhat different procedures were used to prepare samples for BNPS-Skatole cleavage. For Aβ40, the fusion protein was first purified by two sequential chromatography steps: 1) fusion protein was applied to a Ni-NTA column (in 50mM Tris-HCl, 100mM NaCl, 10mM imidazole, pH 7.5, with 5.0M urea and 1% (w/v) Triton X-100) and washed as above, which eliminated some of the impurities. The fusion protein was then eluted from the Ni-NTA column by 50mM Tris-HCl, 100mM NaCl, 500mM imidazole, pH 8.0.

The eluted protein was acidified using neat TFA to pH∼2–3 for RP-HPLC. The fusion protein was purified (Figure 3.8a) and then lyophilized. For Aβ55, the fusion protein, dissolved as lysate in 50mM Tris-HCl, 150mM NaCl, 20mM β-mercaptoethanol, 1mM PMSF, pH 7.5, was partially purified by one round of SEC chromatography (Superdex 200 column, 50mM Tris-HCl, 150mM NaCl, pH 8, and 0.2% (w/v) SDS). This protein was then acidified using neat TFA and further purified by RP-HPLC (Column: see general purification description; gradient (same as in Figure 3.5): 0–10 min, 0% B; 10–12 min, 0–50% B; 12–22 min, 50% B; 22–52 min, 50–70% B; 52–53 min, 70–100% B; 53–58 min, 100% B, 58–59 min, 100 - 0% B).

For BNPS-Skatole cleavage, lyophilized peptides were dissolved in 80% (v/v) acetic acid to a concentration of 1 mg/ml as estimated by A280. Liquefied phenol was added to give a final concentration of 2.5% (v/v). BNPS-Skatole at 1 mg/mL in glacial acetic

acid was added to give a BNPS-Skatole:peptide ratio of 50:1 (mol/mol). The acetic acid concentration was adjusted to 88% (v/v) by addition of water [40]. The mixture was shaken at 48 °C for 24 h in the dark. RP-HPLC of the peptide indicated that the cleavage reaction proceeded to ∼60–70% completion. Residual BNPS-Skatole was removed by dialysis against 88% acetic acid using 1 kD dialysis tubing (Spectra/Por, Spectrum labs), after which the peptide was lyophilized. This procedure yielded an oxidized product, which was reduced as described in the following section.

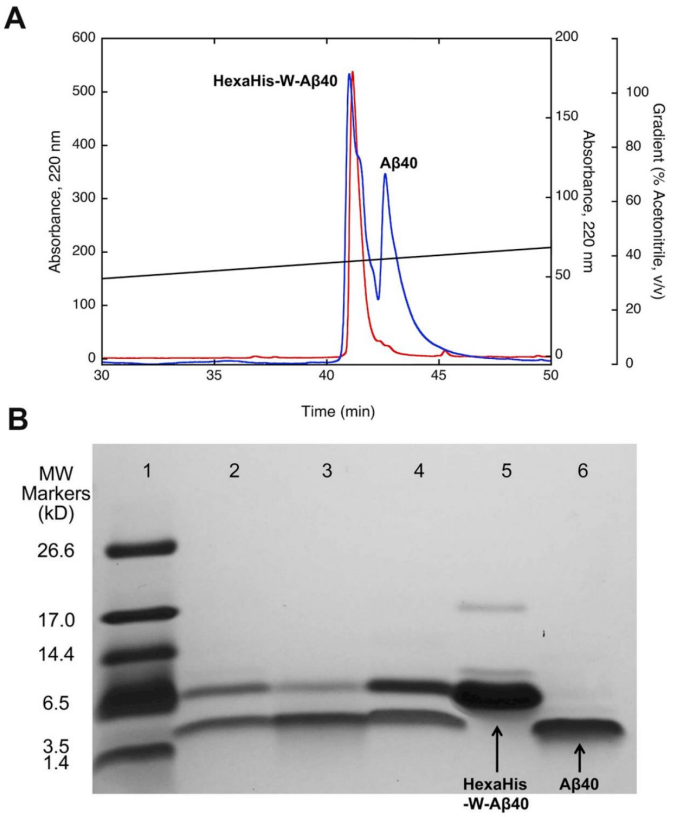

Figure 3.8 Peptide was cleaved using BNPS-Skatole, and then reduced as described in the text. A) Figure shows the RP-HPLC traces of the fusion protein HexaHis-W-Aβ40 (red), and the products of BNPS-Skatole cleavage after reduction (blue, see lane 2 of Figure 3.8b). It coelutes with Aβ40 produced by Factor Xa cleavage of HexaHis-IEGR-Aβ40. B) Tris-Tricine SDS-PAGE. Lanes are as follows: 1=Molecular weight markers. 2=HexaHis-W-Aβ40 after BNPS-Skatole cleavage and reduction. Because the high salt concentration interfered with the gel, 0.2% SDS, 50mM Tris, 150mM NaCl was added to the protein, which was then concentrated using Centricon filtration. The gel shows only the fusion protein and Aβ40; the HexaHis-tag was mostly lost in Centricon filtration. (However, because of the HexaHis-tag is quite similar in size to Aβ40, one would not see three bands even without the Centricon filtration step.) Yields of BNPS-Skatole cleavage typically were 60–70%. 3=HexaHis-W-Aβ40 after BNPS-Skatole cleavage and reduction. Protein was eluted from a Ni-NTA column by 50mM Tris, 150mM NaCl, 5M Urea, 50mM imidazole, pH 8.0, and prepared for SDS-PAGE as described for the previous sample. The eluant is enriched in Aβ40 (lower band) but still contains some HexaHis-W-Aβ40. 4=HexaHis-W-Aβ40 after BNPS-Skatole cleavage and reduction; after elution of protein from the Ni-NTA column by buffer with 50mM imidazole (lane 3), protein still on the column was then eluted using the same buffer but containing 500mM imidazole. 5=Uncleaved HexaHis-W-Aβ40, dissolved in neat HFIP, dried, and then redissolved in SDSsample buffer. 6=Purified Aβ40, after BNPS-Skatole cleavage and reduction, dissolved in neat HFIP, dried, and then redissolved in SDS-sample buffer.

3.2.7 Reduction of Aβ peptides

Aβ peptides, whether cleaved by Factor Xa or BNPS-Skatole were often partially or fully oxidized, and therefore appeared in RP-HPLC as a doublet (Factor Xa cleavage), or as a fully oxidized (BNPS-Skatole cleavage) peptide peak. Indeed, this is also the case for synthetic Aβ peptides, since Met35 is well known to be very prone to oxidation.[16,177] Accordingly, we routinely carried out the following reduction procedure[178], which reduces oxidized Met35 and Met51 (in Aβ55). Lyophilized peptide was dissolved into 2 mL of neat TFA also containing 60 equivalents each of dimethyl sulfide and ammonium iodide. The mixture was incubated for 2 h at 0 °C, after which the reaction was quenched by addition of 100 µL of water containing saturated ascorbic acid. Most of the TFA was removed by drying the mixture in a gentle air stream, until the volume was ∼200 µL.

3.2.8 Ni-NTA filtration & purification

After BNPS-Skatole cleavage and reduction, Aβ40 and Aβ55 were separated from uncleaved fusion protein and the cleaved HexaHis-tag using Ni-NTA chromatography. Again, because of the large difference in hydrophobicities, somewhat different solvent conditions were used for the two peptides. For Aβ40, after the reduction, the solvent was changed as follows. The peptide solution in TFA (with ammonium iodide and dimethylsulfide from the reduction) was diluted to ∼16 mL by adding 5M Urea, 50mM Tris, 150mM NaCl, 10mM imidazole, pH 8.0. This solution was concentrated by Centricon filtration (3 kDa, Amicon). This step was repeated three times (Figure 3.8b, lane 2). The pH of the solution was adjusted to 8.0 and the solution was run through a Ni-NTA spin column (∼2 mL slurry) via gravity flow. Remaining liquid was removed via centrifugation (3000×g). SDS-PAGE at this point indicated that all of the protein was bound to the column, including Aβ40. Aβ40 was eluted from the Ni-NTA column using a 5M Urea, 50mM Tris, 150mM NaCl and 50mM imidazole, pH 8 (Figure 3.8b, lane 3). For Aβ55, after the reduction, the solvent was changed as above, except that the solvent was 0.2% SDS, 50mM Tris, 150mM NaCl,

pH 8.0 (Figure 3.9b, lane 2). As above, the protein was applied to the Ni-NTA column, but SDS-PAGE indicated that while most or all of the HexaHistag and unreacted fusion protein remained bound to the column, Aβ55 passed through the column (Figure 3.9b, lane 3). This flow-through was then further purified by FPLC using Superdex 200 (0.2% SDS, 50mM Tris, 150mM NaCl, pH 8 buffer), as described above.

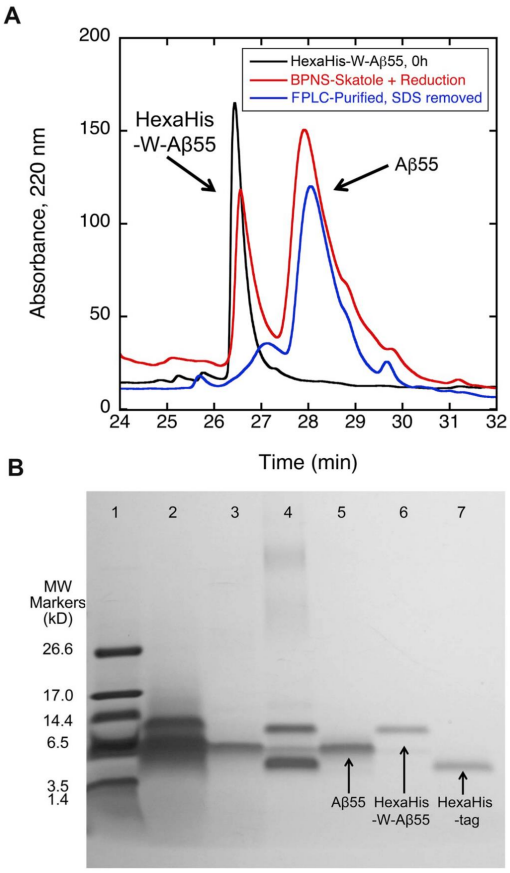

Figure 3.9 Peptide was cleaved using BNPS-Skatole, and then reduced as described in the text. A) Figure shows the RP-LC-MS traces of the fusion protein, and the product of BNPS-Skatole cleavage after reduction (see lane 2 of Figure 3.9b). Black: purified fusion protein before BNPS-Skatole cleavage. Red: fusion protein after 24 h of BNPS-Skatole cleavage followed by reduction. Two main peaks are present, eluting at ~26.4 min (HexaHis-W- Aβ55) and 28.2 min (Aβ55). Aβ55 was purified by FPLC as described in the text. SDS was removed by solvent extraction and analyzed by LCMS, the tracing of which is shown in the figure (Blue). It co-elutes with Aβ55 produced by Factor Xa cleavage of HexaHis-IEGR-Aβ55. B) SDS-Tricine-PAGE of BNPS-Skatole cleavage of HexaHis-W-Aβ55 and products of BNPS-Skatole cleavage. Lanes are as follows: 1=Molecular weight markers. 2=BNPS-Skatole cleavage of HexaHis-W-Aβ55. Protein was cleaved and reduced as described in text, after which the solvent was switched to 0.2% SDS, 50mM Tris, 150mM NaCl, pH 8.0, and concentrated by Centricon filtration. 3=Flow through of Ni-NTA column purification. Products of BNPS-Skatole cleavage and reduction were applied to a Ni-NTA column. The elutant has highly purified Aβ55. 4=Protein eluted from Ni-NTA column by 50mM Tris, 150mM NaCl, 500mM imidazole, pH 8.0. The main eluted proteins at this step are uncleaved fusion protein (HexaHis-W-Aβ55) and the cleaved HexaHis-tag. 5=Aβ55 after FPLC purification; this is the protein of which an HN-HSQC spectrum was obtained (Figure 3.10d). 6 and 7=Uncleaved HexaHis-W-Aβ55 and HexaHis-tag, respectively, separated from Aβ55 by Ni-NTA and from each other by FPLC.

3.2.9 NMR spectroscopy of purified, ^{15}N-labeled Aβ40 and Aβ55

As described in Methods, proteins were well expressed in E. coli using $^{15}N–NH_4Cl$ as the sole nitrogen source. $^{1}H–^{15}N$-HSQC spectra of Aβ40 and Aβ55, cleaved using Factor Xa or BNPS-Skatole are shown in Figure 3.10a–d. Spectra are essentially the same whether the protein was made using Factor Xa or BNPS-Skatole cleavage.

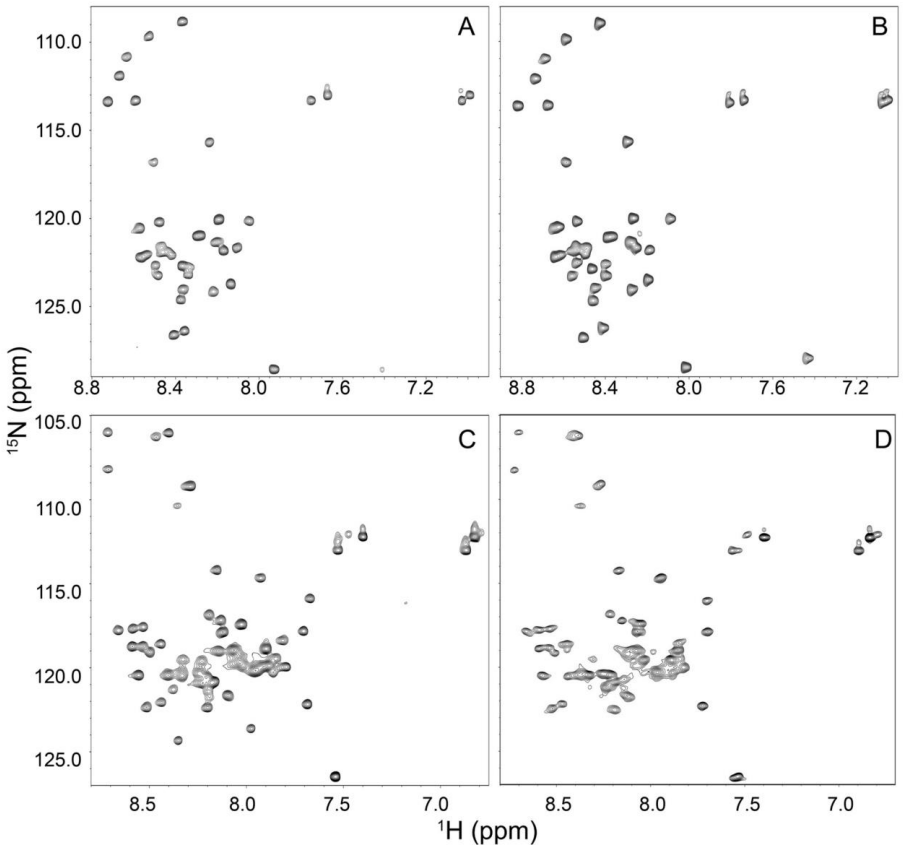

Figure 3.10 (A) Aβ40 at 30 μM, 5 °C, in 4mM HEPES, pH 8.0, cleaved with Factor Xa; (B) Aβ40 at 30 μM, 5 °C, in 4mM HEPES, pH 8.0, cleaved with BNPS-Skatole. (C) Aβ55 cleaved with Factor Xa; at 25 °C, in 50mM Tris-HCl, 150mM NaCl, pH 8.0, containing 0.2% (w/v) SDS. (D) Aβ55 cleaved with BNPSSkatole, at 25 °C, in 50mM Tris-HCl, 150mM NaCl, pH 8.0, containing 0.2% (w/v) SDS. Spectral differences between (A) and (B), and between (C) and (D) are minor (generally≤ 0.01 ppm), and may be accounted for as follows: Concentrations of Aβ40 were estimated by UV absorption at 274 nm and therefore are approximate; concentrations of Aβ55 were not determined. In addition, although the pairs of samples were dissolved in different batches of the same buffer, no pH indicator was included in the NMR sample; thus, minor differences in pH could account for the minor differences in chemical shifts.

3.3 Discussion

In this paper, we have described an expression system for Aβ peptides. Although we have focused on two of these, Aβ40 and Aβ55, it is in principle applicable to any Aβ peptide, and to other peptides with a strong tendency to self-associate and limited water solubility. It is important, in this discussion, to parse out two issues, which, though related, are separate: expression and purification. Considering each of these in turn, these constructs are simple, and expression of peptides using these constructs is highly efficient. In other words, contrary to some opinions, it is not necessary to have an efficiently folding fusion protein partner for Aβ in order to achieve high levels of expression. In addition, expression efficiency is high even in minimal media, perhaps, in part, because the demands of this short fusion protein on the cell's biosynthetic resources are less than those that would come with a larger fusion partner. The Aβ segment is linked to a HexaHis tag and a hydrophilic spacer region. This tends to increase the polarity and solubility of the fusion protein compared with Aβ peptides alone. As to purification, we have presented two purification schemes for each of these proteins, with an overall aim of steering away from the need for folded proteins – either a folded fusion partner for Aβ, or enzymes for cleaving Aβ from its fusion partner. In the case of Aβ40, this peptide is sufficiently soluble in the absence of detergents that Factor Xa cleavage is feasible. The use of a HexaHis tag allows for efficient loading of expressed fusion protein onto a Ni-NTA column, from which detergents or denaturants can be eliminated by simple washing procedures. In the absence of detergents or denaturants, cleavage of the fusion protein by Factor Xa is virtually quantitative. The purification of Aβ55 presents special challenges. In addition to the aggregation-prone Aβ segment, this peptide contains the additional residues of the full TM domain of β-APP.

These residues severely limit the solubility of the fusion protein: even the hydrophilic N-terminal segment is not sufficient to increase the solubility of the fusion protein very greatly; hence, the fusion peptide, though fully separated from Aβ55 in RP-HPLC, elutes

only slightly earlier than Aβ55 (e.g., 43 and 47 min in the chromatograph of Figure 3.5). Indeed, one is forced to use detergents and denaturants to purify Aβ55. The use of the HexaHis tag and the BNPS-Skatole cleavage site (a single Trp residue) eliminates the requirement for any folded proteins, such as enzymes, in the purification procedure. We have presented two different expression and purification systems for Aβ peptides, and there are advantages and disadvantages to each one. Thus, it is important to choose the procedure best suited to the particular peptide. For Aβ40, cleavage with Factor Xa is quantitative, and purification is relatively straightforward compared with Aβ55. On the other hand, since purification of Aβ55 absolutely requires detergents and strongly denaturing conditions, Factor Xa cleavage is suboptimal, since even low concentrations of residual detergent can severely impair the activity of this enzyme. Although we have not made a broad survey of other protease options, we chose this enzyme for its specificity compared, for example, to thrombin. It is likely, however, that other proteases are also sensitive to detergents. For this reason, we developed and optimized BNPS-Skatole cleavage of the fusion protein. Although yields of this cleavage reaction are sub-quantitative, yields are generally far above those obtained using Factor Xa (in the case of Aβ55), and it has the further advantage that it is insensitive to the presence of detergents and denaturants, and therefore can be used to produce highly aggregative and low solubility peptides such as Aβ55. Trp occurs infrequently in proteins in general and within transmembrane domains in particular[179–182], though it is considerably more abundant in regions flanking transmembrane segments.[154–157] Nevertheless, for peptides like Aβ55, and other transmembane peptides lacking Trp in relevant positions, this cleavage method remains a useful option.

3.4 Materials and Methods

In this section, we present the routine methods we used for expression and purification of peptides.[183] In Results, we will present non-routine methods for expression and purification.

3.4.1 Transformation & cryostocks (Aβ40 and Aβ55)

All peptides were expressed in the E. coli BL21 derivative, Rosetta2 (DE3) pLysS (Novagen). For transformations, we made competent cells in 100 µL aliquots with a Mix & Go kit supplied by Zymo research. These aliquots were stored at −80 °C until needed. Before each transformation, the competent cells were thawed for 30 min on ice, followed by addition of 6–10 ng DNA stock. The competent cells were carefully mixed by gentle flicking and then incubated on ice for 5–10 min. 250 µL of Miller LB-media (Fisher Scientific, pH adjusted to 7.2) was added, after which cells were incubated for 1 h at 37 °C, on a rotator bed (225 rpm). To allow better absorption of the liquid, the LB-Agar plates (previously stored at 4 °C) were pre-warmed at 37 °C. Agar plates contained 30 µg/mL of kanamycin and 34 µg/mL of chloramphenicol, corresponding to resistance factors in the pET-28a plasmid and Rosetta2 cells, respectively.[184] The cells were spread onto the agar plates and incubated over night at 37 °C. A single colony from these plates was picked and used for inoculation of 5 mL of Miller LB media (pH=7.2) containing the same antibiotics. The media was grown for 16 h at 37 °C, on a rotator bed (200 rpm). 0.5 mL of the culture was used to make cryostocks with 0.5 mL 50% glycerol. The rest was used for sequencing. DNA for sequencing was isolated using a QIAprep Spin Miniprep Kit supplied by Qiagen.

3.4.2 Expression of unlabeled proteins

For Aβ55, 100 mL LB broth with the above antibiotics was inoculated with a single colony from an LB-agar plate made from the cryostock described in the previous section, and grown at 27 °C, rotated at 200 rpm for 16 h (overnight). After the overnight incubation, A600 was ∼1.0; 600 mL of fresh LB broth was inoculated with these cells to yield A600=0.05. Cell growth was monitored thereafter by A600 measurements, and was continued until A600 reached 0.7–0.8 (2–3 h), after which expression was induced by addition of IPTG to 1 mM. Cells were then grown for an additional 3.5 h, after which they were har-

vested by centrifugation at 6000×g for 20 min at 4 °C (wet weight of the cells ∼1 g). The pellet was resuspended in LB and transferred to 50 mL tubes, centrifuged, decanted and stored at −20 °C until needed. Aβ40 is well expressed in minimal media containing either 14N or 15N as NH4Cl as the sole nitrogen source. Cells were prepared as described above, except for the following: the single colony of cells picked from the agar plates was grown in 2 mL of LB for 7–8 h, and this was placed into 50 mL of minimal media for growth over night at 37 °C. The following morning, these cells were placed into 1 L of M9 (minimal) media[185] containing 0.2x metal mix[186], and allowed to grow until A600 ∼ 0.8, at which time peptide expression was induced by adding IPTG to 1 mM. Cells were allowed to grow for an additional 3.5 h, after which the cells were harvested by centrifugation at 6000×g. Cell pellets were stored at −20°C until needed.

3.4.3 Introduction of isotopic labels (15N and/or 13C) into Aβ55

100 mL of the above overnight cell culture in LB broth was divided into two aliquots of 50 mL, and then pelleted by centrifugation at 4700×g, 30 min, 4 °C. To remove residual LB broth, the pellets were pelleted as above and then resuspended twice into 40 mL of M9 salts.[185] The pellets were re-combined and suspended into 40 mL of M9 media containing 15N– NH4Cl and/or 13C-glucose as the sole nitrogen and carbon sources and a 0.2x trace metal mix, respectively.[185,186] A sufficient quantity of these cells was inoculated into 600 mL of fresh M9 (containing the same isotopic labels) such that A600=0.05. Cell growth (Figure 3.2a) was continued until A600=0.7–0.8 (5–7 h). At that point, expression of the Aβ peptide was induced with IPTG to 1 mM, and incubation was continued for another 3.5 h. Cells were harvested as above (wet weight ∼3 g) by centrifugation at 6000×g for 20 min at 4°C. Cell pellets were stored at −20°C until needed.

3.4.4 Routine purification procedures

Typically, a pellet from 600 mL of culture media was re-suspended in 10 mL/(g cell pellet) of the following Lysis buffer (L): 50mM Tris, 150mM NaCl, 20mM β-ME, pH 7.5, also containing 1mM PMSF. 100 µL/(g cell pellet) of 100 mg/mL lysozyme was added, and the suspension was placed on ice, and agitated on a rocking shaker for 30 min. 100 µL/(g cell pellet) of 10 mg/mL DNaseI (Sigma-Aldrich) was added to the mixture, and the suspension was agitated for an additional 30 min. The cells were disrupted by sonication using a Branson model 250 sonifier (Branson Ultrasonics Corporation, St. Louis, MO) for 15 min (12 cycles, 10s sonication, 60 s pause), with the cells on ice. A soluble fraction (S1) was obtained by centrifugation (Sorvall RC-5C Plus) at 48,000×g for 30 min at 4 °C. As described below, most of the proteins of interest were expressed into inclusion bodies, and were present in the pellet fraction (P1).

3.4.5 Chromatography

Peptides were purified by FPLC and RP-HPLC. FPLC was performed using an Akta-Pure FPLC system (GE-Health), equipped with Unicorn 7.0 software. Size exclusion chromatography was performed with a Superdex 200 column. Eluent was 50mM Tris-HCl, pH 8.0, with 150mM NaCl, and for Aβ55, detergents such as 0.2% (w/v) SDS. Effluent was monitored by absorbance at 210–230 nm and 280 nm. Flow rate was typically 1.0 mL/min; temperature was room temperature (∼20 °C). RP-HPLC was performed using a HP 1050 preparative HPLC or Agilent 1100 analytical HPLC. Columns was C18: 300SB-C18 (Zorbax). RP-HPLC was performed with column temperature=55–60 °C; flow was 10 mL/min for preparative RPHPLC, and 1 mL/min for analytical RP-HPLC. Gradients were from water with 0.1% (v/v) TFA (henceforth called “A”) to acetonitrile with 0.08% TFA (henceforth called “B”); the gradient was adjusted to suit the particular peptide being purified. SDS-PAGE: Protein purifications were monitored using the Tris- Tricine system for SDS-PAGE of Schägger and von Jagow.[144,187]

3.4.6 Mass spectrometry

All mass spectrometry was done using an Agilent 1100 LC-MS system built of an Agilent 1100 HPLC with autosampler and an Agilent 1100 LC/MSD trap with an electrospray ionization (ESI) source. Data were recorded between 100 and 2200 m/z, in positive-ion mode using 4000 V capillary voltage at a 117 nA capillary current, 38 V Skimmer voltage and 3 V octopole voltage, 34 psi Nebulizer pressure and 9 L/min N2 dry gas flow at 300 °C. All data were analyzed using Agilent Chemstation (Rev. B.01.03 SR1 [204]) and Agilent DataAnalysis for LC/ MSD Trap (3.3 Build 146).

3.4.7 NMR spectrometry

NMR spectra were acquired on Bruker AVANCE III 500 MHz and AVANCE IIIHD 600 MHz NMR spectrometers equipped with a room temperature TXI probes. All spectra were acquired at a sample temperature of 5, 25, or 37°C, as indicated in the text. HN-HSQC spectra[188]were acquired using the standard sequencing in the Bruker sequence library.

CHAPTER 4

NANODROPLET OLIGOMERS (NANDOS) OF AMYLOID-β 40

4.1 Introduction

Aβ peptides self-associate into soluble oligomers and fibrils. While a great deal is known about the structure of fibrils[36,56,189–194], much less is known about the soluble oligomers and other pre-fibrillar species.[195,196] Soluble oligomers are widely considered to be the main neurotoxic species in AD and related disorders. Much of the evidence for this statement comes from measurements of the time course of cellular toxicity: the development of cytotoxicity occurs with a lag period, but precedes the formation of mature fibrils. A straightforward interpretation of such data is that monomers self-associate into oligomers of various sizes, and the oligomers confer most of the cytotoxicity.[196–198]

Many studies of Aβ include attempts at rigorous disaggregation of the peptide to a monomeric state, e.g., using organic solvents (e.g., dimethyl sulfoxide (DMSO) or hexafluoroisopropanol (HFIP)) or dilute acid or base.[199–203] While such treatments render peptide monomeric by some criteria (e.g., size exclusion chromatography), the actual aggregation state is not certain, however. A sparsely populated, small oligomer could be difficult to detect by conventional hydrodynamic methods, e.g., DLS or analytical ultracentrifugation. Thus, interrogating the aggregation status of these peptides could present a number of challenges.

In this paper, we examine this point. An inspection of the sequence of Aβ40 suggests that this peptide is amphiphilic – a point that has also been demonstrated experimentally.[37–39,204] Moreover, it could self-associate through either moiety, hydrophilic or lipophilic. The N-terminal region, which is mostly hydrophilic, is known to mediate the binding of metal ions, especially divalent metal ions, through His side-chains and other functional groups. The C-terminal region, on the other hand, is composed entirely of aliphatic

residues, constituting a spatially segregated lipophilic domain. A second patch of lipophilic residues occurs at amino acids 17-21. Either of these lipophilic (or hydrophobic) domains could mediate self-association through the hydrophobic effect.[34]

Here, we present evidence from Video-Rate Rate Atomic Force Microscopy (VRS-AFM) for the existence of flickering, transient small oligomers in fresh, rigorously disaggregated solutions of Aβ40, even at concentrations too low to sustain the formation of fibrils. As an operational designation, we call these species NanoDroplet Oligomers (NanDOs). In addition, we will present evidence from NMR spectroscopy about the nature of the associations of Aβ40 molecules within NanDOs. We will show that these associations are largely through clusters of hydrophobic amino acid side chains in the N- and C-terminal regions. We will also present data concerning the effects of adding metal ions, which cause a higher level of association, flocculation, involving the N-terminal region. We will present a model of the aggregation of Aβ involving the cooperation of the two disparate end of this amphiphilic peptide.

4.2 Results

4.2.1 Analysis of Aβ40 NanoDroplet oligomers with video-rate scanning AFM

As stated in Methods, preparation of Aβ40 included disaggregation steps using HFIP and DMSO at different stages. In agreement with other observers, this peptide was monomeric by size exclusion chromatography (Figure SI 4.8). Shortly after sample preparation, Aβ40 was deposited on mica in-solution and analyzed using Video-rate Scanning (VRS) AFM. In this method, the peptide always remains hydrated at a buffer-mica interface in a drop, rather than being irreversibly adsorbed at a mica-air interface. This was especially important for VRS-AFM, as it allows for visualization of dynamic changes in the sample. Upon injection of the sample, VRS AFM in-solution revealed a dense population

of particles consistent with monomeric Aβ40 (∼1 nm diameter for MW = 4219 and ρ = 1.34 g/cm^3) interspersed with larger particles of ∼ 4 nm. The latter have a diameter consistent with that of small oligomer. These oligomers rapidly diffused across the surface of the mica and underwent fusion into larger particles and separation into smaller ones. To confirm these as fusion events, particle heights and volumes were measured before and after association, for Aβ40 at 1 μM and 12 μM, using standard AFM analysis tools. We found that when two particles fused, the volumes increased additively, but there were only minor variations in height. This conservation of volume is expected for a fluid-like phase (Figure 4.1, Figure SI 4.9). In other words, this is a true fusion of droplets, not simply stacking of one droplet on top of another. Because of their ability to fuse, we term these small oligomers NanoDroplet Oligomers (NanDOs).

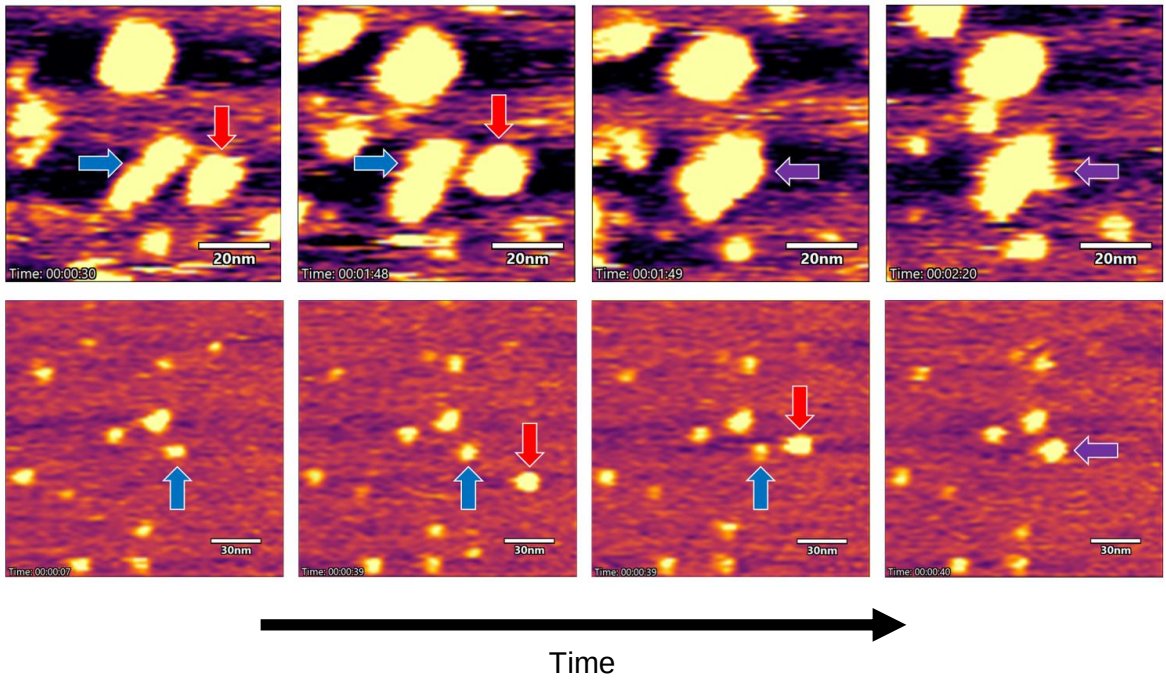

Figure 4.1 Frames from Video Rate Scanning-Atomic Force Microscopy of Aβ40, in solution mode. Top) 12 μM. Bottom) 1 μM. Particles can be observed to fuse and split in real time. Blue and red arrows mark particles; the purple arrow marks a fusion event. See also Table SI 4.1 and Figure SI 4.9.

Further strengthening the argument for the existence of small oligomers, we observed a small increase in particles sizes as a function of peptide concentration (Figure SI 4.10, showing a histogram of particle heights as measured by AFM in solutions of Aβ40 at two concentrations). Since the distribution clearly was not a normal distribution, the distributions of particle heights and volumes were analyzed by the Mann–Whitney U test, a nonparametric test of the null hypothesis that it is equally likely that a randomly selected value from one population is less than or greater than a randomly selected value from a second population – in this case the lower and higher concentrations of Aβ40.[205] One tailed Mann–Whitney U test yielded U values for the particle heights at 20 and 200 μM Aβ40 of 152256 and 134397 (for 321 and 893 particles), respectively, which gave a p-value of 0.049, with a z-value = -1.66, which is not in the 95% critical value accepted range, and therefore indicates that the null hypothesis is rejected, and the particle heights were larger in the 200 μM than the 20 μM Aβ40 sample. For particle volumes, similar results were obtained: one tailed Mann–Whitney U test yielded U values of 163612 and 124256 on the same particles for 20 and 200 μM Aβ40, which gave a p-value of 0.00011, with a z-value = 0.000108, again indicating that the null-hypothesis is rejected, and the particles were larger (by volume) in the 200 μM than the 20 μM. Although the volume result is statistically significant at a higher confidence level than the height result, the experimental measurement of heights by AFM is more reliable than calculation of volumes. The effect-size, therefore, should be considered to be small. As discussed below, we observe small changes in ^{1}H chemical shifts in ^{13}C-HSQC spectra with variations in peptide concentration, indicative of NanDO formation.

4.2.2 NMR spectra reveal NanDO formation

To probe the NanDOs at the atomic level, we acquired NMR spectra of Aβ40 at various concentrations. The lower end of this concentration range is well below the threshold for protofibrillar and fibrillar formation, and indeed, none was observed by ThT fluorescence or transmission electron microscopy. At the higher end of this range, it is possible that

fibrils would form eventually, but all AFM and NMR measurements were made at earlier time points, well before the ~1-2 day period needed to form protofibrils or fibrils.

AFM measurements indicated that oligomers were not only a flickering species, but also were a small portion of the population. These points presented a challenge for demonstrating atomic level changes by methods such as chemical shift perturbations, which would be expected from the formation of small oligomers. Using a wide variety of NMR spectrum types, we examined Aβ40 solutions at concentrations of 12-120 μM. It was important to ensure rigorous control of pH and DMSO concentration, as chemical shifts are very sensitive to these variables. pH was carefully matched in all of these experiment by using HEPES as an internal pH indicator. In other experiments, we monitored DMSO concentration by spiking d6-DMSO with 0.0025% protonated DMSO. We first made assignments using the following spectra (Chemical Shifts at 5 and 20° C in Tables SI 4.3-4.10): ^{15}N- and ^{13}C-HSQC, HNCO, HNcaCO, HNcoCACB, HNCACB, 2D homonuclear and 3D ^{15}N- and ^{13}C-edited TOCSY and NOESY.

At 5°C, the peptide formed solutions for which NMR measurements (^{15}N-HSQC, HNCO, other spectra) showed no changes in intensity or peak positions for a period up to one month (Figure SI 4.11). At 20°C, no changes in the spectra occurred for a period of up to 1.5 weeks, after which slow deterioration of the sample occurred due to oxidation and proteolysis. Thus, the solutions were temporally stable for long periods of time.

No CSPs were detected in either ^{15}N-HSQC or HNCO experiments. We carried out the latter 3D experiments because there was severe overlap of peaks in some areas of the ^{15}N-HSQC spectra. In all of these experiments, the buffer was HEPES, which also served as an internal pH indicator. Since the pH was near the inflection point of this buffer, it was a very sensitive indicator of pH changes. With each change of peptide concentration, the pH was readjusted so that the chemical shifts of the HEPES peaks remained constant to within ≤ 1 Hz (2×10^{-3} ppm of proton chemical shifts).

^{13}C-HSQC spectra showed obvious variations in many of the chemical shifts with changes in peptide concentration (Figure 4.2 a-d, Figure SI 4.12), though other peaks (Figure 4.2 e) showed no convincing movement with peptide concentration (Figure 4.2 e). These changes were especially prominent in some peaks associated with aromatic residues (Figure 2 b-e). (See also Figure SI 4.13, showing changes in chemical shifts observed in HNcoCACB spectra.)

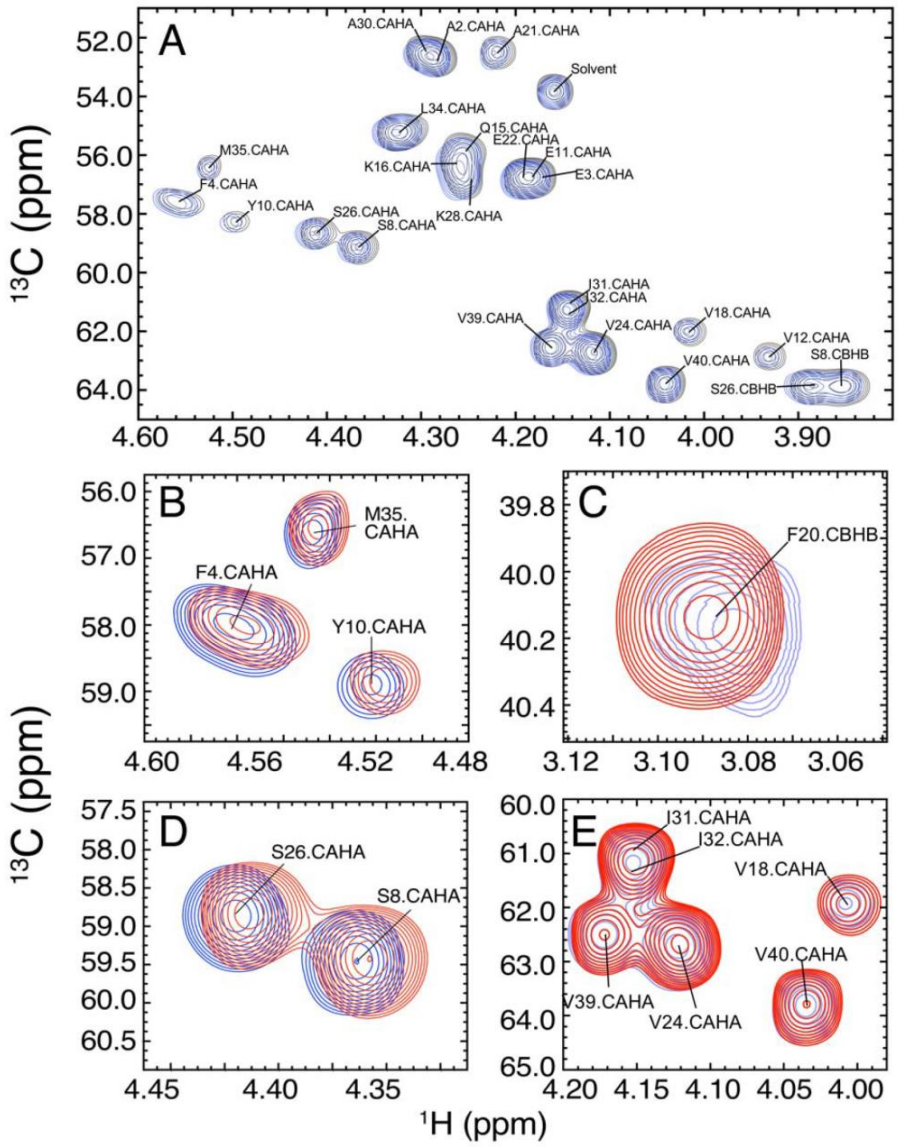

Figure 4.2 A) Portion of the ^{13}C-HSQC spectrum of Aβ40. (See also Figure SI 4.11). ^{13}C-HSQC were acquired at four different peptide concentrations (15, 30, 60 and 120 μM), of which two (15 and 120 μM in black and blue, respectively) are shown in the figure. b-e) Insets from the ^{13}C-HSQC spectra (shown in A) of 30 and 120 μM (blue and red, respectively). Pandels b-d show peaks with changes in chemical shifts; panel E shows five peaks with little or no discernible movement of peaks with the change in peptide concentration.

In addition, these spin system showed only changes of peak positions, without peak doubling. This indicates rapid exchange of peptide between pools of monomer and Nan-

DOs, i.e the observed chemical shifts represented a weighted average between the chemical shifts of Aβ40 monomers and Aβ40 in NanDOs. Furthermore, also consistent with AFM data, NanDOs represent only a small fraction of the total mass of peptide, which accounts for the small size of the observed CSPs. Nevertheless, the fact that some chemical shift perturbations could be observed with variations in peptide concentration strongly supports the occurrence of self-associated species in the solution.

Also consistent with AFM data, a number of additional NMR experiments supported the statement that NanDOs are mainly small oligomers representing a minority species in the solution. As expected from AFM and CSP measurements, diffusion coefficients (Figure 4.3) showed a small difference with changing peptide concentration. Figure 4.3 shows results for 20 HN-N peaks from the DOSY spectra of Aβ40 at 30 and 120 μM, selected as follows. Peaks were used only they had no overlap and were of sufficient signal strength to give a reliable peak volume; this was judged to be the case only if the non-linear least squares fit to the equation gave $R \geq 0.95$ and an error on the Diffusion coefficient parameter of ≤ 10% of its value. With these restrictions, the mean values for D were 1.45 ± 0.22 and 1.33 ± 0.08 $cm^2\ s^{-1}$ at 30 and 120 μM Aβ40, respectively. The data gave t-value = -2.44 and p-value = .009816, i.e., the difference between the means was significant at $p < .01$. Thus, at the lower peptide concentration, the diffusion coefficient was slightly greater than at the higher peptide concentration, consistent with an increase a higher fraction of peptides associated in NanDOs at higher concentrations.

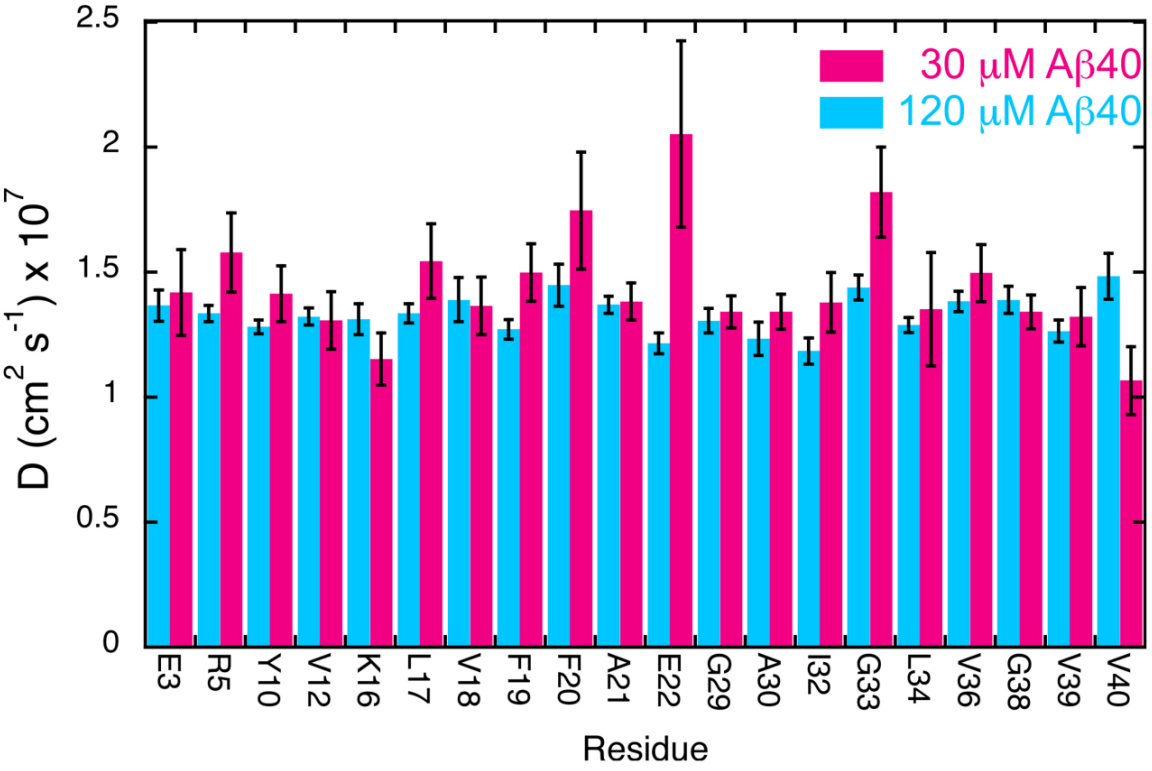

Figure 4.3 Diffusion coeffcients for Aβ40 at concentrations of 30 and 120 μM, calculated from Pulsed Field Gradient NMR experiments.

4.2.3 Paramagnetic Relaxation Enhancement (PRE) of NanDOs reveal association via the hydrophobic residues

Because of the low population and transient nature of NanDOs, we used Paramagnetic Relaxation Enhancement (PRE)[71,206] with two MTSL-labeled peptides: Y10C- and L34C-MTSL-Aβ40. Each of these peptides contained a single Cys residue to which the MTSL probe had been attached previously. The two peptides, Y10C- and L34C-MTSL-Aβ40, represent a point mutation in the N- and C- terminal regions of the peptide, respectively. Preliminary studies indicated that these peptides aggregated with similar kinetics as wild-type Aβ40. NMR spectra, including ^{1}H,^{1}1H-TOCSY and NOESY, and ^{15}N-HSQC (natural abundance), showed weak signal, as expected, but upon reduction of MTSL to

its diamagnetic form by incubating the peptide with ascorbate, signal was recovered and was quite similar to the spectra of wild-type Aβ40. For PRE experiments, ^{15}N-labeled Aβ40 was mixed MTSL-labeled, ^{14}N-labeled Aβ40 in neat DMSO. In most experiments, the ratio of ^{15}N-Aβ40 : ^{14}N-MTSL-Aβ40 was 1:1 (mol:mol). ^{15}N-HSQC experiments were then performed to measure signal intensity of the various peaks (as peak volumes). Peak volumes were compared to solutions of ^{15}N-Aβ40 without the MTSL probe. This procedure allowed us to detect changes in signal intensity at a residue-specific level.

In experiments using ^{14}N-L34C-MTSL-Aβ40, there was a continuous gradient of decreasing signal intensity in a stretch of amino acids from N- to C-terminus (Figure 4.4). Because of the amphiphilic nature of Aβ40, position in the amino acid sequence correlates with hydrophobicity. Thus, a similar correlation was also found between signal intensity and amino acid hydrophobicity (Figure SI 4.14, Table SI 4.11). These data suggest that formation of NanDOs is associated with intermolecular contacts between hydrophobic portions of Aβ40. In contrast to the findings with Y10C- and L34C-MTSL-Aβ40, the Y10C-MTSL Aβ40 peptide showed no such correlations (Figure 4.4 Bottom); if anything, signal increased slightly from N- to C-terminus. The experiments with Y10C-MTSL-Aβ40 further support the idea that the PRE effect observed with L34C- Aβ40 was a result of intermolecular contacts between hydrophobic portions of Aβ40.

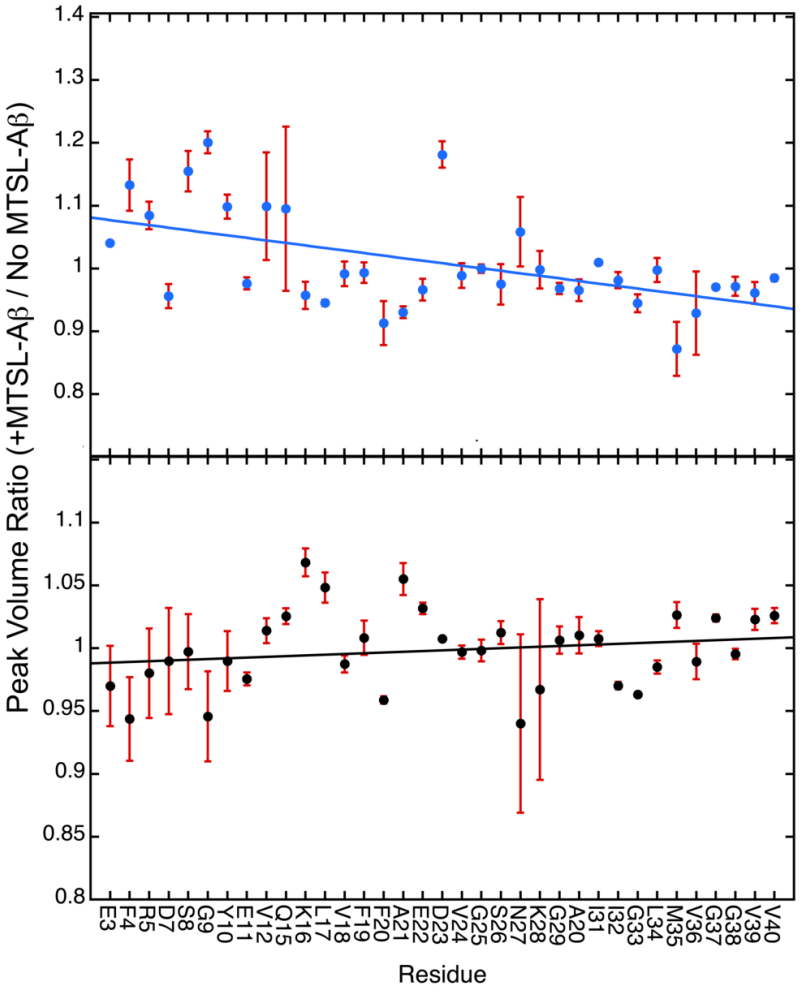

Figure 4.4 Paramagnetic Relaxation Enhancement of 100 μM ^{15}N-Aβ40 mixed with 100 μM ^{14}N-L34C-MTSL- Aβ40 (Top) or ^{14}N-Y34C-MTSL-Aβ40 (Bottom). Points represent Means ± SD for 3 separate experiments (i.e., three replicate samples). Line represents linear least squares fit of the data points. Peak volume is compared with a standard solution of ^{15}N-Aβ40 at the same concentration but not mixed with any other peptide. In (Top), there is a continuous decrease of signal intensity of amino acids from N- to C-terminus. No such decrease is observed in (Bottom).

4.2.4 The addition of Zn^{2+} to flocculate through its N-terminal region

To probe a possible role of N-terminal region in the aggregation of NanDOs, we performed experiments in which Zn^{2+} was added to the solution. Zn^{2+} and other divalent metal ions (including Cu^{2+} and Fe^{2+}) are well known to accelerate aggregation of Aβ pep-

tides.[41,105,162,163,207] Neuritic plaques of Alzheimer's disease and amyloid deposits in mouse models are enriched in these metal ions.[40] The metal binding site in Aβ40 has been localized to the N-terminal region, especially the His residues. In our experiments, we used a low concentration of Aβ40, and added Zn^{2+} into samples at a sub-stoichiometric quantities (1.5:1 = Aβ40:Zn^{2+}, mol:mol), so that there would be as little precipitation as possible. The samples were then analyzed using in-solution AFM and NMR.

AFM showed that addition of Zn^{2+} markedly increased the number and average sizes of the oligomers (Figure 4.5). As in previous experiments, AFM scans were used to analyze interactions between oligomers on the mica surface. This analysis suggests that unlike NanDO fusion, addition of Zn^{2+} caused peptide to form coarse precipitates, i.e., it causes flocculation of the peptide.

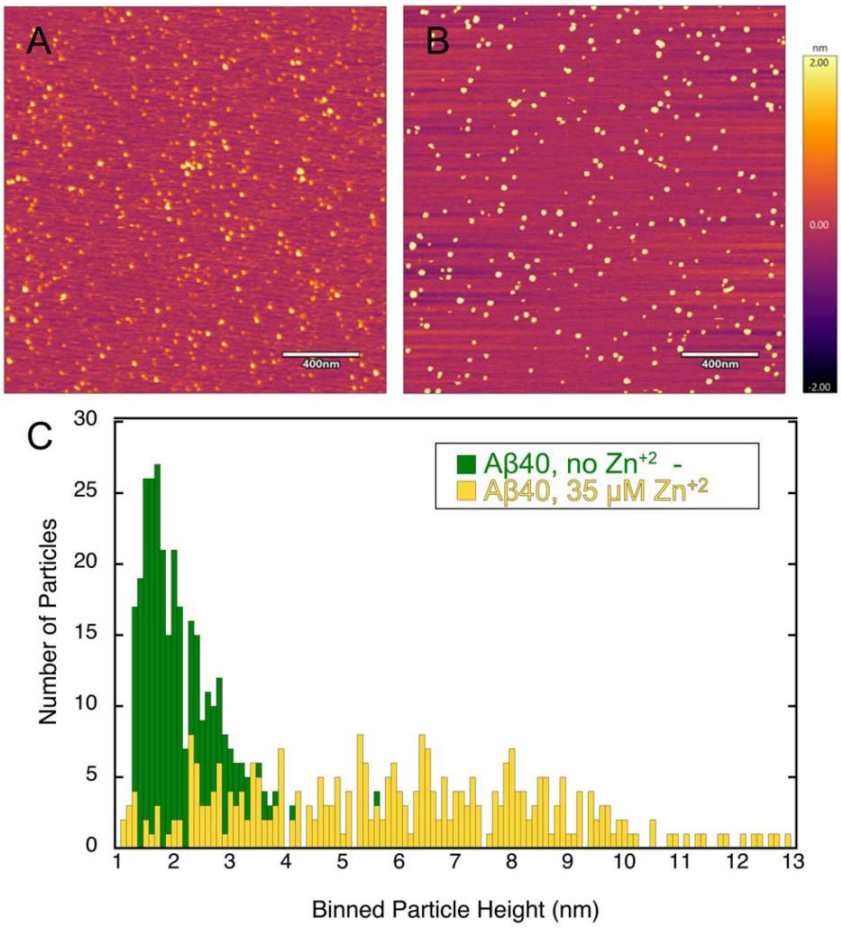

Figure 4.5 In solution AFM of μM Aβ40 with and without addition of Zn^{2+}. A and B) A field of the AFM containing 60 μM Aβ40, with 0 (A) or 35 μM added Zn^{2+}. C) Histogram of particle sizes in A) and B) showing that addition of Zn^{2+} markedly increases the number and average sizes of the soluble oligomers.

NMR showed that addition of Zn^{2+} led to a substantial loss of signal intensity, observed in ^{1}H-1D experiments, ^{1}H,^{15}N-HSQC and HNCO spectra (Figure 4.6 Top). A small portion of the signal loss was global, and due to precipitation of the peptide. Most of the signal loss, however, occurred in peptide that was still in the form of small, soluble oligomers, i.e., in species small enough to be observed by NMR. More importantly, the signal loss was regional, predominantly involving the N-terminal portion of the peptide. Furthermore, this loss of signal could be reversed by the addition of EDTA (Figure 4.6 Top).

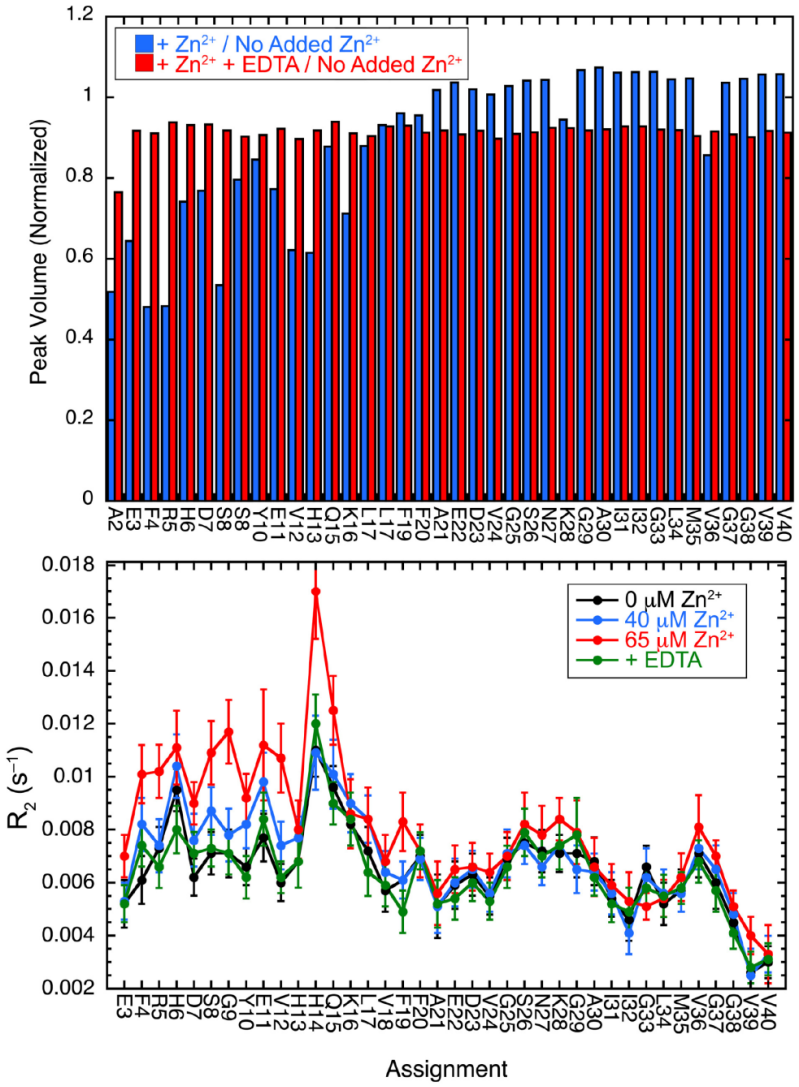

Figure 4.6 NMR effects of adding Zn^{2+} to solutions of Aβ40. Top) Selective loss of signal intensity in residues in the N-terminal portion of the protein in several NMR spectra (^{1}H-1D, ^{1}H,^{15}N-HSQC and HNCO). The figure shows peak volumes obtained from HNCO spectra (^{1}H,^{15}N-HSQC spectra had many overlapping peaks). The loss of signal could be reversed by the addition of EDTA. Bottom) Effect of adding Zn^{2+} to solutions of Aβ40 on R2. Peaks in the N-terminal region of the peptide, especially H14, showed increases in R2. Effects on R1 were minor.

In agreement with other observers, some of the residues that lost signal intensity also showed chemical shift perturbations after addition of Zn^{2+} (Figure SI 4.15, showing ^{13}C-HSQC).[40,112,208,209] When the samples were centrifuged either at 16,000 or 100,000 x g,

the additional loss of signal was small (≤ 10%), and approximately the same at either relative centrifugal field (Figure SI 4.16). When EDTA was added to the remaining supernatant, this addition led to a small increase in signal intensity. This result is consistent with the idea that EDTA had reversed the aggregation of NanDOs into soluble but NMR-invisible flocs, i.e., invisible presumably due to line broadening.

We also measured R_1 and R_2 of Aβ40 in the absence and presence of Zn^{2+} sub-stoichiometric and stoichmetric Zn^{2+}, Aβ40 at 60 μM. There was no significant variation in R_1 upon addition of Zn^{2+}. R_2 however, showed a significant increase for the many of the same residues showing CSPs and loss of signal intensity with Zn^{2+}, i.e., in the N-terminal portion of the peptide (Figure 4.6 Bottom). These changes are consistent with interaction of Zn^{2+} in this region of the peptide leading to its rigidification. Notably, no such changes occurred in residues in the C-terminal region of the peptide.

Taken together, these results indicate that the aggregation of Aβ40 induced by the addition of Zn^{2+} differed substantially from that which leads to the formation of NanDOs. Whereas NanDOs remain in solution and involve interactions mainly among hydrophobic residues, especially those in two hydrophobic patches (residues 17-21 and 30-40), Zn^{2+} causes flocculation of the peptide through binding of the metal by residues in the N-terminal part of the peptide.

4.3 Discussion

In this paper, we have shown that Aβ40, even after disaggregation procedures, forms small flickering aggregates, which we term NanDOs (NanoDroplet Oligomers). NanDOs form immediately upon dissolving the peptide under conditions unfavorable for fibrillization, including peptide concentrations (peptide concentrations 12μM-120μM) far lower than those capable of forming fibrils. As a population, NanDOs remain present within the solutio and are indefinitely stable. These results are in basic agreement with a previous

study by another group[210], which used time-lapse high-speed AFM to study cross-linked (PICUP[211,212]) Aβ42 trimers, pentamers, and heptamers and visualize structural dynamics of these oligomers. The basic difference between the current study and the previous one (aside from the difference in Aβ isoform), is that in our study the molecules were not cross-linked. Thus, NanDOs represent interactions between Aβ40 native sequence molecules, including monomers.

NMR studies confirmed the presence of NanDOs. Although they represent a small portion of the total peptide population, there is a peptide concentration dependency of some of the chemical shifts in ^{13}C-HSQC spectra in one hydrophobic stretch of the sequence, residues 18-20. PRE experiments also indicate the role of the hydrophobic effect in the formation of these NanDOs, especially in the C-terminal region of the peptide. In contrast, addition of Zn^{2+} led to flocculation and changes in signal intensity and R_2 in the N-terminal region of the NMR. Although addition of Zn^{2+} caused some precipitation, changes were observable by NMR in the soluble peptide, which included an increased population of oligomers (as shown by AFM experiments).

Among the remaining questions is the relationship between NanDOs – a temporally stable population of flickering aggregates in which Aβ molecules associate and dissociate – and the larger soluble Aβ oligomers forming at higher Aβ concentrations, and associated with neurotoxicity in Alzheimer's disease. Whereas the cytotoxic oligomers progress to form insoluble amyloid fibrils over time, NanDOs were observed at peptide concentrations that did not support fibril formation. Rather, NanDOs constituted a stable population of flickering aggregates within the solution of Aβ40.

A model drawn from all of these results is in Figure 4.7.

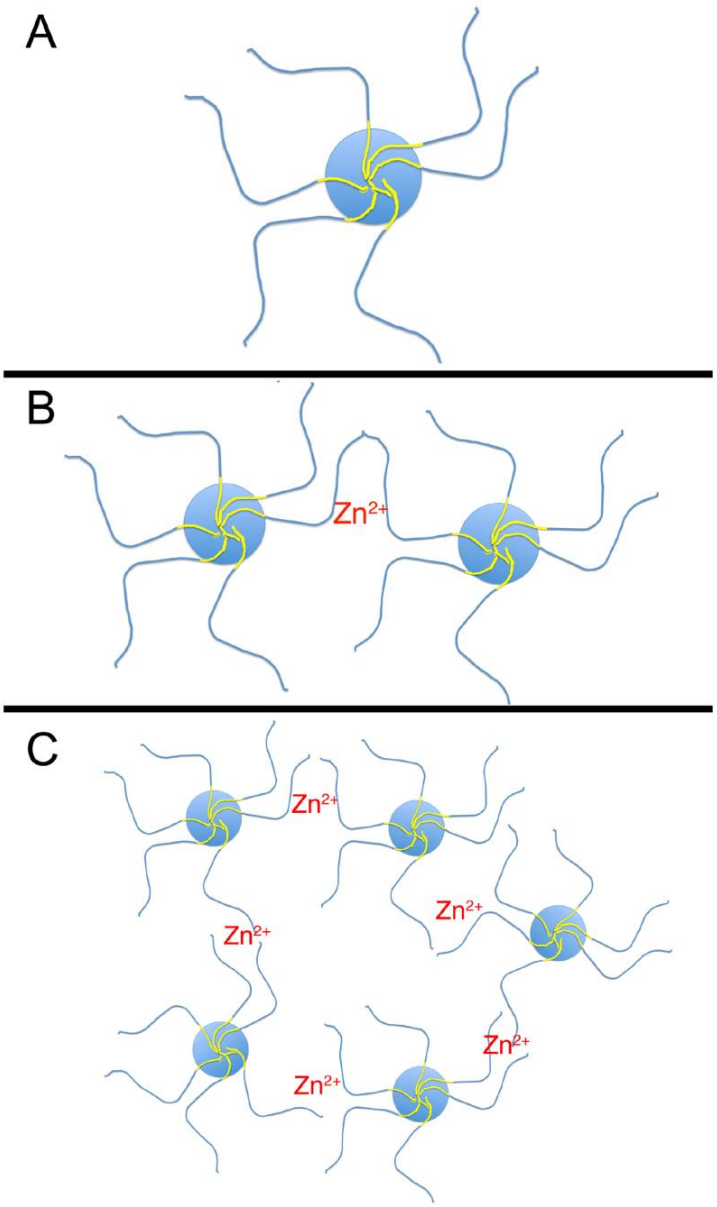

Figure 4.7 Model for the flocculation of NanDOs

Although the peptide molecules within NanDOs remain highly dynamic, as shown by both VSR-AFM and NMR, they are likely to represent a narrowing of the conformational spectrum of Aβ molecules due to intermolecular associations among hydrophobic residues. The addition of Zn^{2+} ions to a NanDO would be expected to cause further constraints upon the conformational repertoire of Aβ molecules. Put into the context of hetero-

geneous nucleation of Aβ aggregation, lipid surfaces (especially ganglioside/cholesterol-rich ones), which are known to catalyze Aβ aggregation, could represent an accentuation of the type of spontaneous intermolecular interactions that lead to the formation of NanDOs.[213,214] As shown in the model, Aβ aggregation into cytotoxic soluble oligomers and fibrils could proceed through a combination of modalities, all of which would be expected to be fostered by the initial transient associations occurring in NanDOs.

The mode of formation of NanDOs, through the hydrophobic effect, is reminiscent of micelle formation, but perhaps a more cogent parallel is to the phenomenon of pre-micelle formation. Amphiphilic molecules, in addition to assembling into micelles, often form smaller aggregates, termed premicelles, at concentrations below the CMC.[215–218] Evidence for premicelles comes from fluorescence spectroscopy[219–221], surface tension measurements[218,222,223], dynamic light scattering[224], molecular dynamics simulations[225,226], and NMR spectroscopy.[216,217,227–229] In many instances, premicellar amphiphiles can enhance catalytic rates.[230–234] A premicelle-forming biocompatible polymer has been shown to enhance the efficiency of drug delivery over traditional polymeric micelles.[235] One further example is of particular relevance to the aggregation of Aβ peptides is that of a star-like tetrameric quaternary ammonium surfactant, PATC, which forms premicelles that disassemble and clear mature Aβ40 fibrils in aqueous solution.[80] It is possible, therefore, that this amphiphile forms a mixed premicelle with Aβ40. Indeed, a great deal of recent investigation has shown that proteins, like other organic compounds and polymers, can undergo phase separation. NanDOs of Aβ40 may represent a premicellar species in the phase behavior of peptides and proteins.

4.4 Materials and Methods

4.4.1 Expression and purification of Aβ40

We expressed Aβ40 peptide, both unlabeled and labeled, for NMR spectroscopy as reported elsewhere.[236] Briefly, Aβ40 was expressed as an N-terminal hexaHis tag appended to Aβ40 by a Factor Xa cleavage site using a pET 28a vector. The plasmid was transformed into BL21(DE3)-pLysS E. coli cells by "Mix-and-Go" method from ZYMO Research Corp. Aβ40 has proven difficult to express in LB media, but is well expressed in minimal media containing either ^{14}N or ^{15}N in NH_4Cl as the sole nitrogen source. For ^{13}C-labeled Aβ40, ^{13}C-D-Glucose was used as the sole carbon source. After gene expression induced by addition of 1 mM isopropyl B-D-1-thiogalactopyranoside and cell growth for 4 hours after induction, cell pellets were stored in -20 ºC until further processed for purification. The protein was in inclusion bodies, which were solubilized using 5M urea with 0.1% (w/v) Triton X-100. The solubilized protein was subsequently purified by Ni-NTA affinity chromatography. The hexaHis tag was removed by Factor Xa enzymatic cleavage on Ni-NTA resin, after which the protein was further purified by HPLC. Immediately after elution from the Ni-NTA column using 5 ml of 500 mM imidazole, 50 mM Tris-HCl, pH 8.0, the pH was lowered to $\sim$ 3 by addition of 180 µL of neat trifluoroacetic acid (TFA). The peptide remained soluble under these conditions. Peptide was then purified by reverse phase HPLC using an Agilent 1100 Preparative HPLC, with a Zorbax PrepHT 300SB-C18 column (21.2 x 250mm, 7 µm beads), previously equilibrated with 20% (v/v) acetonitrile containing 0.1% TFA (v/v). Peptide was eluted using a linear gradient from 20 to 50% (v/v) acetonitrile over 52 min, with the column maintained at 60 °C. Eluent containing peptide was analyzed by mass spectrometry using an Agilent 6130 ESI/CI mass spectrometer, which showed m/z = 1443.96 for +3 ion, MW = 4328.86, expected molecular weight = 4329.9. Peptide solution was then frozen and lyophilized until needed. Purity of the peptide was also monitored by SDS-PAGE. Using this procedure, we purified unlabeled Aβ40, Aβ40 labeled with 15N and Aβ40 labeled with ^{15}N and ^{13}C in yields of ≥ 3 mg/L of culture medium.

4.4.2 Synthesis of Aβ40 and Cysteine mutants of Aβ40

Peptide synthesis of Aβ40 (NH2-DAEFRHDSGYEVHHQKLVF FAEDVGSNKGAIIGLMVGGVV-COOH), and of the same peptide with either Y10 or L34 mutated to C, was carried out using an Applied Biosystems 433A Synthesizer (Foster City, CA), essentially as described in earlier publications.[237] In general, Aβ40 was synthesized using the dipeptide Boc-Ser(Fmoc-Gly)-OH (Novabiochem) for G25-S26.[238] Standard Fmoc synthesis was carried out from residue 40 to N27. The dipeptide and HOBt (both 1 mmol) were dissolved in 2.5 mL of 3/1 = DCM/DMF (v/v), after which DIC (1.1 mmol) was added. After 10 minutes, the activated dipeptide formed; since the solution had formed a slurry, it was filtered through a syringe filter. The activated dipeptide was then added to the reaction vessel containing the resin and allowed to react with the deprotected peptide for 60 min. N-terminus of Aβ and the reaction vessel was vortexed for 60 min and vented every 10 min. Standard FMOC synthesis was resumed, beginning with V24 and continuing to the N-terminus. Peptide was cleaved from resin with 9.45 mL TFA, 0.25 mL H2O, 0.25 mL EDT, and 0.1 mL TIPS for 0.25 mmol peptide. This mixture was added to resin in an ice bath; after 5 minutes, cleavage was continued for 2h, room temperature. After filtration to remove resin, peptide was triturated by addition of cold diethyl ether. Peptide was dissolved in a small volume of 50/50/0.1 = Water/acetonitrile/TFA (v/v/v) and lyophilized. Peptides were purified by RP-HPLC as described previously.[236] When the isoacyl dipeptide strategy had been used, following RP-HPLC purification and lyophilization, the iso-acyl bond was converted to a peptide bond by dissolving it in 1 M NH_4HCO_3 (to $\sim$ 7) for 2 h, after which the Aβ peptides were re-purified by RP-HPLC.

For MTSL-Labeling of Aβ40 Cysteine Mutants, approximately 2-4 mg of dry Y10C-Aβ40 or L34C-Aβ40 was weighed into a 1.5mL Eppendorf tube. 50 µL of DMSO (FISHER BP231-100) was then added to the dry peptide, which was vortexed until solubilized. This liquid was the transferred into 3 mL of 20 mM sodium phosphate, pH 7.4, also containing 20 mM DTT. This mixture was incubated at room temperature for 30 minutes. After incubation,

the solution was desalted using an Econopak 10G Desalting Column (Bio-Rad 7322010) that had been washed previously with four column volumes of 20 mM sodium phosphate, pH 7.4 (no DTT). The first 3.5 ml of the eluent was retained in a 15 mL conical containing 70 mM MTSL dissolved in 50 µL of DMSO.[239] The MTSL-peptide mixture was incubated overnight at 4°C and purified by HPLC as described above. Labeling was verified using an Agilent 6130 ESI/CI mass spectrometer. For MTSL-Y10C-Aβ40, m/z = 1486.90 for the +3 ion (expected MW = 4453.8) and for MTSL-L34C-Aβ40, m/z = 1439.00 for the +3 ion (expected MW= 4502.82). For estimation of peptide concentration, peptides were dissolved in HFIP, and absorbance was measured at 205 nm using ε = 154490 M^{-1} cm^{-1}. In some experiments, concentrations were measured using BCA analysis that had been calibrated by amino acid analysis.[237]

4.4.3 Preparation of Aβ40 solutions

Aβ40 was first dissolved in hexafluoroisopropanol (HFIP) (TCI H0424) and incubated for 30 minutes at 22 °C. Concentration of Aβ40 in HFIP was estimated by A 274.5 nm, using ε = 1420 M-1 cm-1. Concentrations were later measure by Bradford assay, which had been calibrated from aliquots of Aβ40 on which amino acid analysis had been performed.[237] Peptide was lyophilized, re-dissolved in neat DMSO at ∼ 5 mM, and then incubated at 22 °C for 20 minutes. The peptide concentration and DMSO were adjusted so that the final DMSO concentration would be 3% (v/v). Aβ40 in neat DMSO was diluted to various peptide concentrations (25-300 µM) using cold (4°C) 4mM HEPES, pH 8.0. The pH was then adjusted to 7.3 using dilute HCl. For NMR experiments, D2O with DSS was added to 10% (v:v) of the solution (Aldrich 343773). In other experiments, the method of Fezoui et al.[199] was used to disaggregate Aβ40, i.e., solvation of the peptide with 1 mM NaOH followed by transfer to buffer. Identical NMR results were obtained with either method of disaggregation.

4.4.4 Zinc titrations of Aβ40

HFIP-treated, dry Aβ40 was prepared as described above. A 10 mM ZnCl2 solution was made in 4 mM HEPES, pH adjusted to 8.0. This solution was then filtered through a 0.22 µM filter (Steriflip Filter, Millipore Sigma). For titrations, the $ZnCl_2$ was added to the Aβ40 preparations, after which the solution was centrifuged at 16,000 x g for 10 minutes at room temperature. The supernatant was then taken from the samples and analyzed by AFM and NMR as described below.

4.4.5 Atomic Force Microscopy

All AFM experiments were conducted using an Asylum Research Cypher AFM, equipped with either the Environmental Scanner (ES) or Video Rate Scanner (VRS) modules.[240,241] Aβ40 was solubilized in 4 mM HEPES buffer and diluted to either 12 or 120 µM as described above. All AFM measurements were made in the "in solution" mode and at 20°C. Peptide solution was applied to freshly cleaved mica (Ted Pella, Product #50) and allowed to incubate for 30 minutes. The Olympus BL-AC40TS cantilever (Tip Radius ∼8nm, Spring Constant ∼0.09 N/m), a small, soft cantilever used for biological measurements, was used to acquire data on the Cypher ES. For VRS experiments, the Olympus BL-AC10 (Tip Radius ∼20nm, Spring Constant ∼0.1 N/m) was used to achieve significantly faster data acquisition of ∼ 625 Hz/line. Free amplitudes of tips were kept low (∼ 3 nm) for detection of possible particle fusion and division. Video rate scans are so denoted; all other scans were obtained using the Cypher ES module. All data were acquired using tapping mode AFM, with oscillation of the cantilever controlled by the Asylum blueDrive™ photothermal excitation method (1). Data analysis was done using Igor Pro's built in "imageThreshold" particle picking function, with a 1 nm cutoff for the selection mask (2). Once particles were chosen using the "imageThreshold" function, properties such as particle height could be acquired for either single particles or the population mean. Further data analysis and visualization was carried out using home built Python scripts.

4.4.6 NMR assignments and the peptide concentration of chemical shifts

NMR spectra were acquired on appropriately labeled (unlabeled, 15N- or 13C,15N-labeled peptides) of Aβ40 at 5, 10 and 20 °C. For most experiments, unless stated otherwise, peptides were 4 mM HEPES, at pH 7.0, 7.3 or, 8.0, in solutions containing 3% (v/v) dimethyl sulfoxide-d6, 0.1% DSS (as a chemical shift standard) and 10% D2O. The experiments were acquired on either a 500, 600 or 900 MHz Bruker spectrometer (with Topspin 3) at 5 °C. The 900 MHz spectrometer was equipped with cryogenic probe. HEPES was used at an internal pH standard. For experiments to assess chemical shift perturbations, and in general, pH was adjusted so that in 1H spectra, the HEPES peaks agreed with each other to < 001 ppm. To assess DMSO concentrations, experiments were conducted using dimethyl sulfoxide-d6 spiked with 0.001% (v/v) protonated DMSO and compared in 1D 1H to a calibration line.

NMR Assignments of Aβ40 were obtained at 5, 10 and 25 °C using a Bruker AVANCE IIIHD 600MHz spectrometer (University of Chicago Biomolecular NMR Facility), or in some instances, on a 900 MHz Bruker AVANCE NMR Spectrometer (University of Illinois, Chicago NMR Core). The following spectra were obtained: 1H-TOCSY, 1H-NOESY, HN-HSQC, HNCACB, HNCO, HC(CA)CO, and CBCA(CO)NH, 15N-edited-TOCSY, and 13C-edited-TOCSY (CHHC and HCCH).[242] Spectra were processed using either TopSpin[243], NMRPipe ,[134] and NMRFx,[244] and further analyzed using Sparky,[245] NMRView,[246] and CARA.[135] To assess Chemical Shift Perturbations (CSPs),[246] 15N-HSQC, 13C-HSQC and HNCO spectra were acquired at the following peptide concentrations: 25, 50 100, 200 μM.

4.4.7 NMR 15N-Relaxation experiments

The 15N spin-relaxation parameters T1, T2 and heteronuclear NOE were measured at peptide concentrations from 30 μM to 150 μM in increments of 15 μM at two magnetic fields 600MHz and 900MHz magnetic field strength. T1 experiments were acquired with

relaxation-delay of 0.01, 0.1, 0.2, 0.3, 0.4, 0.5, 0.6, 0.7, 0.8, 0.9, 1.0 and 1.25 s. For sample concentrations 150 μM and higher, a relaxation delay of 1.5 second was also used. The T2 experiments were carried out with relaxation-delay of 20, 40, 60, 80, 100, 120, 140, 160, 180, 200, 220, and 240 ms. These spectra were acquired using two magnetic field strength instruments, 600 and 900 MHz. 15N heteronuclear NOE experiments were acquired using a saturation and recycle-delay of 5 s. The data were processed using NMRPipe and analyzed using Sparky and NMRView software. The R1 and R2 (1/T1 and 1/T2, respectively) were calculated by non-linear least squares fit to a monoexponential equation.

4.4.8 Pulsed-field gradient based diffusion experiments

Pulsed field gradient (PFG) based NMR experiments were carried out to measure the translational diffusion constants of the peptide at 30 and 120 μM, at 20 °C. Experiments were carried out using a Bruker AVANCE IIIHD 600MHz spectrometer (University of Chicago Biomolecular NMR Facility), and a modified version of the pulse sequence stebpgpfp1s191d, which uses stimulated echo and bipolar pulse gradients. The experiment was acquired with gradient strengths varying from 2% to 98%, with intermediate increments of 5%. Signal intensities or peak volumes were analyzed using the following equation:[247]

$$I^2 = I_{max}{}^2 e^{-\gamma^2 g^2 \delta^2 (\Delta - (\delta/3)D} = e^{-bDg^2}$$

where I = signal intensity or peak volume, I_{max} = unattenutated signal intensity (47.73 Gauss cm^{-1} for the instrument used in these studies), g is the gradient fraction (fraction • Gmax), γ is the gyromagnetic ratio of the observed nucleus (for 1H, 2.68 x 104 rad $Gauss^{-1}$ s^{-1}), δ is the time length of the gradient (4 ms), Δ is the diffusion delay (0.15 s). Data were

analyzed by non-linear least squares fitting, using the equation:

$$I^2 = ae^{-bDg^2}$$

where a = G_{max}^2 and b is the aggregated parameter:

$$b = -\gamma^2\delta^2(\Delta - \frac{\delta}{3})$$

which yields Diffusion coefficient (cm^2s^{-1}).

4.4.9 Paramagnetic relaxation enhancement

For PRE experiments, ^{15}N-Aβ40 was mixed with ^{14}N-Y10C-MTSL-Aβ40 or ^{14}N-L34C-MTSL-Aβ40 at 1:1 = mol:mol in neat DMSO-d_6 (99.5 atom % D), and then diluted with buffer (typically 4 mM HEPES, pH 7.0, 7.3, or 8.0) to give final peptide concentrations of 200 μM, with 3% (v:v) DMSO and 10% D_2O containing 0.1% DSS. The peptide concentration, pH, buffer concentration, temperature, and DMSO concentrations have been varied in these experiments. pH is monitored using HEPES as an internal standard, and DMSO concentration is monitored using DMSO-d_6 spiked with 0.0001% protonated DMSO. ^{15}N HSQC spectra were acquired at 5 or 20 °C, typical using a 600 MHz Bruker Avance III spectrometer (University of Chicago Biomolecular NMR Facility). Typically, there were two control or reference spectra: 1) ^{15}N HSQC spectra of ^{15}N-Aβ40 peptide (at 100 and 200 μM) without ^{14}N-MTSL-Aβ40; 2) peptide reduced with 2.5 mM sodium ascorbate (RT, 3h) (which converts MTSL to diamagnetic form), after which 15N HSQC spectra are re-acquired. Although both reference methods gave similar results,

reduction with ascorbate was sometimes sub-quantitative, for which reason the reported experiments used ^{15}N-HSQC spectra of ^{15}N-Aβ40 as the reference. Ratios of peak volumes and intensities were measured using NMRView, and these were used to estimate the paramagnetic relaxation enhancement in Aβ40.

4.5 Supporting Information

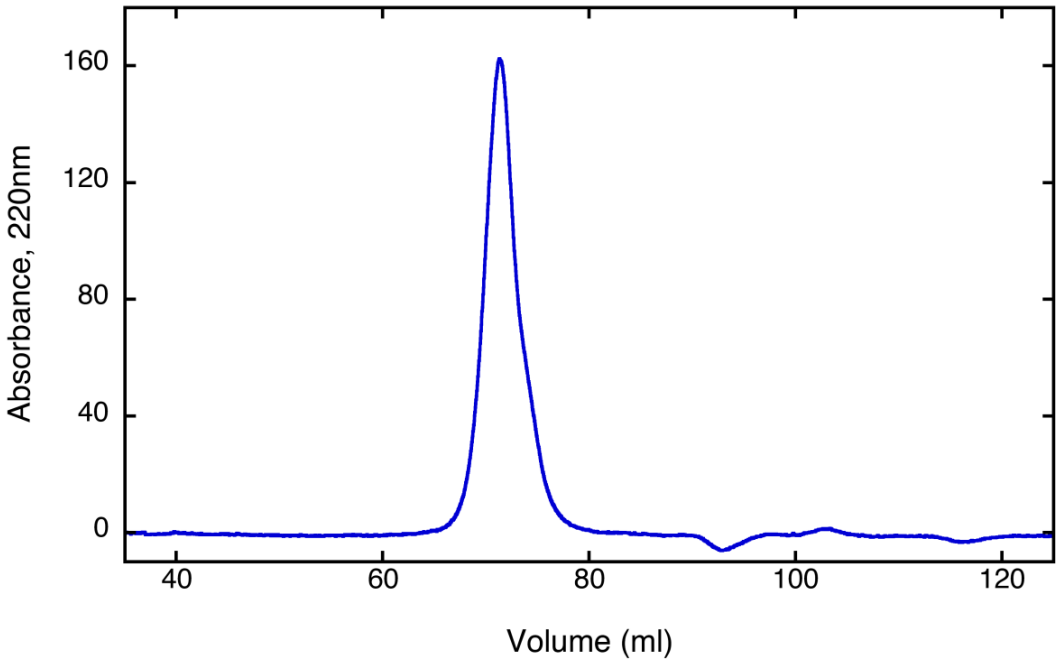

Figure 4.8 Size Exclusion Chromatography of Aβ40. A 120 μM solution of Aβ40 in 4 mM HEPES, pH 8.0, was analyzed using size exclusion chromatography (Superdex 75, Hiload 16/600) fitted to a BioRad Akta-Pure FLPC system. Eluent was the same buffer; flow rate was 1.0 ml/min; temperature was 20 °C. The peptide eluted as a single, symmetrical peak centered at 71 ml (Kav ≈ 0.4), corresponding to an apparent molecule weight of ≈ 6 kD, i.e., consistent with monomer or dimer (7-9).

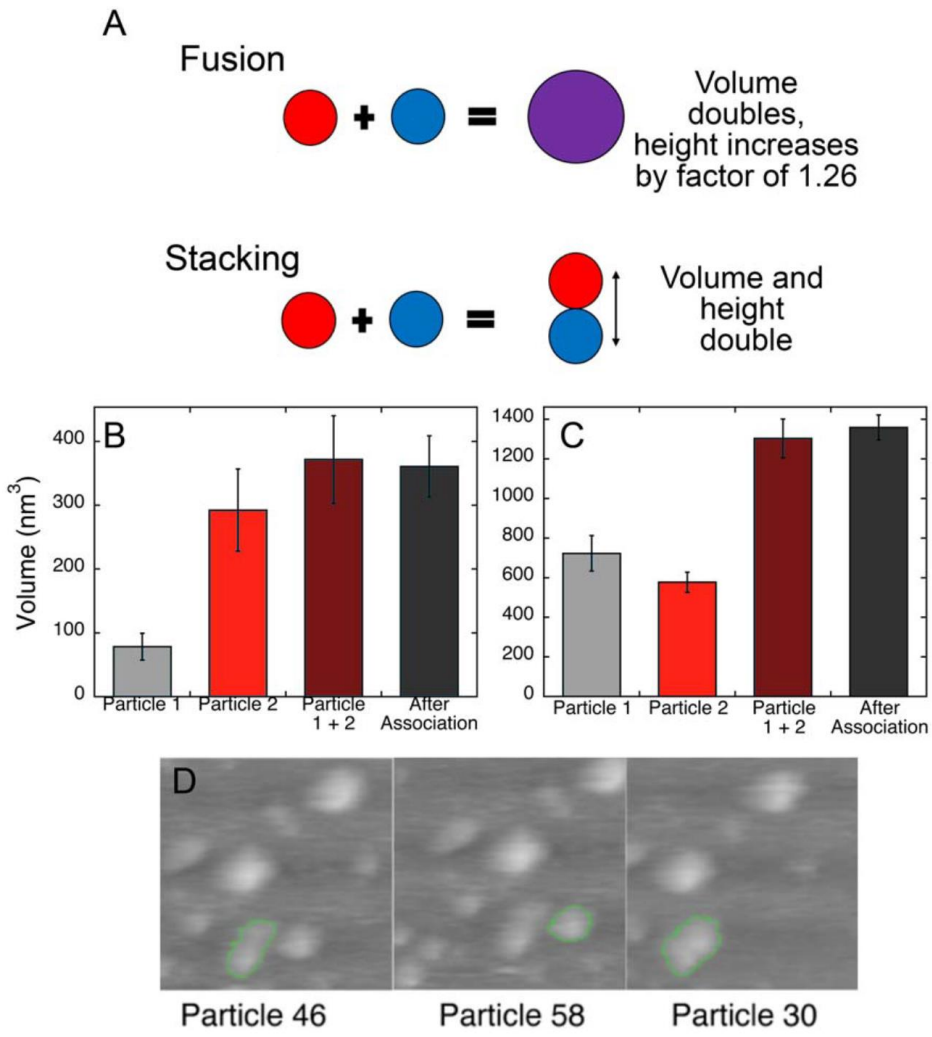

Figure 4.9 Analysis of VRS-AFM videos

A) The figure illustrates the hypothetical cases of two spherical particles, each with one volume unit, either stacking or fusing. If the two particles stack on top of one another, both the height and volume double. If they fuse, the volume still doubles, but the height increases by only a factor of 1.26, i.e., $2^{\frac{1}{3}}$.VRS-AFM movies indicated that droplets were fusing, which we tested as follows. Particle volume and height were measured before

and after a pair or droplets fused, using the flattening and masking features of Igor Pro's "imageThreshold" function, with a 1nm cutoff (similar to the method in the previous section). The heights and volumes were collected and recorded for 10-15 frames before and after the particle association. The average and standard deviation were then calculated for each particle. As shown in the Figure SI 4.9 b and c, tracking the volume of VRS data frame by frame, and averaging the volume across these frames for each individual particle before and after association, clearly shows conservation (within the 95% confidence interval) of the additive volumes of the particles, suggesting fusion. Similar measurements of heights shows that while there is only a slight increase in height after fusion, this clearly is less than additive, again suggesting fusion rather than simple stacking of one rigid particle upon another. Three examples of the particle selection procedure used to generate the above data are shown in Figure SI 4.9 d (see also Table SI 1). Particles are tracked individually for height and volume. Of the three particles shown in the illustrative example, below, Particles 46 and 58 are pre-fusion, while Particle 30 is actually two particles fusing.

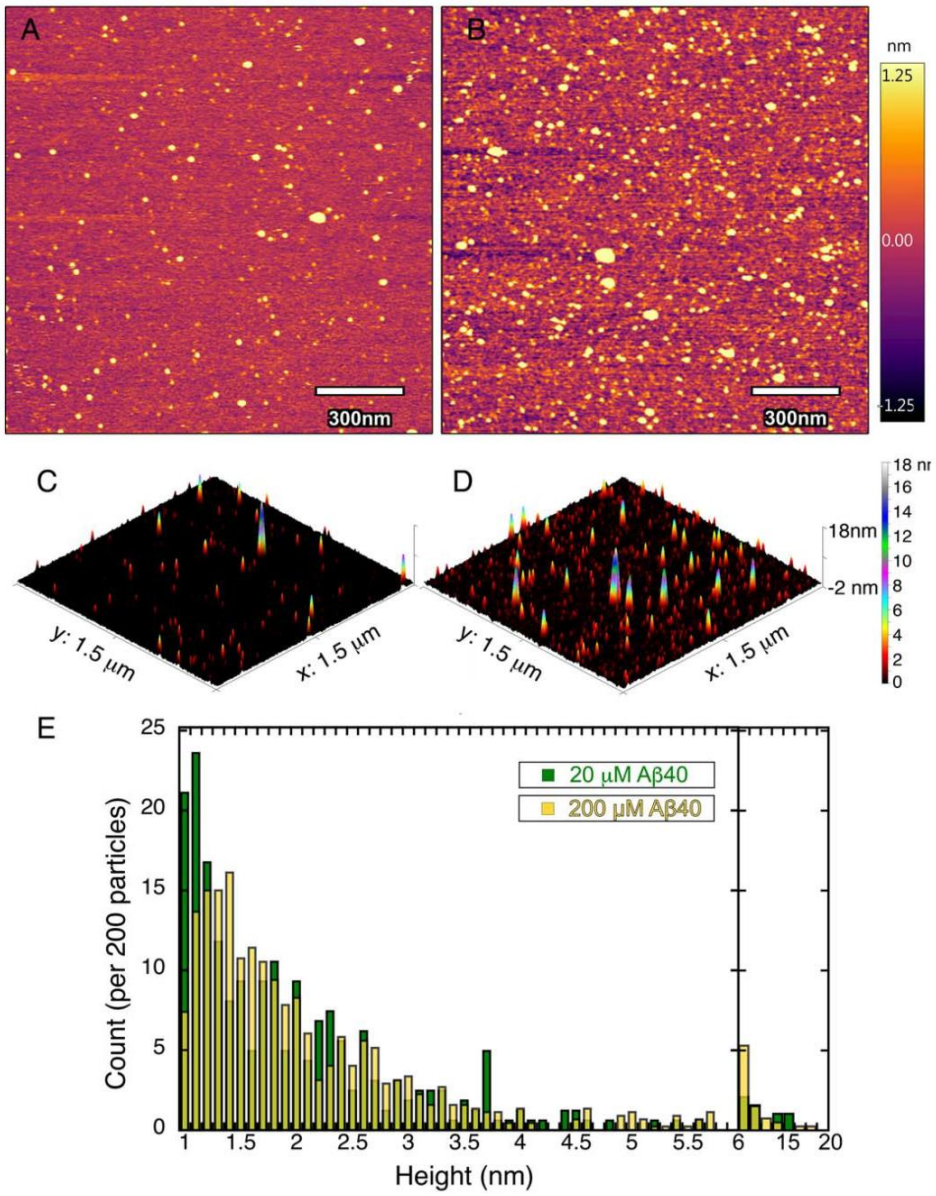

Figure 4.10 In-solution AFM of Aβ40 at 12 µM (A, C) and 120 µM (B, D). Scale bar = 300 nm. B and D represent three-dimensional projections of particle heights. E. Histogram of particle volumes (nm3) at 12 µM (green) and 120 µM (yellow)

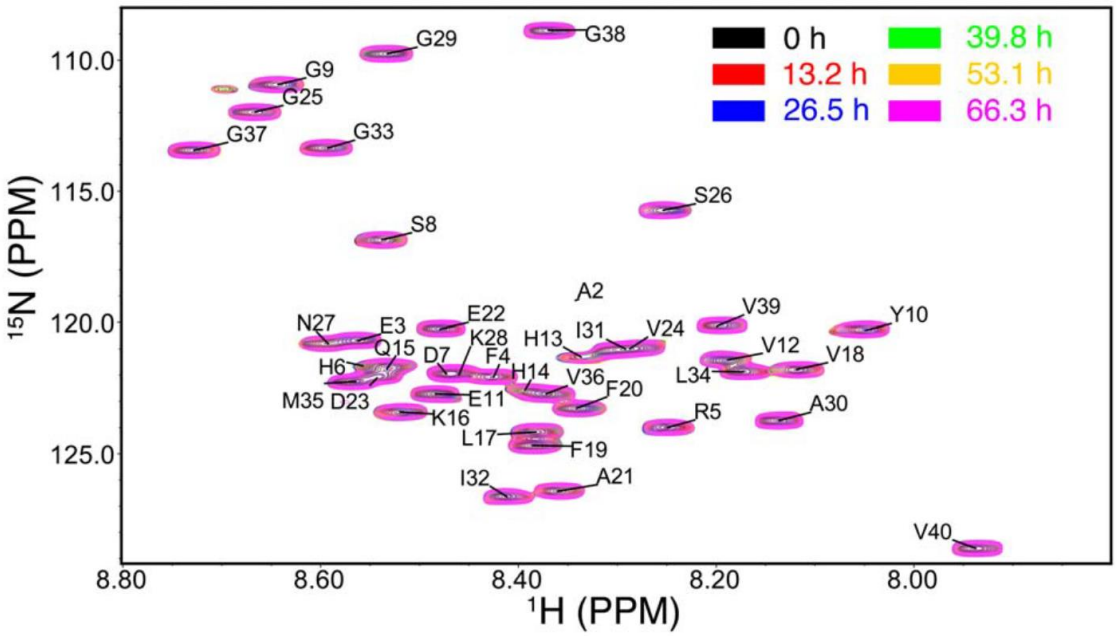

Figure 4.11 Sequential ^{15}N-HSQC spectra of Aβ40, in 4 mM HEPES, pH 7.3, 5°C at the times indicated in the figure, showing essentially no change over the course of 3 days. Similar spectra have been obtained at longer time points, up to 2.5 weeks.

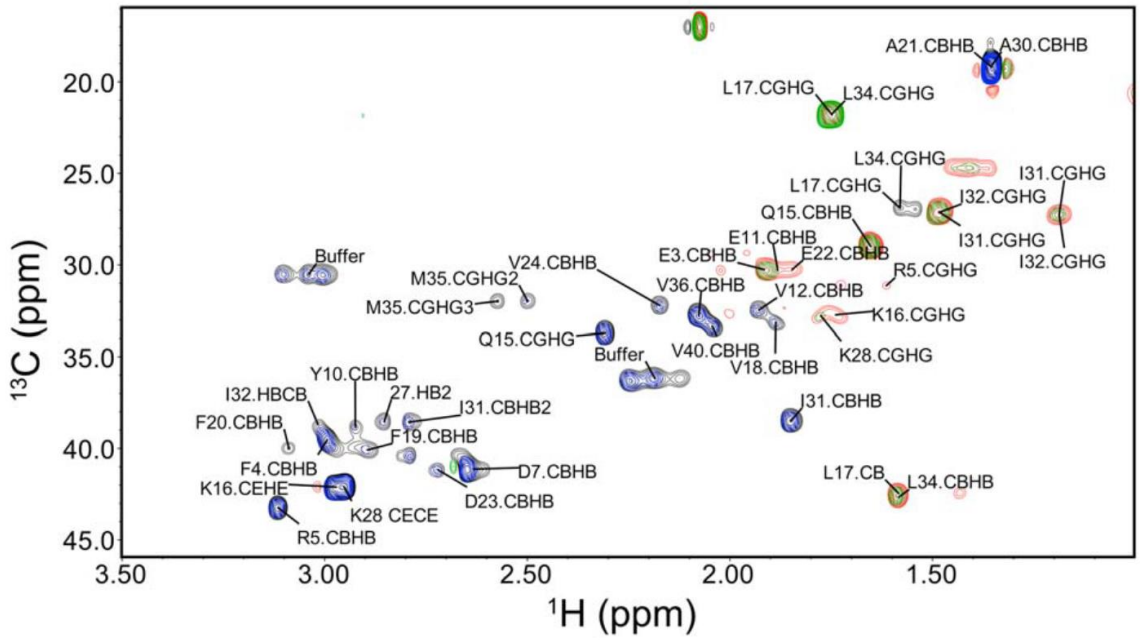

Figure 4.12 Portion of the ^{13}C-HSQC spectrum of 15 and 120 μM ^{15}N,^{13}C-Aβ40, in 4 mM HEPES, pH 7.3, 20 °C, showing mainly side chain peaks (Cβ, Cγ, and Cε atoms). For the spectrum at 120 μM 15N,13C-Aβ40, black peaks are positive, red are negative; for the spectrum at 15 μM 15N,13C-Aβ40, blue peaks are positive, green are negative. Figure 2 of the article shows the portion of the spectrum with peaks for Cα atoms.

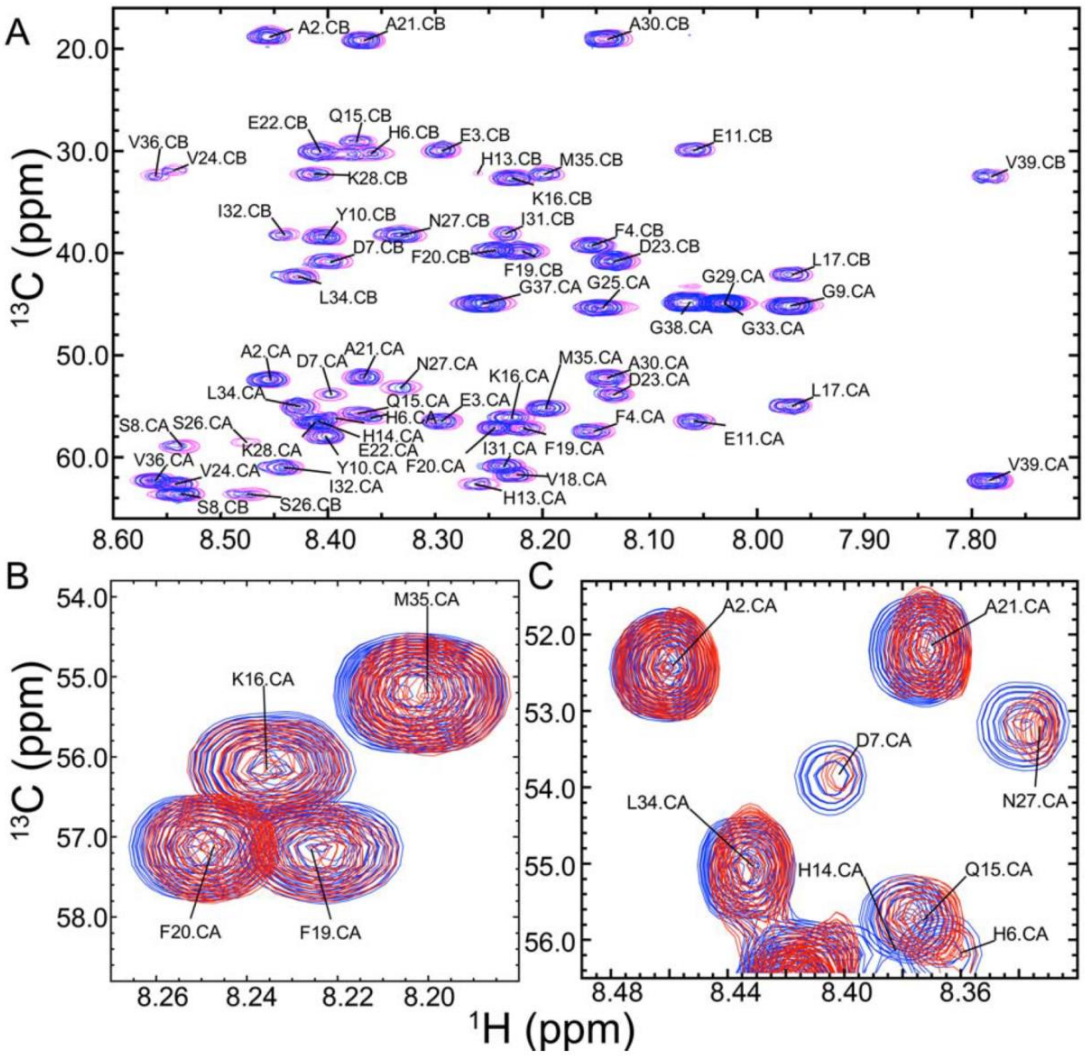

Figure 4.13 HNcoCACB spectra of Aβ40 at 15 and 120 μM (magenta and blue, respectively), in 4 mM HEPES, pH 7.3, 20 °C. Because of extensive peak overlap in ^{13}C-HSQC spectra, and in order to take CSPs in the ^{15}N and ^{1}H,^{15}N dimensions into account, we acquired HNcoCACB spectra, at peptide concentrations of 15, 30, 60,and 120 μM, which resolved the Cα and Cβ peaks and had sufficient signal even at the lowest of these peptide concentrations. Small chemical shift perturbations were observed in these spectra (Panels b and c): M35.CA, F20.CA (Panel b), D7.CA, A21.CA, N27.CA, Q15.CA, and L34.CA (Panel c) had observable chemical shift changes, while K16.CA (Panel b) and A2.CA (Panel c) did not.

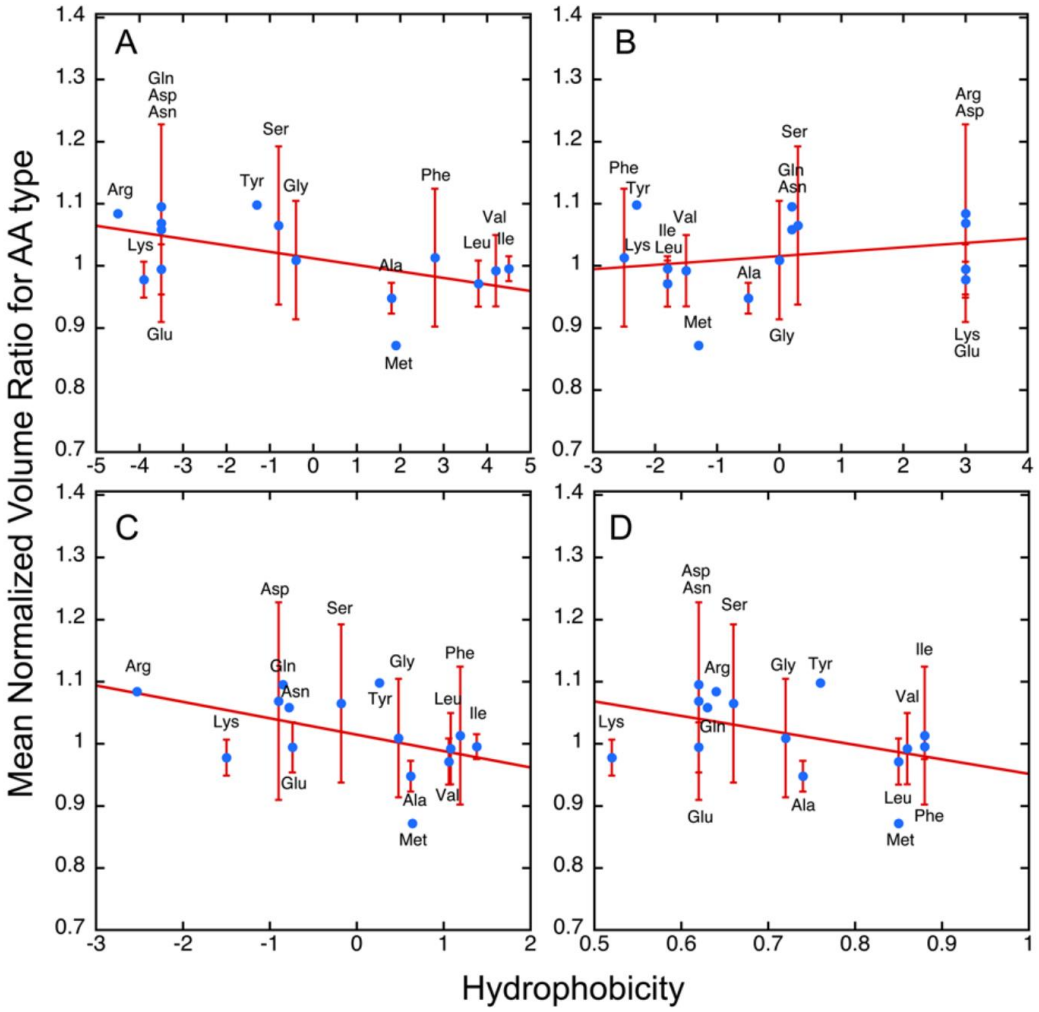

Figure 4.14 Correlation between signal intensity and amino acid hydrophobicity.The figure shows four hydrophobicity scales: A) Kyte and Doolittle[248]; B) Eisenberg[249]; C) Hopp and Woods[250] and D) Rose[251]. See also Table SI 4.11

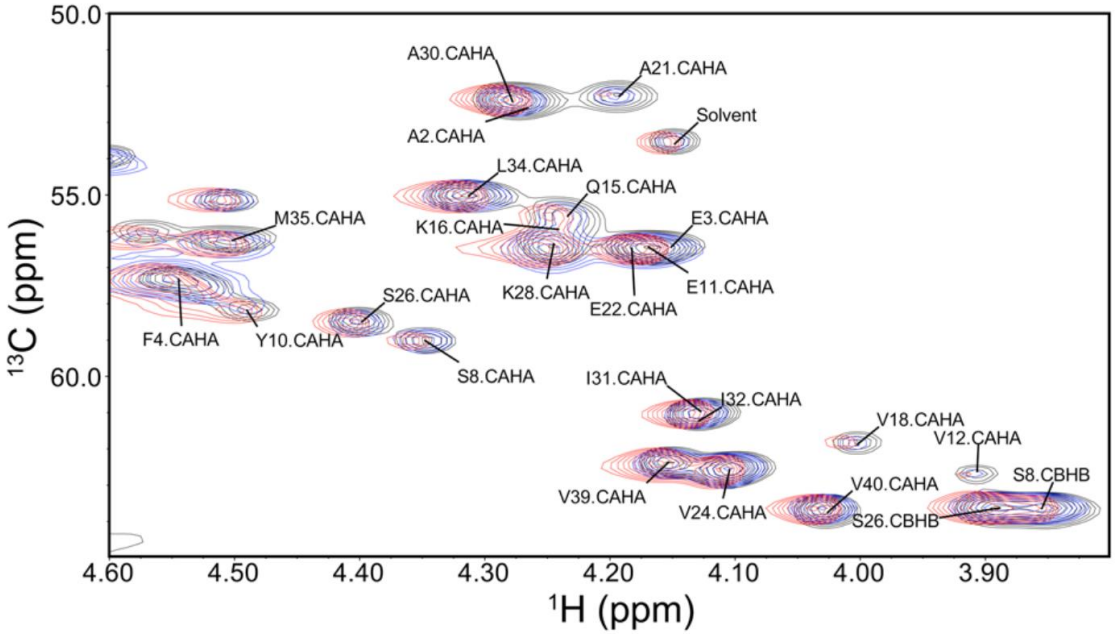

Figure 4.15 Chemical Shift Perturbations in ^{13}C-HSQC spectra of Aβ40 after the addition of Zn^{2+} and EDTA. One spectrum (black) shows 60 μM ^{15}N,^{13}C-Aβ40 at 5°C, pH 7.3. Superimposed are two additional spectra: the same sample after the addition of 30 μM $ZnCl_2$ and rigorous pH matching (red); and the same sample after the further addition of 30 μM EDTA and rigorous pH matching (blue). The figure shows the portion of the spectrum showing mainly Cα peaks. In agreement with other observers, some of the residues that lost signal intensity also showed chemical shift perturbations after addition of Zn^{2+}.

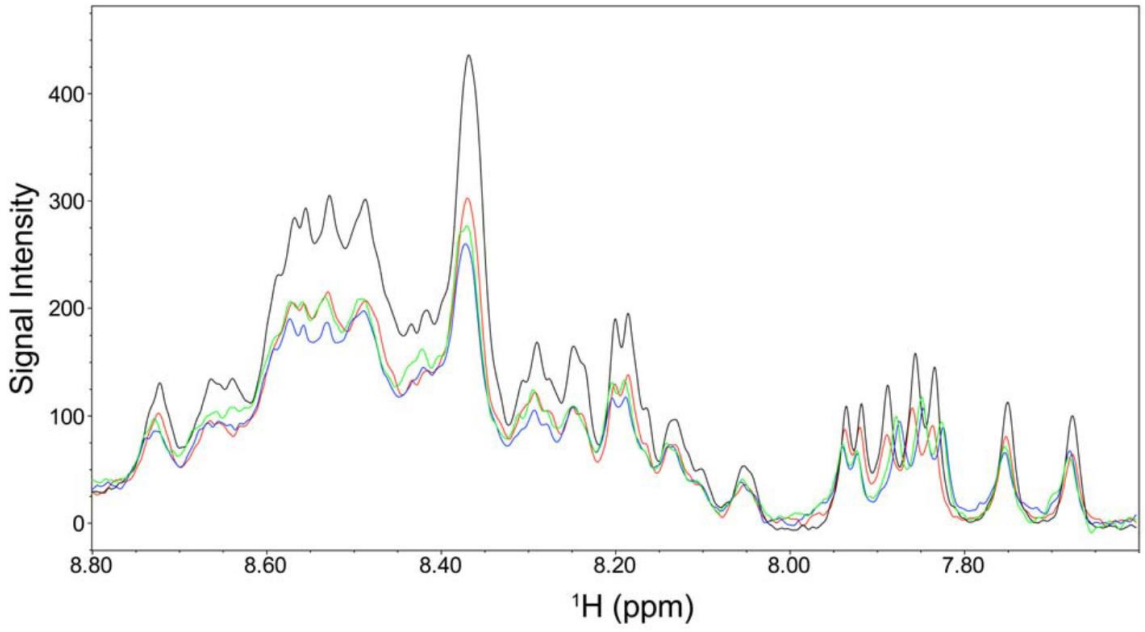

Figure 4.16 As described in the main text, adding Zn^{2+} to solutions of Aβ40 led to a striking decrease in signal intensity, especially in residues in the N-terminal portion of the peptide. The figure shows ^{1}H NMR spectra of 40 μM Aβ40 before (black) and after (red) addition of near-stoichiometric Zn^{2+}. Since a small amount of precipitate formed after addition of Zn^{2+}, the loss of peptide as precipitate was estimated as follows. The samples were centrifuged either at 16,000 (not shown) or 100,000 x g and the ^{1}H NMR spectrum was acquired (red). Centrifugation at either relative centrifugal field, even the ultracentrifugal field, resulted in little additional loss of signal. When EDTA was added to the remaining supernatant, and this addition led to a small increase in signal intensity (green), suggesting that EDTA had caused re-dispersal of flocs that were NMR-invisible but nonetheless still in solution.

Table 4.1: Statistical analysis of In-Solution VRS-AFM for Figure 1.1 Top

Aβ40 = 12 μM	Height (nm)	Volume (nm ^{3})
Red Arrow (Pre-Assoc.)	6.2 $\pm$ 0.4	574.6 $\pm$ 54.3
Blue Arrow (Pre-Assoc.)	5.6 $\pm$ 0.4	724.6 $\pm$ 93.0
Purple Arrow (Post-Assoc.)	6.5 $\pm$ 0.5	1357.7 $\pm$ 71.0

Table 4.2: Statistical analysis of In-Solution VRS-AFM for Figure 1.1 Bottom

Aβ40 = 1 μM	Height (nm)	Volume (nm ^{3})
Red Arrow (Pre-Assoc.)	4.1 $\pm$ 0.4	292.3 $\pm$ 68.1
Blue Arrow (Pre-Assoc.)	5.6 $\pm$ 0.4	79.0 $\pm$ 20.2
Purple Arrow (Post-Assoc.)	3.6 $\pm$ 0.4	359.2 $\pm$ 50.7

Table 4.3: Proton chemical shifts, 60 µM Aβ40 in 4 mM HEPES, pH 7.30, 20°C Amino acids 3 - 20

Residue	HN	Hα	Hβ	Hβ	Hγ	Hγ	Hδ
E3	8.47	4.16	1.86	1.9	2.1	2.18	
F4	8.31	4.53	2.98				
R5	8.16	4.24	2.16				3.1
D7	8.37	4.59	2.63				
S8	8.41	4.35	3.84				
G9	8.55	3.84					
Y10	7.97	4.48	3	2.91			
E11	8.41	4.17	1.9		2.14	2.17	
V12	8.08	3.91	1.92		0.75	0.84	
Q15	8.41	4.22	1.95		2.3		
K16	8.39	4.25	1.78		1.71		
L17	8.25	4.3	1.53	1.58	1.42		0.81
V18	7.99	4	1.87		0.72	0.8	
F19	8.25	4.56	2.87	2.96			
F20	8.24	4.55	3.07				

Table 4.4: Proton chemical shifts, 60 μM Aβ40 in 4 mM HEPES, pH 7.30, 20°C Amino acids 21 - 40

Residue	HN	Hα	Hα	Hβ	Hβ	Hγ	Hδ	Hδ
A21	8.26	4.2		0.942				
E22	8.38	4.18		1.9	2.01	2.24		
D23	8.43	4.62		2.61	2.71			
V24	8.17	4.12		1.84		0.85		
G25	8.56	3.95						
S26	8.16	4.4		3.88				
N27	8.49	4.71		2.77	2.85			
K28	8.35	4.24		1.86		1.75		
G29	8.43	3.89						
A30	8.04	4.28		1.34				
I31	8.16	4.1		1.71				
I32	8.27	4.13		1.83		1.18	0.89	
G33	8.47	3.91						
L34	8.05	4.32		1.57			0.9	0.85
M35	8.45	4.5		2.05		2.48		
V36	8.23	4.1		2.06		0.92		
G37	8.59	3.95						
G38	8.72	3.92	3.99					
V39	8.08	4.15		2.06		0.91		
V40	7.81	4.03		2.03		0.87		

Table 4.5: Proton chemical shifts, 60 μM Aβ40 in 4 mM HEPES, pH 7.30, 5°C Amino acids 3 - 20

Residue	HN	Hα	Hβ	Hβ	Hγ	Hδ
E3	8.56	4.13	1.86		2.13	
F4	8.42	4.51	2.96			
R5	8.25	4.21	1.60		1.46	3.09
H6	8.61	121.03	4.94			
D7	8.47	4.58	2.63			
S8	8.54	4.33	3.85			
G9	8.64	3.86				
Y10	8.05	4.46	2.94			
E11	8.49	4.15	1.82		2.14	
H13	8.40	121.93				
H14	8.40	122.46	4.55			
Q15	8.52	4.22	1.96			
K16	8.51	4.23	1.71		1.37	
L17	8.38	4.28	1.56		1.43	0.84
V18	8.11	3.98	1.87		0.76	
F19	8.38	4.53	2.90			
F20	8.34	4.52	2.88	3.04		

Table 4.6: Proton chemical shifts, 60 μM Aβ40 in 4 mM HEPES, pH 7.30, 5°C Amino acids 21 - 40

Residue	HN	Hα	Hβ	Hγ	Hδ
A21	8.37	4.17	1.32		
E22	8.48	4.15	1.89		
D23	8.54	4.60	2.65		
V24	8.27	4.09	2.15	0.91	
G25	8.67	3.93			
S26	8.26	4.38	3.85		
N27	8.60	4.69	2.79		
K28	8.47	4.22		1.76	
G29	8.54	3.88			
A30	8.14	4.26	1.33		
I31	8.30	4.10	1.81	1.18	0.85
I32	8.41	4.11	1.82	1.18	0.88
G33	8.59	3.88			
L34	8.17	4.29	1.56		0.84
M35	8.56	4.48	1.99	2.52	
V36	8.36	4.08	2.05	0.92	
G37	8.73	3.94			
G38	8.37	3.93			
V39	8.20	4.14	2.04	0.89	
V40	7.93	4.00	2.01	0.87	

Table 4.7: ^{13}C and ^{15}N Chemical Shifts, 60 μM Aβ40 in 4 mM HEPES, pH 7.30, 20 °C, Amino acids 3-20

Residue	HN	N	CO	Cα	Cβ
A2			177.33	52.66	19.17
E3	8.47	120.31	176.07	56.78	30.27
F4	8.3	121.63	175.26	57.77	39.5
R5	8.15	123.57	175.61	57.78	31.09
H6	8.41	121.11	175.13	56.71	30.65
D7	8.36	121.65	176.33	54.12	41.1
S8	8.39	116.44	175.15	59.1	64
G9	8.54	110.62	174.03	45.42	
Y10	7.97	119.96	175.78	58.35	38.74
E11	8.42	122.34	176.32	56.78	30.27
V12	8.07	120.78	176.11	62.91	30.17
H13	8.25	122.1	176.06	62.76	
H14	8.25	122.26	175.37	56.71	
Q15	8.38	121.15	175.71	56.17	29.34
K16	8.37	122.68	176.2	56.57	32.83
L17	8.23	123.66	176.78	55.2	42.33
V18	7.97	121	175.16	62.15	32.83
F19	8.23	123.92	174.88	57.34	40.05
F20	8.23	122.55	174.86	57.33	39.89

Table 4.8: ^{13}C and ^{15}N Chemical Shifts, 60 μM Aβ40 in 4 mM HEPES, pH 7.30, 20 °C, Amino acids 21-40

Residue	HN	N	CO	Cα	Cβ
A21	8.25	125.86	177.32	52.56	19.48
E22	8.37	119.82	176.18	56.76	30.4
D23	8.42	121.57	176.63	54.33	41.15
V24	8.14	120.38	177.07	62.8	32.12
G25	8.55	111.54	174.58	45.51	
S26	8.15	115.46	174.58	58.61	63.77
N27	8.49	120.52	174.62	53.36	38.46
K28	8.34	121.63	177.18	56.89	32.49
G29	8.42	109.34	173.78	45.27	
A30	8.03	123.48	177.65	52.58	19.36
I31	8.15	120.37	176.41	61.14	38.22
I32	8.24	125.67	176.65	61.43	38.39
G33	8.45	112.67	173.77	45.27	
L34	8.04	121.56	177.29	55.23	42.63
M35	8.43	121.67	176.14	55.35	32.46
V36	8.2	121.86	176.64	62.53	32.54
G37	8.57	112.8	174.46	45.27	
G38	8.26	108.64	173.75	45.18	
V39	8.07	119.73	175.47	62.57	32.67
V40	7.79	127.98	180.96	63.6	33.06

Table 4.9: ^{13}C and ^{15}N Chemical Shifts, 60 μM Aβ40 in 4 mM HEPES, pH 7.30, 5 °C, Amino acids 3-20

Residue	HN	N	CO	Cα	Cβ
A2	8.56	120.66	177.31		
E3	8.55	120.66	176.06	56.63	30.41
F4	8.44	122.05	175.27	57.64	39.61
R5	8.26	123.94	175.57	55.58	31.08
H6	8.56	121.64	174.90	56.19	30.42
D7	8.47	121.85	176.33	54.18	41.11
S8	8.54	116.84	175.20	59.10	63.80
G9	8.64	110.91	174.04	45.44	
Y10	8.05	120.25	175.82	58.27	38.72
E11	8.48	122.64	176.24	56.62	30.44
V12	8.18	121.41	175.10	62.89	32.33
H13	8.31	121.07	175.10	62.94	
H14	8.39	122.39	176.01	56.81	
Q15	8.52	121.72	175.69	56.15	29.47
K16	8.51	123.44	176.25	56.36	32.90
L17	8.38	123.21	176.80	55.17	42.44
V18	8.11	121.72	175.14	61.97	33.37
F19	8.38	124.64	174.80	57.59	40.16
F20	8.34	123.19	174.77	57.30	40.13

Table 4.10: ^{13}C and ^{15}N Chemical Shifts, 60 μM Aβ40 in 4 mM HEPES, pH 7.30, 5 °C, Amino acids 21-40

Residue	HN	N	CO	Cα	Cβ
A21	8.36	126.37	177.29	52.32	19.34
E22	8.48	120.20	176.16	56.61	30.43
D23	8.54	122.09	176.16	54.20	41.10
V24	8.27	120.94	177.12	62.92	32.29
G25	8.66	111.95	174.54	45.49	
S26	8.24	115.69	174.51	58.58	63.88
N27	8.58	120.73	175.20	53.27	38.55
K28	8.46	121.92	177.22	56.66	32.44
G29	8.52	109.71	173.72	45.03	
A30	8.13	123.72	177.66	52.35	19.30
I31	8.29	120.92	176.46	61.04	38.24
I32	8.41	126.53	176.66	61.19	38.44
G33	8.59	113.27	173.70	45.03	
L34	8.17	121.77	177.34	55.17	42.57
M35	8.55	122.16	176.18	55.22	32.45
V36	8.56	122.13	176.72	62.50	32.79
G37	8.73	113.34	174.46	45.08	
G38	8.37	108.79	173.70	45.01	
V39	8.19	120.00	175.58	62.47	32.86
V40	7.92	128.49	181.00	63.49	32.84

Table 4.11: Correlation between hydrophobicity and PRE effect

Scale	Y-Intercept	Slope	Error Y-Intercept	Error Slope	Chi-Sq	R
Kyte-Doolittle	1.01	0.01	-0.01	0.00	0.04	0.55
Hopp-Woods	1.02	0.02	0.01	0.01	0.05	0.23
Eisenber	1.02	0.02	-0.03	0.01	0.04	0.48
Cornette	1.02	0.02	-0.01	0.01	0.05	0.37
Rose	1.18	0.10	-0.23	0.13	0.05	0.44
Janin	1.01	0.02	-0.04	0.02	0.05	0.43
Engelman	1.01	0.02	-0.01	0.00	0.04	0.46
OI	1.01	0.02	0.01	0.02	0.05	0.21
tt	1.02	0.02	-0.01	0.01	0.05	0.21

CHAPTER 5

DISCUSSION

5.1 Future Work on the NanoDroplet Oligomers of Aβ

The NanoDroplet Oligomers (NanDOs) of Aβ may represent a premicellar holding pattern that can occur at small concentrations of Aβ (1uM). There are several questions raised with the discovery of these NanDOs: Where do NanDOs fit into the pathway of Aβ aggregation? Are they neurotoxic? Do they lead to the formation of more neurotoxic oligomers? It is critical when exploring these questions that the production and identification of the NanDO is consistent in methods used and described in **Chapter 4**.

First, Aβ must undergo a disaggregation procedure using either hexafluoroisopropanol or NaOH. This is key to removing pre-aggregates that can seed Aβ monomers and presents an opportunity for accurate concentration determination using fluorescence and Amino Acid Analysis (AAA).[237] Second, samples must be brought up to volume in cold, low-salt buffer at Aβ concentrations below the concentration necessary for fibril formation $\leq 120\mu$M. NanDO formation will occur almost instantly after preparation. However, NanDO lifetimes will be significantly longer at cold temperatures (5°C) compared to room temperatures. Third, since the buffer contains little salt, it is subject to very sensitive changes in pH. Therefore, initial pH measurements of the sample using standard pH probes must be done after the addition of the buffer to the peptide. This is because during the HPLC purification of Aβ peptides (expressed or synthetic), TFA in the water/acetonitrile running buffer is transferred along with the pure Aβ peptide, which lowers the pH when the sample is prepped after drying. For concentration and metal titration experiments in **Chapter 4**, I performed a method of pHing the samples by matching the resonance of an internal indicator in a 1D ^{1}H experiment to the resonance of the indicator in a new sample as detected by NMR. The method is relatively straight forward, requiring that small

amounts of acid (HCl) or base (NaOH) solution be added to the NMR tube in between acquisitions. This is necessary to do due to the impact that pH has on the resonance of spin systems in 1D, 2D or 3D NMR experiments. Inaccurate pH between experiments can result in mistaking chemical shift perturbations or signal changes for peptide/peptide interactions.

As a described in **Chapter 4**, NanDOs are a low population species (5-10%) of the total Aβ mass. To detect their presence, I turned to methods and techniques equipped to analyze slight changes in samples populations. This included Atomic Force Microscopy, diffusion and PRE NMRS. Moving ahead, these techniques will be invaluable in understanding the transition from the NanDO to larger, more neurotoxic oligomer species. Larger Aβ40 oligomers ($\sim$10 nm) are shown to have in-parallel β-sheets and are ThT sensitive[67]. If NanDOs are pushed to aggregate via buffer change, then this transition can be detected with the above methods.

There is more to explore in respect to heterogeneous nucleators of NanDOs. **Chapter 4** shows that the addition of Zinc drives the flocculation and precipitation of NanDOs through the N-terminal region. Other metals, both trivalent and divalent, could be explored to expose the varying degree of flocculation or dissociation caused to the NanDO. Micelles and membranes made of lipids with varying charateristics, such as head charge and chain length, may influence the formation of NanDOs or drive it towards further aggregation through structural rearrangements.

5.2 Detecting Polymorphism in Oligomers

As discussed in **Chapter 1** and **Chapter 2**, polymorphism is a feature of Aβ fibrils that is dependant on several factors including sequence and growth conditions. In a recent experiment to see if sequence impacts fibril morphology, I incubated human, mole rat and mouse Aβ40 in the the same growth conditions. The Aβ amino acid sequence between

the three species is mostly the same except H13 in mole rats and G5,F10 and H13 in mice compared to the human Aβ sequence, respectively.[252] As seen in Figure 5.1, the human fibrils are short and striated while the rodents are longe with distint twists. Given that polymorphism can impact fibril morphology and toxicity, the questions must be asked: Does polymorphism extend to oligomers? Are some oligomers more toxic than other because of this polymorphism? Seeding with Aβ fibril fragments acts as a catalyst and increases the number of oligomers in the sample. The process of nucleation-polymerization is toxic and could be key to oligomer toxicity rather than the isolated oligomers themselves.[253–255] Turning to seeding methods to grow oligomers as described above and capture them using filtration and freeze-trapping a la methods carried out by Chimon et al will present opportunities to study them while hopefully preserving their structure.[256] Using amyloid-fibrils grown from species specific sequences and human tissues, ssNMR methods and site-specific labeling strategies will provide many advantages to detecting and measuring oligomer polymorphism at the molecular level.

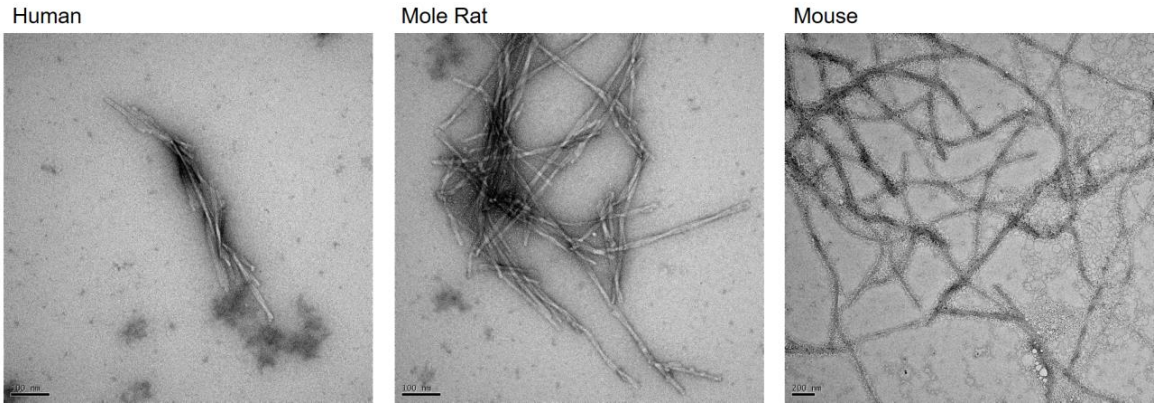

Figure 5.1 Aβ40 fibrils of the human, mole rat and mouse sequences.

5.3 Concluding Remarks

As we enter a new decade, questions and answers about Aβ and Alzheimer's Disease grow in complexity and challenge. Amyloid-beta small oligomers are tucked away in

the limits of many of our technologies and therefore require new innovative approaches. Whether or not an accurate ”structure” of the Aβ small oligomer will ever be obtained is unknown, as much evidence points to them as being unstructured. However, there is much being revealed about how these small oligomers form and cause neurotoxicity. By understanding the mechanism of their formation at an atomic level, we are another step closer to completing the picture on Aβ’s role in AD and hopefully, a step closer to developing treatments that can effectively interact with Aβ.

REFERENCES

1. Fagan, A. M.; Xiong, C.; Jasielec, M. S.; Bateman, R. J.; Goate, A. M.; Benzinger, T. L.; Ghetti, B.; Martins, R. N.; Masters, C. L.; Mayeux, R.; Ringman, J. M.; Rossor, M. N.; Salloway, S.; Schofield, P. R.; Sperling, R. A.; Marcus, D.; Cairns, N. J.; Buckles, V. D.; Ladenson, J. H.; Morris, J. C.; Holtzman, D. M. Longitudinal change in CSF biomarkers in autosomal-dominant Alzheimer's disease. *Science Translational Medicine* **2014**, *6*.

2. Deture, M. A.; Dickson, D. W. The neuropathological diagnosis of Alzheimer's disease. *Molecular Neurodegeneration* **2019**, *14*, 1–18.

3. Stelzmann, R. A.; Norman Schnitzlein, H.; Reed Murtagh, F. An english translation of alzheimer's 1907 paper, "über eine eigenartige erkankung der hirnrinde". *Clinical Anatomy* **1995**, *8*, 429–431.

4. Glenner, G. G.; Wong, C. W. Alzheimer's disease: Initial report of the purification and characterization of a novel cerebrovascular amyloid protein. *Biochemical and Biophysical Research Communications* **1984**, *120*, 885–890.

5. Tanzi, R. E.; Bertram, L. Twenty years of the Alzheimer's disease amyloid hypothesis: A genetic perspective. *Cell* **2005**, *120*, 545–555.

6. Hardy, J. A.; Higgins, G. A. Alzheimer's disease: The amyloid cascade hypothesis. *Science* **1992**, *256*, 184–185.

7. Turner, P. R.; O'Connor, K.; Tate, W. P.; Abraham, W. C. *Progress in Neurobiology*; 2003; Vol. 70; pp 1–32.

8. Müller, U. C.; Deller, T.; Korte, M. Not just amyloid: Physiological functions of the amyloid precursor protein family. *Nature Reviews Neuroscience* **2017**, *18*, 281–298.

9. Pauwels, K.; Williams, T. L.; Morris, K. L.; Jonckheere, W.; Vandersteen, A.; Kelly, G.; Schymkowitz, J.; Rousseau, F.; Pastore, A.; Serpell, L. C.; Broersen, K. Structural basis for increased toxicity of pathological Aβ42:Aβ40 ratios in alzheimer disease. *Journal of Biological Chemistry* **2012**, *287*, 5650–5660.

10. Zhang, X.; Fu, Z.; Meng, L.; He, M.; Zhang, Z. The Early Events That Initiate β-Amyloid Aggregation in Alzheimer's Disease. *Frontiers in Aging Neuroscience* **2018**, *10*, 1–13.

11. Wang, J.; Gu, B. J.; Masters, C. L.; Wang, Y. J. A systemic view of Alzheimer disease - Insights from amyloid-β metabolism beyond the brain. *Nature Reviews Neurology* **2017**, *13*, 612–623.

12. Hellström-Lindahl, E.; Viitanen, M.; Marutle, A. Comparison of Aβ levels in the brain of familial and sporadic Alzheimer's disease. *Neurochemistry International* **2009**, *55*, 243–252.

13. Yankner, B. A.; Dawes, L. R.; Fisher, S.; Villa-komaroff, L.; Yankner, B. A.; Dawes, L. R.; Fisher, S.; Villa-komaroff, L.; Oster-granite, M. L.; Neve, R. L. Neurotoxicity of a Fragment of the Amyloid Precursor Associated with Alzheimer's Disease. **1989**, *245*, 417–420.

14. Kanski, J.; Aksenova, M.; Allan Butterfield, D. The hydrophobic environment of Met35 of Alzheimer's Aβ(1-42) is important for the neurotoxic and oxidative properties of the peptide. *Neurotoxicity Research* **2002**, *4*, 219–223.

15. Bode, D. C.; Freeley, M.; Nield, J.; Palma, M.; Viles, J. H. Amyloid-β oligomers have a profound detergent-like effect on lipid membrane bilayers, imaged by atomic force and electron microscopy. *Journal of Biological Chemistry* **2019**, *294*, 7566–7572.

16. Hou, L.; Shao, H.; Zhang, Y.; Li, H.; Menon, N. K.; Neuhaus, E. B.; Brewer, J. M.; Byeon, I. J. L.; Ray, D. G.; Vitek, M. P.; Iwashita, T.; Makula, R. A.; Przybyla, A. B.; Zagorski, M. G. Solution NMR Studies of the Aβ(1-40) and Aβ(1-42) Peptides Establish that the Met35 Oxidation State Affects the Mechanism of Amyloid Formation. *Journal of the American Chemical Society* **2004**, *126*, 1992–2005.

17. O'Brien, R.; Wong, P. Amyloid Precursor Protein Processing in Alzheimer's Disease. *Annual Review of Neuroscience* **2011**, *34*, 185–204.

18. El Khoury, J.; Toft, M.; Hickman, S. E.; Means, T. K.; Terada, K.; Geula, C.; Luster, A. D. Ccr2 deficiency impairs microglial accumulation and accelerates progression of Alzheimer-like disease. *Nature Medicine* **2007**, *13*, 432–438.

19. Wyss-Coray, T.; Rogers, J. Inflammation in Alzheimer disease-A brief review of the basic science and clinical literature. *Cold Spring Harbor Perspectives in Medicine* **2012**, *2*, 1–23.

20. Haass, C.; Selkoe, D. J. Soluble protein oligomers in neurodegeneration: Lessons from the Alzheimer's amyloid β-peptide. *Nature Reviews Molecular Cell Biology* **2007**, *8*, 101–112.

21. Podlisny, M. B.; Ostaszewski, B. L.; Squazzo, S. L.; Koo, E. H.; Rydell, R. E.; Teplow, D. B.; Selkoe, D. J. Aggregation of secreted amyloid β-protein into sodium dodecyl sulfate- stable oligomers in cell culture. *Journal of Biological Chemistry* **1995**, *270*, 9564–9570.

22. Gong, Y.; Chang, L.; Viola, K. L.; Lacor, P. N.; Lambert, M. P.; Finch, C. E.; Krafft, G. A.; Klein, W. L. Alzheimer's disease-affected brain: Presence of oligomeric Aβ ligands (ADDLs) suggests a molecular basis for reversible memory loss. *Proceedings of the National Academy of Sciences of the United States of America* **2003**, *100*, 10417–10422.

23. Walsh, D. M.; Tseng, B. P.; Rydel, R. E.; Podlisny, M. B.; Selkoe, D. J. The oligomerization of amyloid β-protein begins intracellularly in cells derived from human brain. *Biochemistry* **2000**, *39*, 10831–10839.

24. Lesné, S.; Ming, T. K.; Kotilinek, L.; Kayed, R.; Glabe, C. G.; Yang, A.; Gallagher, M.; Ashe, K. H. A specific amyloid-β protein assembly in the brain impairs memory. *Nature* **2006**, *440*, 352–357.

25. Fu, Z.; Aucoin, D.; Davis, J.; Van Nostrand, W. E.; Smith, S. O. Mechanism of Nucleated Conformational Conversion of Aβ42. *Biochemistry* **2015**, *54*, 4197–4207.

26. Harper, J. D.; Wong, S. S.; Lieber, C. M.; Lansbury, P. T. Observation of metastable Aβ amyloid protofibrils by atomic force microscopy. *Chemistry and Biology* **1997**, *4*, 119–125.

27. Scheidt, H. A.; Morgado, I.; Huster, D. Solid-state NMR reveals a close structural relationship between amyloid-β protofibrils and oligomers. *Journal of Biological Chemistry* **2012**, *287*, 22822–22826.

28. Scheidt, H. A.; Morgado, I.; Rothemund, S.; Huster, D.; Fändrich, M. Solid-state NMR spectroscopic investigation of Aβ protofibrils: Implication of a β-sheet remodeling upon maturation into terminal amyloid fibrils. *Angewandte Chemie - International Edition* **2011**, *50*, 2837–2840.

29. Querol-Vilaseca, M.; Colom-Cadena, M.; Pegueroles, J.; Nuñez-Llaves, R.; Luque-Cabecerans, J.; Muñoz-Llahuna, L.; Andilla, J.; Belbin, O.; Spires-Jones, T. L.; Gelpi, E.; Clarimon, J.; Loza-Alvarez, P.; Fortea, J.; Lleó, A. Nanoscale structure of amyloid-β plaques in Alzheimer's disease. *Scientific Reports* **2019**, *9*, 1–10.

30. Tsai, J.; Grutzendler, J.; Duff, K.; Gan, W. B. Fibrillar amyloid deposition leads to local synaptic abnormalities and breakage of neuronal branches. *Nature Neuroscience* **2004**, *7*, 1181–1183.

31. Cloe, A. L.; Orgel, J. P.; Sachleben, J. R.; Tycko, R.; Meredith, S. C. The Japanese mutant Aβ (ΔE22-Aβ 1-39) forms fibrils instantaneously, with low-thioflavin T fluorescence: Seeding of wild-type Aβ 1-40 into atypical fibrils by Δe22- Aβ 1-39. *Biochemistry* **2011**, *50*, 2026–2039.

32. Tomidokoro, Y.; Rostagno, A.; Neubert, T. A.; Lu, Y.; William Rebeck, G.; Frangione, B.; Greenberg, S. M.; Ghiso, J. Iowa variant of familial Alzheimer's disease: Accumulation of posttranslationally modified AβD23N in parenchymal and cerebrovascular amyloid deposits. *American Journal of Pathology* **2010**, *176*, 1841–1854.

33. Biancalana, M.; Koide, S. Molecular mechanism of Thioflavin-T binding to amyloid fibrils. *Biochimica et Biophysica Acta - Proteins and Proteomics* **2010**, *1804*, 1405–1412.

34. Srivastava, A. K.; Pittman, J. M.; Zerweck, J.; Venkata, B. S.; Moore, P. C.; Sachleben, J. R.; Meredith, S. C. β-Amyloid aggregation and heterogeneous nucleation. *Protein Science* **2019**, *28*, 1567–1581.

35. Gremer, L.; Schölzel, D.; Schenk, C.; Reinartz, E.; Labahn, J.; Ravelli, R. B. G.; Tusche, M.; Lopez-iglesias, C.; Hoyer, W.; Heise, H.; Willbold, D.; Schröder, G. F. Fibril structure of amyloid-beta(1-42) by cryo–electron microscopy. *Science* **2017**, *358*, 116–119.

36. Tycko, R. Molecular structure of aggregated amyloid-β: Insights from solid-state nuclear magnetic resonance. *Cold Spring Harbor Perspectives in Medicine* **2016**, *6*, a024083.

37. Qahwash, I. M.; Boire, A.; Lanning, J.; Krausz, T.; Pytel, P.; Meredith, S. C. Site-specific effects of peptide lipidation on β-amyloid aggregation and cytotoxicity. *Journal of Biological Chemistry* **2007**, *282*, 36987–36997.

38. Morel, B.; Carrasco, M. P.; Jurado, S.; Marco, C.; Conejero-Lara, F. Dynamic micellar oligomers of amyloid beta peptides play a crucial role in their aggregation mechanisms. *Physical Chemistry Chemical Physics* **2018**, *20*, 20597–20614.

39. Sabaté, R.; Estelrich, J. Evidence of the existence of micelles in the fibrillogenesis of β-amyloid peptide. *Journal of Physical Chemistry B* **2005**, *109*, 11027–11032.

40. Faller, P.; Hureau, C.; Berthoumieu, O. Role of metal ions in the self-assembly of the Alzheimer's amyloid-β peptide. *Inorganic Chemistry* **2013**, *52*, 12193–12206.

41. Lim, K. H.; Kim, Y. K.; Chang, Y. T. Investigations of the molecular mechanism of metal-induced Aβ (1-40) amyloidogenesis. *Biochemistry* **2007**, *46*, 13523–13532.

42. Lee, M. C.; Yu, W. C.; Shih, Y. H.; Chen, C. Y.; Guo, Z. H.; Huang, S. J.; Chan, J. C.; Chen, Y. R. Zinc ion rapidly induces toxic, off-pathway amyloid-β oligomers distinct from amyloid-β derived diffusible ligands in Alzheimer's disease. *Scientific Reports* **2018**, *8*, 1–16.

43. Breydo, L.; Uversky, V. N. Structural, morphological, and functional diversity of amyloid oligomers. *FEBS Letters* **2015**, *589*, 2640–2648.

44. Kumar, A.; Paslay, L. C.; Lyons, D.; Morgan, S. E.; Correia, J. J.; Rangachari, V. Specific soluble oligomers of amyloid-β peptide undergo replication and form non-fibrillar aggregates in interfacial environments. *Journal of Biological Chemistry* **2012**, *287*, 21253–21264.

45. Bode, D. C.; Baker, M. D.; Viles, J. H. Ion channel formation by amyloid-β42 oligomers but not amyloid-β40 in cellular membranes. *Journal of Biological Chemistry* **2017**, *292*, 144–1413.

46. Serra-Batiste, M.; Ninot-Pedrosa, M.; Bayoumi, M.; Gairí, M.; Maglia, G.; Carulla, N. Aβ42 assembles into specific β-barrel pore-forming oligomers in membrane-mimicking environments. *Proceedings of the National Academy of Sciences of the United States of America* **2016**, *113*, 10866–10871.

47. Lindberg, D. J.; Wesén, E.; Björkeroth, J.; Rocha, S.; Esbjörner, E. K. Lipid membranes catalyse the fibril formation of the amyloid-β (1–42) peptide through lipid-fibril interactions that reinforce secondary pathways. *Biochimica et Biophysica Acta - Biomembranes* **2017**, *1859*, 1921–1929.

48. Sabaté, R.; Gallardo, M.; Estelrich, J. Spontaneous incorporation of β-amyloid peptide into neutral liposomes. *Colloids and Surfaces A: Physicochemical and Engineering Aspects* **2005**, *270-271*, 13–17.

49. Williams, T. L.; Serpell, L. C. Membrane and surface interactions of Alzheimer's Aβ peptide - Insights into the mechanism of cytotoxicity. *FEBS Journal* **2011**, *278*, 3905–3917.

50. Safar, J.; Wille, H.; Itri, V.; Groth, D.; Serban, H.; Torchia, M.; Cohen, F. E.; Prusiner, S. B. Eight prion strains have PrP(Sc) molecules with different conformations. *Nature Medicine* **1998**, *4*, 1157–1165.

51. Tycko, R. Amyloid Polymorphism: Structural Basis and Neurobiological Relevance. *Neuron* **2015**, *86*, 632–645.

52. Collinge, J.; Clarke, A. R. A general model of prion strains and their pathogenicity. *Science* **2007**, *318*, 930–936.

53. Bousset, L.; Pieri, L.; Ruiz-Arlandis, G.; Gath, J.; Jensen, P. H.; Habenstein, B.; Madiona, K.; Olieric, V.; Böckmann, A.; Meier, B. H.; Melki, R. Structural and functional characterization of two alpha-synuclein strains. *Nature Communications* **2013**, *4*, 2575.

54. Gath, J.; Bousset, L.; Habenstein, B.; Melki, R.; Böckmann, A.; Meier, B. H. Unlike twins: An NMR comparison of two α-synuclein polymorphs featuring different toxicity. *PLoS ONE* **2014**, *9*, e90659.

55. Frederick, K. K.; Debelouchina, G. T.; Kayatekin, C.; Dorminy, T.; Jacavone, A. C.; Griffin, R. G.; Lindquist, S. Distinct prion strains are defined by amyloid core structure and chaperone binding site dynamics. *Chemistry and Biology* **2014**, *21*, 295–305.

56. Tycko, R. Physical and structural basis for polymorphism in amyloid fibrils. *Protein Science* **2014**, *23*, 1528–1539.

57. Qiang, W.; Kelley, K.; Tycko, R. Polymorph-specific kinetics and thermodynamics of β-amyloid fibril growth. *Journal of the American Chemical Society* **2013**, *135*, 6860–6871.

58. Petkova, A. T.; Leapman, R. D.; Guo, Z.; Yau, W. M.; Mattson, M. P.; Tycko, R. Self-propagating, molecular-level polymorphism in Alzheimer's β-amyloid fibrils. *Science* **2005**, *307*, 262–265.

59. Paravastu, A. K.; Leapman, R. D.; Yau, W. M.; Tycko, R. Molecular structural basis for polymorphism in Alzheimer's β-amyloid fibrils. *Proceedings of the National Academy of Sciences of the United States of America* **2008**, *105*, 18349–18354.

60. Lu, J. X.; Qiang, W.; Yau, W. M.; Schwieters, C. D.; Meredith, S. C.; Tycko, R. Molecular structure of β-amyloid fibrils in alzheimer's disease brain tissue. *Cell* **2013**, *154*, 1257–1268.

61. Qiang, W.; Yau, W. M.; Lu, J. X.; Collinge, J.; Tycko, R. Structural variation in amyloid-β fibrils from Alzheimer's disease clinical subtypes. *Nature* **2017**, *541*, 217–221.

62. Youn, Y. C.; Kang, S.; Suh, J.; Park, Y. H.; Kang, M. J.; Pyun, J. M.; Choi, S. H.; Jeong, J. H.; Park, K. W.; Lee, H. W.; An, S. S. A.; Dominguez, J. C.; Kim, S. Blood amyloid-β oligomerization associated with neurodegeneration of Alzheimer's disease. *Alzheimer's Research and Therapy* **2019**, *11*, 1–8.

63. Hsia, A. Y.; Masliah, E.; McConlogue, L.; Yu, G.-Q.; Tatsuno, G.; Hu, K.; Kholodenko, D.; Malenka, R. C.; Nicoll, R. A.; Mucke, L. Plaque-independent disruption of neural circuits in Alzheimer's Disease Models. *Proceedings of the National Academy of Sciences* **1999**, *96*, 3228–3233.

64. Wang, J.; Dickson, D. W.; Trojanowski, J. Q.; Lee, V. M. The levels of soluble versus insoluble brain aβ distinguish Alzheimer's disease from normal and pathologic aging. *Experimental Neurology* **1999**, *158*, 328–337.

65. Lue, L.-f.; Kuo, Y.-m.; Roher, A. E.; Brachova, L.; Shen, Y.; Sue, L.; Beach, T.; Kurth, J. H.; Rydel, R. E.; Rogers, J. Soluble Amyloid β Peptide Concentration as a Predictor of Synaptic Change in Alzheimer's Disease. *American Journal of Pathology* **1999**, *155*, 1–10.

66. McLean, C. A.; Cherny, R. A.; Fraser, F. W.; Fuller, S. J.; Smith, M. J.; Beyreuther, K.; Bush, A. I.; Masters, C. L. Soluble pool of Aβ amyloid as a determinant of severity of neurodegeneration in Alzheimer's disease. *Annals of Neurology* **1999**, *46*, 860–866.

67. Chimon, S.; Shaibat, M. A.; Jones, C. R.; Calero, D. C.; Aizezi, B.; Ishii, Y. Evidence of fibril-like β-sheet structures in a neurotoxic amyloid intermediate of Alzheimer's β-amyloid. *Nature Structural and Molecular Biology* **2007**, *14*, 1157–1164.

68. Kotler, S. A.; Brender, J. R.; Vivekanandan, S.; Suzuki, Y.; Yamamoto, K.; Monette, M.; Krishnamoorthy, J.; Walsh, P.; Cauble, M.; Holl, M. M.; Marsh, E. N. G.; Ramamoorthy, A. High-resolution NMR characterization of low abundance oligomers of amyloid-β without purification. *Scientific Reports* **2015**, *5*, 1–12.

69. Brath, U.; Swamy, S. I.; Veiga, A. X.; Tung, C. C.; Van Petegem, F.; Erdélyi, M. Paramagnetic Ligand Tagging to Identify Protein Binding Sites. *Journal of the American Chemical Society* **2015**, *137*, 11391–11398.

70. Fawzi, N. L.; Ying, J.; Torchia, D. A.; Clore, G. M. Kinetics of amyloid β monomer-to-oligomer exchange by NMR relaxation. *Journal of the American Chemical Society* **2010**, *132*, 9948–9951.

71. Clore, G. M. Seeing the invisible by paramagnetic and diamagnetic NMR. *Biochemical Society Transactions* **2013**, *41*, 1343–1354.

72. Sinnaeve, D. The Stejskal-Tanner Equation Generalized for Any Gradient Shape - An Overview of Most Pulse Sequences Measuring Free Diffusion. *Concepts in Magnetic Resonance Part A* **2012**, *40*, 39–65.

73. Arold, S.; Hoh, F.; Domergue, S.; Birck, C.; Delsuc, M.-A.; Jullien, M.; Dumas, C. Characterization and molecular basis of the oligomeric structure of HIV-1 Nef protein. *Protein Science* **2000**, *9*, 1137–1148.

74. Petkova, A. T.; Ishii, Y.; Balbach, J. J.; Antzutkin, O. N.; Leapman, R. D.; Delaglio, F.; Tycko, R. A structural model for Alzheimer's β-amyloid fibrils based on experimental constraints from solid state NMR. *Proceedings of the National Academy of Sciences of the United States of America* **2002**, *99*, 16742–16747.

75. Paravastu, A. K.; Qahwash, I.; Leapman, R. D.; Meredith, S. C.; Tycko, R. Seeded growth of β-amyloid fibrils from Alzheimer's brain-derived fibrils produces a distinct fibril structure. *Proceedings of the National Academy of Sciences of the United States of America* **2009**, *106*, 7443–7448.

76. Paravastu, A. K.; Petkova, A. T.; Tycko, R. Polymorphic fibril formation by residues 10-40 of the Alzheimer's β-amyloid peptide. *Biophysical Journal* **2006**, *90*, 4618–4629.

77. Uversky, V. N.; Gillespie, J. R.; Fink, A. L. Why are 'natively unfolded' proteins unstructured under physiologic conditions? *Proteins: Structure, Function and Genetics* **2000**, *41*, 415–427.

78. Fink, A. L. Natively unfolded proteins. *Current Opinion in Structural Biology* **2005**, *5*, 53–58.

79. Dunker, A. K.; Oldfield, C. J.; Meng, J.; Romero, P.; Yang, J. Y.; Chen, J. W.; Vacic, V.; Obradovic, Z.; Uversky, V. N. The unfoldomics decade: An update on intrinsically disordered proteins. BMC Genomics. 2008.

80. He, B.; Wang, K.; Liu, Y.; Xue, B.; Uversky, V. N.; Dunker, A. K. Predicting intrinsic disorder in proteins: An overview. *Cell Research* **2009**, *19*, 929–949.

81. Shivaprasad, S.; Wetzel, R. An intersheet packing interaction in Aβ fibrils mapped by disulfide cross-linking. *Biochemistry* **2004**, *43*, 15310–15317.

82. Shivaprasad, S.; Wetzel, R. Scanning cysteine mutagenesis analysis of Aβ-(1-40) amyloid fibrils. *Journal of Biological Chemistry* **2006**, *281*, 993–1000.

83. Shankar, G. M.; Li, S.; Mehta, T. H.; Garcia-Munoz, A.; Shepardson, N. E.; Smith, I.; Brett, F. M.; Farrell, M. A.; Rowan, M. J.; Lemere, C. A.; Regan, C. M.; Walsh, D. M.; Sabatini, B. L.; Selkoe, D. J. Amyloid-β protein dimers isolated directly from Alzheimer's brains impair synaptic plasticity and memory. *Nature Medicine* **2008**, *14*, 837–842.

84. Sandberg, A.; Luheshi, L. M.; Söllvander, S.; De Barros, T. P.; Macao, B.; Knowles, T. P.; Biverstål, H.; Lendel, C.; Ekholm-Petterson, F.; Dubnovitsky, A.; Lannfelt, L.; Dobson, C. M.; Härd, T. Stabilization of neurotoxic Alzheimer amyloid-β oligomers by protein engineering. *Proceedings of the National Academy of Sciences of the United States of America* **2010**, *107*, 15595–15600.

85. Lazo, N. D.; Grant, M. A.; Condron, M. C.; Rigby, A. C.; Teplow, D. B. On the nucleation of amyloid β-protein monomer folding. *Protein Science* **2009**, *14*, 1581–1596.

86. Grant, M. A.; Lazo, N. D.; Lomakin, A.; Condron, M. M.; Arai, H.; Yamin, G.; Rigby, A. C.; Teplow, D. B. Familial Alzheimer's disease mutations alter the stability of the amyloid β-protein monomer folding nucleus. *Proceedings of the National Academy of Sciences of the United States of America* **2007**, *104*, 16522–16527.

87. Baumketner, A.; Bernstein, S. L.; Wyttenbach, T.; Lazo, N. D.; Teplow, D. B.; Bowers, M. T.; Shea, J.-E. Structure of the 21-30 fragment of amyloid β-protein. *Protein Science* **2006**, *15*, 1239–1247.

88. Borreguero, J. M.; Urbanc, B.; Lazo, N. D.; Buldyrev, S. V.; Teplow, D. B.; Stanley, H. E. Folding events in the 21-30 region of amyloid β-protein (Aβ) studied in silico. *Proceedings of the National Academy of Sciences of the United States of America* **2005**, *102*, 6015–6020.

89. Chen, W.; Mousseau, N.; Derreumaux, P. The conformations of the amyloid-β (21-30) fragment can be described by three families in solution. *Journal of Chemical Physics* **2006**, *125*.

90. Cruz, L.; Urbanc, B.; Borreguero, J. M.; Lazo, N. D.; Teplow, D. B.; Stanley, H. E. Solvent and mutation effects on the nucleation of amyloid β-protein folding. *Proceedings of the National Academy of Sciences of the United States of America* **2005**, *102*, 18258–18263.

91. Fawzi, N. L.; Phillips, A. H.; Ruscio, J. Z.; Doucleff, M.; Wemmer, D. E.; Head-Gordon, T. Structure and dynamics of the Aβ21-30 peptide from the interplay of NMR experiments and molecular simulations. *Journal of the American Chemical Society* **2008**, *130*, 6145–6158.

92. Krone, M. G.; Baumketner, A.; Bernstein, S. L.; Wyttenbach, T.; Lazo, N. D.; Teplow, D. B.; Bowers, M. T.; Shea, J. E. Effects of Familial Alzheimer's Disease Mutations on the Folding Nucleation of the Amyloid β-Protein. *Journal of Molecular Biology* **2008**, *381*, 221–228.

93. Murray, M. M.; Krone, M. G.; Bernstein, S. L.; Baumketner, A.; Condron, M. M.; Lazo, N. D.; Teplow, D. B.; Wyttenbach, T.; Shea, J. E.; Bowers, M. T. Amyloid β-protein: Experiment and theory on the 21-30 fragment. *Journal of Physical Chemistry B* **2009**, *113*, 6041–6045.

94. Wetzel, R. Kinetics and thermodynamics of amyloid fibril assembly. *Accounts of Chemical Research* **2006**, *39*, 671–679.

95. O'Nuallain, B.; Shivaprasad, S.; Kheterpal, I.; Wetzel, R. Thermodynamics of Aβ(1-40) amyloid fibril elongation. *Biochemistry* **2005**, *44*, 12709–12718.

96. Akaike, H. A New Look at the Statistical Model Identification. *IEEE Transactions on Automatic Control* **1974**, *19*, 716–723.

97. Yamaoka, K.; Nakagawa, T.; Uno, T. Application of Akaike's information criterion (AIC) in the evaluation of linear pharmacokinetic equations. *Journal of Pharmacokinetics and Biopharmaceutics* **1978**, *6*, 165–175.

98. Yamaoka, K.; Tanigawara, Y.; Nakagawa, T.; Uno, T. A pharmacokinetic analysis program (multi) for microcomputer. *Journal of Pharmacobio-Dynamics* **1981**, *4*, 879–885.

99. Press, J. S. *Bayesian statistics: Principles, models, and applications.*; John Wiley & Sons: New York, NY, 1989.

100. Sachleben, J. R. Bayesian and information theory analysis of MAS sideband patterns in spin 1/2 systems. *Journal of Magnetic Resonance* **2006**, 123–133.

101. Sivia, D. *Data analysis: A Bayesian Tutorial*; Calrendon Press: Oxford, 1996.

102. Tycko, R. Solid-State NMR Studies of Amyloid Fibril Structure. *Annual Review of Physical Chemistry* **2011**, *62*, 279–299.

103. Tycko, R.; Wickner, R. B. Molecular structures of amyloid and prion fibrils: Consensus versus controversy. *Accounts of Chemical Research* **2013**, *46*, 1487–1496.

104. Ow, S. Y.; Dunstan, D. E. A brief overview of amyloids and Alzheimer's disease. *Protein Science* **2014**, *23*, 1315–1331.

105. Bush, A. I.; Pettingell, W. H.; Multhaup, G.; Paradis, M. D.; Vonsattel, J. P.; Gusella, J. F.; Beyreuther, K.; Masters, C. L.; Tanzi, R. E. Rapid induction of Alzheimer Aβ amyloid formation by zinc. *Science* **1994**, *265*, 1464–1467.

106. Atwood, C. S.; Moir, R. D.; Huang, X.; Scarpa, R. C.; Bacarra, N. M. E.; Romano, D. M.; Hartshorn, M. A.; Tanzi, R. E.; Bush, A. I. Dramatic aggregation of alzheimer by Cu(II) is induced by conditions representing physiological acidosis. *Journal of Biological Chemistry* **1998**, *273*, 12817–12826.

107. Lovell, M. A.; Robertson, J. D.; Teesdale, W. J.; Campbell, J. L.; Markesbery, W. R. Copper, iron and zinc in Alzheimer's disease senile plaques. *Journal of the Neurological Sciences* **1998**, *158*, 47–52.

108. Klug, G. M.; Losic, D.; Subasinghe, S. S.; Aguilar, M. I.; Martin, L. L.; Small, D. H. β-Amyloid protein oligomers induced by metal ions and acid pH are distinct from those generated by slow spontaneous ageing at neutral pH. *European Journal of Biochemistry* **2003**, *270*, 4282–4293.

109. Hou, L.; Zagorski, M. G. NMR reveals anomalous copper(II) binding to the amyloid Aβ peptide of Alzheimer's disease. *Journal of the American Chemical Society* **2006**, *128*, 9260–9261.

110. Ha, C.; Ryu, J.; Chan, B. P. Metal ions differentially influence the aggregation and deposition of Alzheimer's β-amyloid on a solid template. *Biochemistry* **2007**, *56*, 6118–6125.

111. Danielsson, J.; Pierattelli, R.; Banci, L.; Gräslund, A. High-resolution NMR studies of the zinc-binding site of the Alzheimer's amyloid β-peptide. *FEBS Journal* **2007**, *274*, 46–59.

112. Rezaei-Ghaleh, N.; Giller, K.; Becker, S.; Zweckstetter, M. Effect of zinc binding on β-amyloid structure and dynamics: Implications for Aβ aggregation. *Biophysical Journal* **2011**, *101*, 1202–1211.

113. Kozin, S. A.; Mezentsev, Y. V.; Kulikova, A. A.; Indeykina, M. I.; Golovin, A. V.; Ivanov, A. S.; Tsvetkov, P. O.; Makarov, A. A. Zinc-induced dimerization of the amyloid-β metal-binding domain 1-16 is mediated by residues 11-14. *Molecular BioSystems* **2011**, *7*, 1053–1055.

114. Solomonov, I.; Korkotian, E.; Born, B.; Feldman, Y.; Bitler, A.; Rahimi, F.; Li, H.; Bitan, G.; Sagi, I. Zn2+-Aβ40 complexes form metastable quasi-spherical oligomers that are cytotoxic to cultured hippocampal neurons. *Journal of Biological Chemistry* **2012**, *287*, 20555–20564.

115. Dies, H.; Toppozini, L.; Rheinstädter, M. C. The interaction between amyloid-β peptides and anionic lipid membranes containing cholesterol and melatonin. *PLoS ONE* **2014**, *9*, e99124.

116. Lu, M.; Yang, J.; Ren, Z.; Sabui, S.; Espejo, A.; Bedford, M. T.; Jacobson, R. H.; Jeruzalmi, D.; McMurray, J. S.; Chen, X. Crystal Structure of the Three Tandem FF Domains of the Transcription Elongation Regulator CA150. *Journal of Molecular Biology* **2009**, *393*, 397–408.

117. Vivekanandan, S.; Brender, J. R.; Lee, S. Y.; Ramamoorthy, A. A partially folded structure of amyloid-beta(1-40) in an aqueous environment. *Biochemical and Biophysical Research Communications* **2011**, *411*, 312–316.

118. Nanga, R. P. R.; Brender, J. R.; Vivekanandan, S.; Ramamoorthy, A. Structure and membrane orientation of IAPP in its natively amidated form at physiological pH in a membrane environment. *Biochimica et Biophysica Acta - Biomembranes* **2011**, *1808*, 2337–2342.

119. Singh, Y.; Sharpe, P. C.; Hoang, H. N.; Lucke, A. J.; McDowall, A. W.; Bottomley, S. P.; Fairlie, D. P. Amyloid formation from an α-helix peptide bundle is seeded by 3 10-helix aggregates. *Chemistry - A European Journal* **2011**, *17*, 151–160.

120. Scherpelz, K. P.; Lu, J. X.; Tycko, R.; Meredith, S. C. *Methods in Molecular Biology*; 2016.

121. Sciarretta, K. L.; Gordon, D. J.; Petkova, A. T.; Tycko, R.; Meredith, S. C. Aβ40-lactam(D23/K28) models a conformation highly favorable for nucleation of amyloid. *Biochemistry* **2005**, *44*, 6003–6014.

122. Dawson, P. E.; Muir, T. W.; Clark-Lewis, I.; Kent, S. B. Synthesis of proteins by native chemical ligation. *Science* **1994**, *266*, 776–779.

123. Hackeng, T. M.; Griffin, J. H.; Dawson, P. E. Protein synthesis by native chemical ligation: Expanded scope by using straightforward methodology. *Proceedings of the National Academy of Sciences of the United States of America* **1999**, *96*, 10068–10073.

124. Schnölzer, M.; Kent, S. B. Constructing proteins by dovetailing unprotected synthetic peptides: Backbone-engineered HIV protease. *Science* **1992**, *356*, 221–225.

125. Bang, D.; Chopra, N.; Kent, S. B. Total Chemical Synthesis of Crambin. *Journal of the American Chemical Society* **2004**, *126*, 1377–1383.

126. Chopra, N.; Gan, W.; Schreiber, H.; Kurutz, J. W.; Meredith, S. C. Versatile cyclic templates for assembly of axially oriented ligands. *Bioconjugate Chemistry* **2009**, *20*, 231–240.

127. Pentelute, B. L.; Kent, S. B. Selective desulfurization of cysteine in the presence of Cys(Acm) in polypeptides obtained by native chemical ligation. *Organic Letters* **2007**, *9*, 687–690.

128. Lebowitz, J.; Lewis, M. S.; Schuck, P. Modern analytical ultracentrifugation in protein science: A tutorial review. *Protein Science* **2009**, *11*, 2067–2079.

129. LeVine, H. Quantification of β-sheet amyloid fibril structures with thioflavin T. *Methods in Enzymology* **1999**, *309*, 274–284.

130. Naiki, H.; Higuchi, K.; Hosokawa, M.; Takeda, T. Fluorometric determination of amyloid fibrils in vitro using the fluorescent dye, thioflavine T. *Analytical Biochemistry* **1989**, *177*, 244–249.

131. Baryshnikova, O. K.; Williams, T. C.; Sykes, B. D. Internal pH indicators for biomolecular NMR. *Journal of Biomolecular NMR* **2008**, *41*, 5–7.

132. Bax, A.; Davis, D. G. Practical aspects of two-dimensional transverse NOE spectroscopy. *Journal of Magnetic Resonance (1969)* **1985**, *63*, 207–213.

133. Hwang, T. L.; Shaka, A. J. Water Suppression That Works. Excitation Sculpting Using Arbitrary Wave-Forms and Pulsed-Field Gradients. *Journal of Magnetic Resonance - Series A* **1995**, *112*, 275–279.

134. Delaglio, F.; Grzesiek, S.; Vuister, G. W.; Zhu, G.; Pfeifer, J.; Bax, A. NMRPipe: A multidimensional spectral processing system based on UNIX pipes. *Journal of Biomolecular NMR* **1995**, *6*, 277–293.

135. Keller, R. *Goldau, Switzerland: Cantina Verlag*; 2004.

136. Cornilescu, G.; Delaglio, F.; Bax, A. Protein backbone angle restraints from searching a database for chemical shift and sequence homology. *Journal of Biomolecular NMR* **1999**, *13*, 289–302.

137. Shen, Y.; Delaglio, F.; Cornilescu, G.; Bax, A. TALOS+: A hybrid method for predicting protein backbone torsion angles from NMR chemical shifts. *Journal of Biomolecular NMR* **2009**, *44*, 213–223.

138. Berjanskii, M. V.; Wishart, D. S. A simple method to predict protein flexibility using secondary chemical shifts. *Journal of the American Chemical Society* **2005**, *127*, 14970–14971.

139. Ellman, G. L. Tissue sulfhydryl groups. *Archives of Biochemistry and Biophysics* **1959**, *82*, 70–77.

140. Sedlak, J.; Lindsay, R. H. Estimation of total, protein-bound, and nonprotein sulfhydryl groups in tissue with Ellman's reagent. *Analytical Biochemistry* **1968**, *25*, 192–205.

141. Riddles, P. W.; Blakeley, R. L.; Zerner, B. Reassessment of Ellman's Reagent. *Methods in Enzymology* **1983**, *91*, 49–60.

142. Schägger, H. Tricine-SDS-PAGE. *Nature Protocols* **2006**, *1*, 16–22.

143. Sidorova, M. V.; Molokoedov, A. S.; Az'muko, A. A.; Kudryavtseva, E. V.; Krause, E.; Ovchinnikov, M. V.; Bespalova, Z. D. The use of hydrogen peroxide for closing disulfide bridges in peptides. *Russian Journal of Bioorganic Chemistry* **2004**, *30*, 115–125.

144. Schägger, H. Tricine-SDS-PAGE. *Nature Protocols* **2006**, *1*, 16–22.

145. Sharpe, S.; Yau, W. M.; Tycko, R. Expression and purification of a recombinant peptide from the Alzheimer's β-amyloid protein for solid-state NMR. *Protein Expression and Purification* **2005**, *42*, 200–210.

146. Hayashi, K.; Kojima, C. pCold-GST vector: A novel cold-shock vector containing GST tag for soluble protein production. *Protein Expression and Purification* **2008**, *62*, 120–127.

147. Zhang, L.; Yu, H.; Song, C.; Lin, X.; Chen, B.; Tan, C.; Cao, G.; Wang, Z. Expression, purification, and characterization of recombinant human β-amyloid42 peptide in Escherichia coli. *Protein Expression and Purification* **2009**, *64*, 55–62.

148. Garai, K.; Crick, S. L.; Mustafi, S. M.; Frieden, C. Expression and purification of amyloid-β peptides from Escherichia coli. *Protein Expression and Purification* **2009**, *66*, 107–112.

149. Long, F.; Cho, W.; Ishii, Y. Expression and purification of 15N- and 13C-isotope labeled 40-residue human Alzheimer's β-amyloid peptide for NMR-based structural analysis. *Protein Expression and Purification* **2011**, *79*, 16–24.

150. Satakarni, M.; Curtis, R. Production of recombinant peptides as fusions with SUMO. *Protein Expression and Purification* **2011**, *78*, 113–119.

151. Weber, D. K.; Sani, M. A.; Gehman, J. D. A routine method for cloning, expressing and purifying Aβ(1-42) for structural NMR studies. *Amino Acids* **2014**, *46*, 2415–2426.

152. Li, W.; Gao, M.; Liu, W.; Kong, Y.; Tian, H.; Yao, W.; Gao, X. Optimized Soluble Expression and Purification of an Aggregation-prone Protein by Fusion Tag Systems and On-column Cleavage in Escherichia coli. *Protein & Peptide Letters* **2012**, *19*, 1324–1329.

153. Kim, E. K.; Moon, J. C.; Lee, J. M.; Jeong, M. S.; Oh, C.; Ahn, S. M.; Yoo, Y. J.; Jang, H. H. Large-scale production of soluble recombinant amyloid-β peptide 1-42 using cold-inducible expression system. *Protein Expression and Purification* **2012**, *86*, 53–57.

154. Chhetri, G.; Pandey, T.; Chinta, R.; Kumar, A.; Tripathi, T. An improved method for high-level soluble expression and purification of recombinant amyloid-beta peptide for in vitro studies. *Protein Expression and Purification* **2015**, *114*, 71–76.

155. Beel, A. J.; Mobley, C. K.; Hak, J. K.; Tian, F.; Hadziselimovic, A.; Jap, B.; Prestegard, J. H.; Sanders, C. R. Structural studies of the transmembrane C-terminal domain of the amyloid precursor protein (APP): Does APP function as a cholesterol sensor? *Biochemistry* **2008**, *47*, 9428–9446.

156. Pester, O.; Barrett, P. J.; Hornburg, D.; Hornburg, P.; Pröbstle, R.; Widmaier, S.; Kutzner, C.; Dürrbaum, M.; Kapurniotu, A.; Sanders, C. R.; Scharnagl, C.; Langosch, D. The backbone dynamics of the amyloid precursor protein transmembrane helix provides a rationale for the sequential cleavage mechanism of γ-secretase. *Journal of the American Chemical Society* **2013**, *135*, 1317–1329.

157. Yau, W. M.; Wimley, W. C.; Gawrisch, K.; White, S. H. The preference of tryptophan for membrane interfaces. *Biochemistry* **1998**, *283*, 22233–22243.

158. Sanchez, K. M.; Kang, G.; Wu, B.; Kim, J. E. Tryptophan-lipid interactions in membrane protein folding probed by ultraviolet resonance Raman and fluorescence spectroscopy. *Biophysical Journal* **2011**, *100*, 2121–2130.

159. De Jesus, A. J.; Allen, T. W. The role of tryptophan side chains in membrane protein anchoring and hydrophobic mismatch. *Biochimica et Biophysica Acta - Biomembranes* **2013**, *1828*, 864–876.

160. 12/98, T. *Novagen User Protocol Vectors*; Novagen, 1998.

161. Ben-Bassat, A.; Bauer, K.; Chang, S. Y.; Myambo, K.; Boosman, A. Processing of the initiation methionine from proteins: Properties of the Escherichia coli methionine aminopeptidase and its gene structure. *Journal of Bacteriology* **1987**, *169*, 751–757.

162. Bush, A. I.; Pettingell, W. H.; Paradis, M. D.; Tanzi, R. E. Modulation of Aβ adhesiveness and secretase site cleavage by zinc. *Journal of Biological Chemistry* **1994**, *269*, 12152–12158.

163. Atwood, C. S.; Moir, R. D.; Huang, X.; Scarpa, R. C.; Bacarra, N. M. E.; Romano, D. M.; Hartshorn, M. A.; Tanzi, R. E.; Bush, A. I. Dramatic aggregation of alzheimer by Cu(II) is induced by conditions representing physiological acidosis. *Journal of Biological Chemistry* **1998**, *273*, 12817–12826.

164. Atwood, C. S.; Scarpa, R. C.; Huang, X.; Moir, R. D.; Jones, W. D.; Fairlie, D. P.; Tanzi, R. E.; Bush, A. I. Characterization of copper interactions with Alzheimer amyloid β peptides: Identification of an attomolar-affinity copper binding site on amyloid β1-42. *Journal of Neurochemistry* **2000**, *75*, 1219–1233.

165. Talmard, C.; Guilloreau, L.; Coppel, Y.; Mazarguil, H.; Faller, P. Amyloid-beta peptide forms monomeric complexes with CuII and ZnII prior to aggregation. *ChemBioChem* **2007**, *8*, 163–165.

166. Tsvetkov, P. O.; Popov, I. A.; Nikolaev, E. N.; Archakov, A. I.; Makarov, A. A.; Kozin, S. A. Isomerization of the Asp7 residue results in zinc-induced oligomerization of Alzheimer's disease amyloid β (1-16) peptide. *ChemBioChem* **2008**, *9*, 1564–1567.

167. Faller, P.; Hureau, C. Bioinorganic chemistry of copper and zinc ions coordinated to amyloid-β peptide. *Dalton Transactions* **2009**, 1080–1094.

168. Bousejra-Elgarah, F.; Bijani, C.; Coppel, Y.; Faller, P.; Hureau, C. Iron(II) binding to amyloid-β, the Alzheimer's peptide. *Inorganic Chemistry* **2011**, *50*, 9024–9030.

169. Arnold, T.; Linke, D. The use of detergents to purify membrane proteins. *Current Protocols in Protein Science* **2008**, 4.8.1–4.8.30.

170. Puchades, M.; Westman, A.; Blennow, K.; Davidsson, P. Removal of sodium dodecyl sulfate from protein samples prior to matrix-assisted laser desorption/ionization mass spectrometry. *Rapid Communications in Mass Spectrometry* **1999**, *13*, 344–349.

171. Fontana, A. Modification of Tryptophan with Bnps-Skatole (2-(2-Nitrophenylsulfenyl)-3-Methyl-3-Bromoindolenine). *Methods in Enzymology* **1972**, *25*, 419–423.

172. Martenson, R. E.; Deibler, G. E.; Kramer, A. J. Reaction of Peptide 89-169 of Bovine Myelin Basic Protein with 2-(2-Nitrophenylsulfenyl)-3-methyl-3′-bromoindolenine. *Biochemistry* **1977**, *16*, 216–221.

173. Vestling, M. M.; Kelly, M. A.; Fenselau, C.; Costello, C. E. Optimization by mass spectrometry of a tryptophan□specific protein cleavage reaction. *Rapid Communications in Mass Spectrometry* **1994**, *8*, 786–790.

174. Rahali, V.; Gueguen, J. Chemical cleavage of bovine β-lactoglobulin by BNPS-skatole for preparative purposes: Comparative study of hydrolytic procedures and peptide characterization. *Journal of Protein Chemistry* **1999**, *18*, 1–12.

175. Crimmins, D. L.; Mische, S. M.; Denslow, N. D. Chemical Cleavage of Proteins in Solution. *Current Protocols in Protein Science* **2005**, *100*, 11.4.1–11.4.11.

176. Plimmer, R. H. A.; Eaves, E. C. The Estimation of Tyrosine in Proteins by Bromination. *Biochemical Journal* **1913**, *3*, 310.

177. Hou, L.; Lee, H. G.; Han, F.; Tedesco, J. M.; Perry, G.; Smith, M. A.; Zagorski, M. G. Modification of amyloid-β1-42 fibril structure by methionine-35 oxidation. *Journal of Alzheimer's Disease* **2013**, *37*, 9–18.

178. Hackenberger, C. P. The reduction of oxidized methionine residues in peptide thioesters with NH4I-Me2S. *Organic and Biomolecular Chemistry* **2006**, *4*, 2291–2295.

179. Senes, A.; Gerstein, M.; Engelman, D. M. Statistical analysis of amino acid patterns in transmembrane helices: The GxxxG motif occurs frequently and association with β-branched residues at neighboring positions. *Journal of Molecular Biology* **2000**, *296*, 921–936.

180. Ulmschneider, M. B.; Sansom, M. S. Amino acid distributions in integral membrane protein structures. *Biochimica et Biophysica Acta - Biomembranes* **2001**, *1512*, 1–14.

181. Bhardwaj, N.; Stahelin, R. V.; Langlois, R. E.; Cho, W.; Lu, H. Structural Bioinformatics Prediction of Membrane-binding Proteins. *Journal of Molecular Biology* **2006**, *359*, 486–495.

182. Sharpe, H. J.; Stevens, T. J.; Munro, S. A Comprehensive Comparison of Transmembrane Domains Reveals Organelle-Specific Properties. *Cell* **2010**, *142*, 158–169.

183. Harper, S.; Speicher, D. W. Expression and purification of GST fusion proteins. *Current Protocols in Protein Science* **2001**, 6.6.1–6.6.21.

184. 0661JN, T. R. C. *Novagen User Protocol*, 11th ed.; EMD Chemicals Inc., an affiliate of Merck KGaA: Darmstadt, Germany, 2011.

185. Marley, J.; Lu, M.; Bracken, C. A method for efficient isotopic labeling of recombinant proteins. *Journal of Biomolecular NMR* **2001**, *20*, 71–75.

186. Studier, F. W. Protein production by auto-induction in high density shaking cultures. *Protein expression and purification* **2005**, *41*, 207–234.

187. Schägger, H.; von Jagow, G. Tricine-sodium dodecyl sulfate-polyacrylamide gel electrophoresis for the separation of proteins in the range from 1 to 100 kDa. *Analytical Biochemistry* **1987**, *166*, 368–379.

188. Bax, A.; Ikura, M.; Kay, L. E.; Torchia, D. A.; Tschudin, R. Comparison of different modes of two-dimensional reverse-correlation NMR for the study of proteins. *Journal of Magnetic Resonance (1969)* **1990**, *86*, 304–318.

189. Tycko, R. Solid-state NMR as a probe of amyloid fibril structure. *Current Opinion in Chemical Biology* **2000**, *13*, 229–234.

190. Nelson, R.; Eisenberg, D. Structural Models of Amyloid-Like Fibrils. *Advances in Protein Chemistry* **2006**, *73*, 235–282.

191. Meier, B. H.; Riek, R.; Böckmann, A. Emerging Structural Understanding of Amyloid Fibrils by Solid-State NMR. *Trends in Biochemical Sciences* **2017**, *42*, 777–787.

192. Iadanza, M. G.; Jackson, M. P.; Hewitt, E. W.; Ranson, N. A.; Radford, S. E. A new era for understanding amyloid structures and disease. *Nature Reviews Molecular Cell Biology* **2018**, *19*.

193. Hayden, E. Y.; Teplow, D. B. Amyloid β-protein oligomers and Alzheimer's disease. *Alzheimer's Research and Therapy* **2013**, *62*, 1261–1276.

194. Fändrich, M.; Schmidt, M.; Grigorieff, N. Recent progress in understanding Alzheimer's β-amyloid structures. *Trends in Biochemical Sciences* **2011**, *36*, 338–345.

195. Cline, E. N.; Bicca, M. A.; Viola, K. L.; Klein, W. L. The Amyloid-β Oligomer Hypothesis: Beginning of the Third Decade. *Journal of Alzheimer's Disease* **2018**, *64*, S567–S610.

196. Selkoe, D. J.; Hardy, J. The amyloid hypothesis of Alzheimer's disease at 25 years. *EMBO Molecular Medicine* **2016**, *8*, 595–608.

197. Sengupta, U.; Nilson, A. N.; Kayed, R. The Role of Amyloid-β Oligomers in Toxicity, Propagation, and Immunotherapy. *EBioMedicine* **2016**, *6*, 42–49.

198. Lambert, M. P.; Barlow, A. K.; Chromy, B. A.; Edwards, C.; Freed, R.; Liosatos, M.; Morgan, T. E.; Rozovsky, I.; Trommer, B.; Viola, K. L.; Wals, P.; Zhang, C.; Finch, C. E.; Krafft, G. A.; Klein, W. L. Diffusible, nonfibrillar ligands derived from Aβ1-42 are potent central nervous system neurotoxins. *Proceedings of the National Academy of Sciences of the United States of America* **1998**, *85*, 6448–6453.

199. Fezoui, Y.; Hartley, D. M.; Harper, J. D.; Khurana, R.; Walsh, D. M.; Condron, M. M.; Selkoe, D. J.; Lansbury, J.; Fink, A. L.; Teplow, D. B. An improved method of preparing the amyloid β-protein for fibrillogenesis and neurotoxicity experiments. *Amyloid* **2000**, *7*, 166–178.

200. Chung, H.; Crooks, E. J.; Ziliox, M.; Smith, S. O. *Methods in Molecular Biology*; 2018.

201. Kamiie, J.; Aihara, N.; Uchida, Y.; Kobayashi, D.; Yoshida, Y.; Kuroda, T.; Sakaue, M.; Sugihara, Y.; Rezeli, M.; Marko-Varga, G. Amyloid-specific extraction using organic solvents. *MethodsX* **2020**, *7*, 100770.

202. LeVine, H. Alzheimer's β-peptide oligomer formation at physiologic concentrations. *Analytical Biochemistry* **2004**, *335*, 81–90.

203. Nichols, M. R.; Moss, M. A.; Reed, D. K.; Cratic-McDaniel, S.; Hoh, J. H.; Rosenberry, T. L. Amyloid-β protofibrils differ from amyloid-β aggregates induced in dilute hexafluoroisopropanol in stability and morphology. *Journal of Biological Chemistry* **2005**, *280*, 2471–2480.

204. Österlund, N.; Kulkarni, Y. S.; Misiaszek, A. D.; Wallin, C.; Krüger, D. M.; Liao, Q.; Mashayekhy Rad, F.; Jarvet, J.; Strodel, B.; Wärmländer, S. K.; Ilag, L. L.; Kamerlin, S. C.; Gräslund, A. Amyloid-β Peptide Interactions with Amphiphilic Surfactants: Electrostatic and Hydrophobic Effects. *ACS Chemical Neuroscience* **2018**, *9*, 1680–1692.

205. Gooch, J. W. *Encyclopedic Dictionary of Polymers*; 2011.

206. Marius Clore, G.; Iwahara, J. Theory, practice, and applications of paramagnetic relaxation enhancement for the characterization of transient low-population states of biological macromolecules and their complexes. *Chemical Reviews* **2009**, *109*, 4108–4139.

207. Stoltenberg, M.; Bush, A. I.; Bach, G.; Smidt, K.; Larsen, A.; Rungby, J.; Lund, S.; Doering, P.; Danscher, G. Amyloid plaques arise from zinc-enriched cortical layers in APP/PS1 transgenic mice and are paradoxically enlarged with dietary zinc deficiency. *Neuroscience* **2007**, *150*, 357–369.

208. Istrate, A. N.; Kozin, S. A.; Zhokhov, S. S.; Mantsyzov, A. B.; Kechko, O. I.; Pastore, A.; Makarov, A. A.; Polshakov, V. I. Interplay of histidine residues of the Alzheimer's disease Aβ peptide governs its Zn-induced oligomerization. *Scientific Reports* **2016**, *6*, 1–14.

209. Ryu, J.; Girigoswami, K.; Ha, C.; Ku, S. H.; Park, C. B. Influence of multiple metal ions on β-amyloid aggregation and dissociation on a solid surface. *Biochemistry* **2008**, *47*, 5328–5335.

210. Banerjee, S.; Sun, Z.; Hayden, E. Y.; Teplow, D. B.; Lyubchenko, Y. L. Nanoscale Dynamics of Amyloid β-42 Oligomers As Revealed by High-Speed Atomic Force Microscopy. *ACS Nano* **2017**, *11*, 12202–12209.

211. Hayden, E. Y.; Conovaloff, J. L.; Mason, A.; Bitan, G.; Teplow, D. B. *Methods in Molecular Biology*; 2018.

212. Fancy, D. A.; Kodadek, T. Chemistry for the analysis of protein-protein interactions: Rapid and efficient cross-linking triggered by long wavelength light. *Proceedings of the National Academy of Sciences of the United States of America* **1999**, *96*, 6020–6024.

213. Matsubara, T.; Yasumori, H.; Ito, K.; Shimoaka, T.; Hasegawa, T.; Sato, T. Amyloid-fibrils assembled on ganglioside-enriched membranes contain both parallel -sheets and turns. *Journal of Biological Chemistry* **2018**, *293*, 14146–14154.

214. Yip, C. M.; Elton, E. A.; Darabie, A. A.; Morrison, M. R.; Mclaurin, J. Cholesterol, a modulator of membrane-associated Aβ-fibrillogenesis and neurotoxicity. *Journal of Molecular Biology* **2001**, *311*, 723–734.

215. Sakai, T.; Kaneko, Y.; Tsujii, K. Premicellar aggregation of fatty acid N-methylethanolamides in aqueous solutions. *Langmuir* **2006**, *22*, 2039–2044.

216. Gillitt, N. D.; Savelli, G.; Bunton, C. A. Premicellization of dimethyl Di-n-dodecylammonium chloride. *Langmuir* **2006**, *22*, 5570–5571.

217. Cui, X.; Mao, S.; Liu, M.; Yuan, H.; Du, Y. Mechanism of surfactant micelle formation. *Langmuir* **2008**, *24*, 10771–10775.

218. Vold, M. J. Micellization Process with Emphasis on Premicelles. *Langmuir* **1992**, *8*, 1082–1085.

219. Niu, S.; Gopidas, K. R.; Turro, N. J.; Gabor, G. Formation of Premicellar Clusters of 2-p-Toluidinonaphthalene-6-sulfonate with Cationic Detergents. *Langmuir* **1992**, *8*, 1271–1277.

220. Barnadas-Rodríguez, R.; Estelrich, J. Photophysical changes of pyranine induced by surfactants: Evidence of premicellar aggregates. *Journal of Physical Chemistry B* **2009**, *113*, 1972–1982.

221. Beija, M.; Fedorov, A.; Charreyre, M. T.; Martinho, J. M. Fluorescence anisotropy of hydrophobic probes in poly(N -decylacrylamide)- block -poly(N,N -diethylacrylamide) block copolymer aqueous solutions: Evidence of premicellar aggregates. *Journal of Physical Chemistry B* **2010**, *114*, 9977–9986.

222. Buckingham, S. A.; Garvey, C. J.; Warr, G. G. Effect of head-group size on micellization and phase behavior in quaternary ammonium surfactant systems. *Journal of Physical Chemistry* **1993**, *97*, 10236–10244.

223. Menger, F. M.; Littau, C. A. Gemini Surfactants: Synthesis and Properties. *Journal of the American Chemical Society* **1991**, *113*, 1451–1452.

224. Lee, Y. C.; Liu, H. S.; Lin, S. Y.; Huang, H. F.; Wang, Y. Y.; Chou, L. W. An observation of the coexistence of multimers and micelles in a nonionic surfactant C10E4 solution by dynamic light scattering. *Journal of the Chinese Institute of Chemical Engineers* **2008**, *39*, 75–83.

225. Lebard, D. N.; Levine, B. G.; DeVane, R.; Shinoda, W.; Klein, M. L. Premicelles and monomer exchange in aqueous surfactant solutions above and below the critical micelle concentration. *Chemical Physics Letters* **2012**, *522*, 38–42.

226. Yan, H.; Cui, P.; Liu, C. B.; Yuan, S. L. Molecular dynamics simulation of pyrene solubilized in a sodium dodecyl sulfate micelle. *Langmuir* **2012**, *28*, 4931–4938.

227. Jiang, Y.; Chen, H.; Cui, X. H.; Mao, S. Z.; Liu, M. L.; Luo, P. Y.; Du, Y. R. 1H NMR study on pre-micellization of quaternary ammonium gemini surfactants. *Langmuir* **2008**, *24*, 3118–3121.

228. Yunes, S. J.; Gillitt, N. D.; Bunton, C. A. Examination of the pseudophase model of monomer-micelle interconversion in cetylpyridinium chloride. *Journal of Colloid and Interface Science* **2005**, *281*, 482–487.

229. Zou, M.; Dong, J.; Yang, G.; Li, X. A comprehensive study on micellization of dissymmetric pyrrolidinium headgroup-based gemini surfactants. *Physical Chemistry Chemical Physics* **2015**, *17*, 10265–10273.

230. Atherton, S. J.; Dymond, C. M. Formation of clusters between ionic species and sodium dodecyl sulfate below the critical micelle concentration. Ethidium ions and divalent metal ions. *Journal of Physical Chemistry* **1989**, *93*, 6809–6813.

231. Brinchi, L.; Di Profio, P.; Germani, R.; Goracci, L.; Savelli, G.; Gillitt, N. D.; Bunton, C. A. Premicellar accelerated decarboxylation of 6-nitrobenzisoxazole-3-carboxylate ion and its 5-tetradecyloxy derivative. *Langmuir* **2007**, *23*, 436–442.

232. Cho, J. R.; Morawetz, H. Catalysis of Ionic Reactions by Micelles. Reaction of Co(NH3)5Cl2+ with Hg2+ in Sodium Alkyl Sulfate Solutions. *Journal of the American Chemical Society* **1972**, *94*, 375–377.

233. Graciani, M. D. M.; Rodríguez, A.; Fernández, G.; Moyá, M. L. Study of ligand substitution reactions involving the Fe(CN)5H2O3- ions in surfactant solutions. *Langmuir* **1997**, *13*, 4239–4245.

234. Drennan, C. E.; Hughes, R. J.; Reinsborough, V. C.; Soriyan, O. O. Rate enhancement of nickel(II) complexation in dilute anionic surfactant solutions. *Canadian Journal of Chemistry* **1998**, *76*, 152–157.

235. Méndez-Pérez, M.; Vaz, B.; García-Río, L.; Pérez-Lorenzo, M. Polymeric premicelles as efficient lipophilic nanocarriers: Extending drug uptake to the submicellar regime. *Langmuir* **2013**, *29*, 11251–11259.

236. Zerweck, J.; Venkata, B. S.; Pittman, J. M.; Srivastava, A. K.; Moore, P. C.; Sachleben, J. R.; Thinakaran, G.; Meredith, S. C. A versatile method for producing labeled or unlabeled Aβ55, Aβ40, and other β-amyloid family peptides. *Protein Expression and Purification* **2019**, *162*, 72–82.

237. Heinrikson, R. L.; Meredith, S. C. Amino acid analysis by reverse-phase high-performance liquid chromatography: Precolumn derivatization with phenylisothiocyanate. *Analytical Biochemistry* **1984**, *136*, 65–74.

238. Sohma, Y.; Sasaki, M.; Hayashi, Y.; Kimura, T.; Kiso, Y. Design and synthesis of a novel water-soluble Aβ1-42 isopeptide: An efficient strategy for the preparation of Alzheimer's disease-related peptide, Aβ1-42, via O-N intramolecular acyl migration reaction. *Tetrahedron Letters* **2004**, *45*, 5965–5968.

239. Sjodt, M.; Clubb, R. Nitroxide Labeling of Proteins and the Determination of Paramagnetic Relaxation Derived Distance Restraints for NMR Studies. *BIO-PROTOCOL* **2017**, *7*, e2207.

240. Labuda, A.; Cleveland, J.; Geisse, N.; Kocun, M.; Ohler, B.; Proksch, R.; Viani, M.; Walters, D. Photothermal excitation for improved cantilever drive performance in tapping mode atomic force microscopy. *Microscopy and Analysis* **2014**, *28*, S21–S25.

241. Ridler, T. W.; Calvard, S. Picture thresholding using an iterative selection method. *IEEE Transactions on Systems, Man and Cybernetics* **1978**, *8*, 630–632.

242. Cavanagh, J.; Fairbrother, W. J.; Palmer, A. G.; Skelton, N. J.; Rance, M. *Protein NMR Spectroscopy*; 2007.

243. Bruker, Bruker Topspin.

244. Norris, M.; Fetler, B.; Marchant, J.; Johnson, B. A. NMRFx Processor: a cross-platform NMR data processing program. *Journal of Biomolecular NMR* **2016**, *65*, 205–216.

245. Lee, W.; Tonelli, M.; Markley, J. L. NMRFAM-SPARKY: Enhanced software for biomolecular NMR spectroscopy. *Bioinformatics* **2015**, *31*, 1325–1327.

246. Johnson, B. A.; Blevins, R. A. NMR View: A computer program for the visualization and analysis of NMR data. *Journal of Biomolecular NMR* **1994**, *4*, 603–614.

247. Stejskal, E. O.; Tanner, J. E. Spin diffusion measurements: Spin echoes in the presence of a time-dependent field gradient. *The Journal of Chemical Physics* **1965**, *42*, 288.

248. Kyte, J.; Doolittle, R. F. A simple method for displaying the hydropathic character of a protein. *Journal of Molecular Biology* **1982**, *157*, 105–132.

249. Eisenberg, D.; Schwarz, E.; Komaromy, M.; Wall, R. Analysis of membrane and surface protein sequences with the hydrophobic moment plot. *Journal of Molecular Biology* **1984**, *179*, 125–142.

250. Hopp, T. P.; Woods, K. R. Prediction of protein antigenic determinants from amino acid sequences. *Proceedings of the National Academy of Sciences of the United States of America* **1981**, *78*, 3824–3828.

251. Rose, G. D.; Geselowitz, A. R.; Lesser, G. J.; Lee, R. H.; Zehfus, M. H. Hydrophobicity of amino acid residues in globular proteins. *Science* **1985**, *229*, 835–838.

252. Edrey, Y. H.; Medina, D. X.; Gaczynska, M.; Osmulski, P. A.; Oddo, S.; Caccamo, A.; Buffenstein, R. Amyloid beta and the longest-lived rodent: The naked mole-rat as a model for natural protection from alzheimer's disease. *Neurobiology of Aging* **2013**, *34*, 2352–2360.

253. Sowade, R. F.; Jahn, T. R. Seed-induced acceleration of amyloid -β Mediated neurotoxicity in vivo. *Nature Communications* **2017**, *8*, 1–12.

254. Jan, A.; Adolfsson, O.; Allaman, I.; Buccarello, A. L.; Magistretti, P. J.; Pfeifer, A.; Muhs, A.; Lashuel, H. A. Aβ42 neurotoxicity is mediated by ongoing nucleated polymerization process rather than by discrete Aβ42 species. *Journal of Biological Chemistry* **2011**, *286*, 8585–8596.

255. Cohen, S. I. A.; Linse, S.; Luheshi, L. M.; Hellstrand, E.; White, D. A.; Rajah, L.; Otzen, D. E.; Vendruscolo, M.; Dobson, C. M.; Knowles, T. P. J. Proliferation of amyloid-β42 aggregates occurs through a secondary nucleation mechanism. *Proceedings of the National Academy of Sciences of the United States of America* **2013**, *110*, 9758–9763.

256. Chimon, S.; Ishii, Y. Capturing intermediate structures of Alzheimer's β-amyloid, Aβ(1-40), by solid-state NMR spectroscopy. *Journal of the American Chemical Society* **2005**, *127*, 13472–13473.